Design Considerations for Engineered Myocardium

Design Considerations for Engineered Myocardium

A dissertation presented

by

Sean Paul Sheehy

to

The School of Engineering and Applied Sciences

in partial fulfillment of the requirements
for the degree of

Doctor of Philosophy

in the subject of

Engineering Sciences

Harvard University
Cambridge, Massachusetts

March, 2014

Dissertation Advisor: Professor Kevin Kit Parker Sean Paul Sheehy

Design Considerations for Engineered Myocardium

Abstract

The fabrication of biomimetic heart muscle suitable for pharmaceutical compound evaluation and disease modeling is hindered by limitations in our understanding of how to guide and assess the maturity of engineered myocardium *in vitro*. We hypothesized that tissue architecture serves as an important cue for directing the maturation of engineered heart tissues and that reliable assessment of maturity could be performed using a multi-parametric rubric utilizing cardiomyocytes of known developmental state as a basis for comparison. Physical micro-environmental cues are recognized to play a fundamental role in normal heart development, therefore we used micro-patterned extracellular matrix to direct isolated cardiac myocytes to self-assemble into anisotropic sheets reminiscent of the architecture observed in the laminar musculature of the heart. Comparison of global sarcomere alignment, gene expression, and contractile stress in engineered anisotropic myocardium to isotropic monolayers, as well as, adult ventricular tissue revealed that anisotropic engineered myocardium more closely matched the characteristics of adult ventricular tissue, than isotropic cultures of randomly organized cardiomyocytes. These findings support the notion that tissue architecture is an important cue for building mature engineered myocardium. Next, we sought to develop a quality assessment strategy that utilizes a core set of 64 experimental measurements representative of 4 major categories (*i.e.* gene expression, myofibril structure, electrical

activity, and contractility) to provide a numeric score of how closely stem cell-derived cardiac myocytes match the physiological characteristics of mature, post-natal cardiomyocytes. The efficacy of this rubric was assessed by comparing anisotropic engineered tissues fabricated from commercially-available murine ES- (mES) and iPS- (miPS) derived myocytes against neonatal mouse ventricular myocytes. The quality index scores calculated for these cells revealed that the miPS-derived myocytes more closely resembled the neonate ventricular myocytes than the mES-derived myocytes. Taken together, the results of these studies provide valuable insight into the fabrication and validation of engineered myocardium that faithfully recapitulate the characteristics of mature ventricular myocardium found *in vivo*. These engineered tissue design and quality validation strategies may prove useful in developing heart muscle analogs from human stem cell-derived myocytes that more accurately predict patient response than currently used animal models.

Table of Contents

Table of Figures

Acknowledgments

I would like to express my deepest gratitude to my advisor, Professor Kit Parker for taking a chance on hiring me to run his lab more than a decade ago, and encouraging me to pursue graduate studies. I am truly grateful for his guidance, patience, and support throughout my development as a scientist. He has helped me to grow as an individual and taught me what it takes to become a leader. It has been a tremendous honor to participate in the founding of the Disease Biophysics Group, and it has brought me great joy and triumph to watch it flourish over the years.

I would also like to thank my dissertation committee for their understanding, support, and advice in navigating the challenges of my PhD studies. Their scientific knowledge and general wisdom were critically helpful in completing this work. I would like to thank Professor Donald Ingber for his valuable time and insightful advice. I would also like to thank Professor Neel Joshi for all of his guidance and feedback in preparing this dissertation.

Many thanks go out to all of the members of the Disease Biophysics Group, past and present for their guidance, support, and most importantly, friendship. I cannot even begin to enumerate the vast wealth of knowledge that has been bestowed upon me by the many talented post-doctoral fellows that have passed through the lab over the years. I will also be forever grateful for the emotional support and personal guidance that they were always quick to bestow upon me in both triumph and defeat. In particular, I would like to express my most sincere gratitude to Dr. Adam Feinberg, Dr. Anya Grosberg, Dr. Francesco Pasqualini, and Dr. Patrick Campbell for the helpful advice and knowledge they imparted throughout the course of my research. I also would like to specifically

thank Dr. Leila Deravi, Mr. Borna Dabiri, Dr. Johan Ulrik Lind, and Dr. Patrick Campbell for their sage advice on my presentations, manuscripts, and science in general. Through your support, encouragement, and guidance, you guys made this possible.

Last, but not least, I would like to thank my family, particularly my siblings Joseph, Rachel, Heather, and Victoria for all of the love and support that they have showered upon me over the years. The late night motivational conversations with Victoria, southern delicacy care packages from Heather, and never ending stream of niece and nephew pictures from all of them never failed to pick me up during the challenging times. I love you all very much, and I would not have been able to complete my graduate school journey without you.

1 Introduction

Myocardial development is regulated by an elegantly choreographed ensemble of signaling events mediated by a multitude of intermediates that take a variety of forms. Cellular differentiation and maturation are a subset of vertically integrated processes that extend over several spatial and temporal scales to create a well-defined collective of cells that are able to function cooperatively and reliably at the organ level. Early efforts to understand the molecular mechanisms of cardiomyocyte fate determination focused primarily on genetic and chemical mediators of this process. However, increasing evidence suggests that mechanical interactions between the extracellular matrix (ECM) and cell surface receptors as well as physical interactions between neighboring cells play important roles in regulating the signaling pathways controlling the developmental processes of the heart. Interdisciplinary efforts have made it apparent that the influence of the ECM on cellular behavior occurs through a multitude of physical mechanisms, such as ECM boundary conditions, elasticity, and the propagation of mechanical signals to intracellular compartments, such as the nucleus. In addition to experimental studies, a number of mathematical models have been developed that attempt to capture the interplay between cells and their local microenvironment and the influence these interactions have on cellular self-assembly and functional behavior. Nevertheless, many questions remain unanswered concerning the mechanism through which physical interactions between cardiomyocytes and their environment are translated into biochemical cellular responses and how these signaling modalities can be utilized *in vitro* to fabricate myocardial tissue constructs from stem cell-derived cardiomyocytes that more faithfully represent their *in vivo* counterpart. These studies represent a broad effort

to characterize biological form as a conduit for information transfer that spans the nanometer length-scale of proteins to the meter length-scale of the patient and may yield new insights into the contribution of mechantransduction into heart development and disease.

1.1 Mechanotransduction Influences Cardiomyocyte Form and Function

A vexing issue in cardiac development is the presence of a three-dimensional structural and functional hierarchy that spans several orders of spatial magnitude from the centimeter length scale of the myocardium to the nanometer length scale of actomyosin motors (Figure 1-1). One possible mechanism through which architectural and temporal synchrony is maintained during cardiac organogenesis is the propagation of mechanical forces, encoding multi-scale information, from super-cellular, cellular, and sub-cellular networks that are physically connected throughout the heart. Simplified, qualitative models of cellular development often overlook the importance of mechanical cues and the bi-directional flow of information between cells and their local microenvironment during tissue formation [1]. Physical forces transmitted between cells and the extracellular matrix (ECM), as well as between neighboring cells, could prove vital to the emergent form and function of the healthy myocardium during cardiac morphogenesis. These mechanical cues may be an essential component of a larger biological network that integrates chemical and mechanical signals to drive nascent cells to adopt relevant phenotypes based on contextual information encoded in the local microenvironment [2].

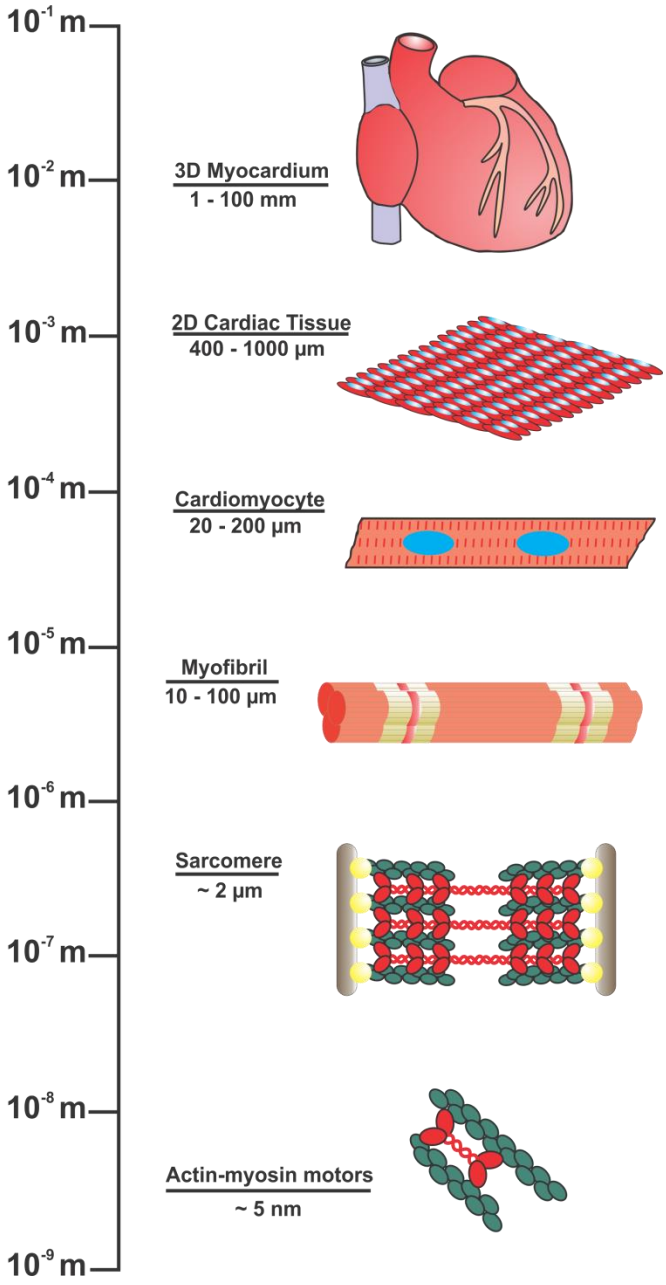

Figure 1-1: Spatial scaling of the functional components of the heart.

The functional components of the myocardium demonstrate a hierarchical relationship that spans several orders of spatial magnitude, from the nanometer length scale of the proteins comprising actomyosin cross-bridges to the millimeter length sheets of laminar myocardial tissue that make up the muscular walls of the heart chambers.

It is now well accepted that epigenetic factors, such as mechanical forces, play a fundamental role in regulating organ development [3, 4]. The physical properties of the local microenvironment and the contractile activity of cells influence the developmental processes that take place during embryogenesis [5]. Individual cells sense external mechanical cues primarily through interactions with the ECM via integrin binding and from neighboring cells through intercellular junctions [6]. Mechanical tension in the cytoskeleton arising from intercellular junctions and ECM adhesions has been shown experimentally to contribute to epithelial branching [7] and angiogenesis during lung development [8, 9]. Mechanical forces also underlie morphological changes that occur in the heart during development, wherein alterations to cardiomyocyte shape and spatial organization arising from actin cytoskeletal dynamics influence looping of the embryonic heart tube, for example. [10-12]. In the post-natal myocardium, forces endured during the contraction cycle are postulated to contribute to development and remodeling through cardiomyocyte hypertrophy, in which changes to myofibril and ECM architecture can lead to either adaptive or maladaptive growth [13, 14]. This review will examine the contributing role of mechanical forces to cellular development within the heart and explore the potential benefits of mathematical models for capturing the involvement of post-translational cytoskeletal dynamics in recapitulating the development of the myocardium *in vitro*. Knowledge gained from these models could provide valuable insight for designing custom ECM micro-environments that allow the construction of functional, patient-relevant engineered tissues from ES- and iPS-derived cardiomyocytes.

1.2 Mechanical Cues Associated with Cardiac Development

During formation of the heart, the cardiac mesoderm arises from the primitive streak as a product of temporally-synchronized Wnt, BMP, and activin/Nodal signaling events that occur in a spatially-asymmetric manner [15]. In turn, this left-right asymmetrical patterning results in activation of distinct gene expression profiles, differential proliferation, and cardiomyocyte shape changes that are responsible for regionalized myocardial lineage specification and the morphological transition from a linear tube to the four-chambered structure that the heart ultimately adopts [15-17]. Looping of the embryonic heart tube is primarily the product of localized changes in cardiomyocyte morphology that have been shown to arise from intrinsic remodeling of the actin cytoskeleton, and may also play a role in activating the regional changes in proliferation and gene expression observed in subsequent phases of cardiac development [16, 18, 19]. Post-natal cardiomyocyte growth and development occurs through a process known as 'hypertrophy' that is mediated by signaling events that are activated by both biochemical and biomechanical stimuli [20]. Cardiac hypertrophy is initiated by hemodynamic load and characterized by increased cardiomyocyte size and the expression of genes that are believed to act as a compensatory mechanism to normalize ventricular afterload [21, 22]. In order to recognize and respond to changes in systolic wall stress, the cells comprising the myocardium must possess a communications pathway that allows external physical cues to activate intracellular signaling cascades.

The cytoskeleton is the primary conduit for mechanically-encoded information in the cell [23], regulating cell shape [24] and influencing migration, cellular function and homeostasis [25-27]. Transmembrane integrin receptors provide a direct mechanical

linkage between the ECM and the cytoskeleton within the cell through which external physical forces may influence intra-cellular processes (Figure 1-2A) [28]. Over the course of development, the heart undergoes coordinated changes in ECM composition and expression of α- and β-integrin isoforms that specifically recognize various ECM components [29-31]. In the fetal stage, expression levels of fibronectin and α5β1 integrin receptors are elevated relative to expression levels observed in the adult myocardium [32-34]. This differential expression of fibronectin and β1 integrins has been associated with the proliferation and spreading that is observed in pre-natal cardiomyocytes, but absent post-partum [35, 36]. Variations in β1 integrin splice isoforms also distinguish the embryonic and adult myocardium. Embryonic cardiomyocytes have been shown to primarily express the β1A isoform, while adult cardiomyocytes preferentially express the β1D variant [37-39]. Furthermore, ablation of β1 integrin expression in the ventricular myocytes of transgenic mice revealed that disruption of normal integrin function resulted in pathological fibrotic remodeling, increased susceptibility to dilated cardiomyopathy, and perinatal mortality [40, 41]. Taken together, this relationship between the shift in integrin isoform expression and ECM composition suggests that the integrin-ECM interface may serve as a means for the cells of the nascent heart to recognize and respond to the ever changing mechanical forces that are present during cardiac organogenesis.

1.3 Signaling through the Integrin-ECM Interface

Transmembrane integrin receptors form a direct mechanical linkage between the ECM and the cytoskeleton [42] and serve as the primary conduit of bi-directional signaling between cells and the ECM [43, 44] despite the fact that they lack intrinsic kinase activity

[28]. Mechanical forces are transmitted across the integrin-ECM interface to the cytoskeleton, where they activate mechano-sensitive signal transducers, such as focal adhesion kinase (FAK), that are able to translate the mechanical cue into a biochemical response [45-47]. This mode of information transmission has been shown to activate a variety of chemical signaling pathways, including the Rho kinase, PI3K, ILK, Src, ERK, and MAP kinase pathways that modulate transcriptional activity and direct important cellular activities, such as cell cycle entry and the induction of apoptosis [3, 25, 28, 48, 49]. Many of these signaling intermediates are immobilized on the cytoskeleton, particularly at the Z-discs in cardiomyocytes, and are thus subject to mechanical perturbations that may modulate their activity and translocation to cellular compartments, such as the nucleus [50-52]. Cardiomyocytes express a protein known as melusin that flanks sarcomeric α-actinin at the Z lines and interacts with the cytoplasmic domain of β1 integrins [53]. Melusin has been implicated as an important sensor of myocardial wall stress in murine knock-out studies that showed a specific attenuation of glycogen kinase 3β signaling in melusin-null hearts [54]. Another Z-disc protein that is widely regarded to serve as a mechano-sensor is muscle LIM protein (MLP), which is believed to transduce mechanical signals via the calcineurin-NFAT pathway to activate the hypertrophic response in cardiomyocytes [55, 56]. Titin, a component of the sarcomere that regulates diastolic tension, possesses a C-terminal kinase domain that has been implicated in cardiomyocyte strain sensing [57]. It has been shown that this catalytic domain is involved in regulating the activity of the muscle-specific transcriptional co-activators MuRF2 and four-and-a-half-LIM-domain (FHL) through changes in titin conformation [58-60]. Evidence suggests that MLP stabilizes the interaction between T-

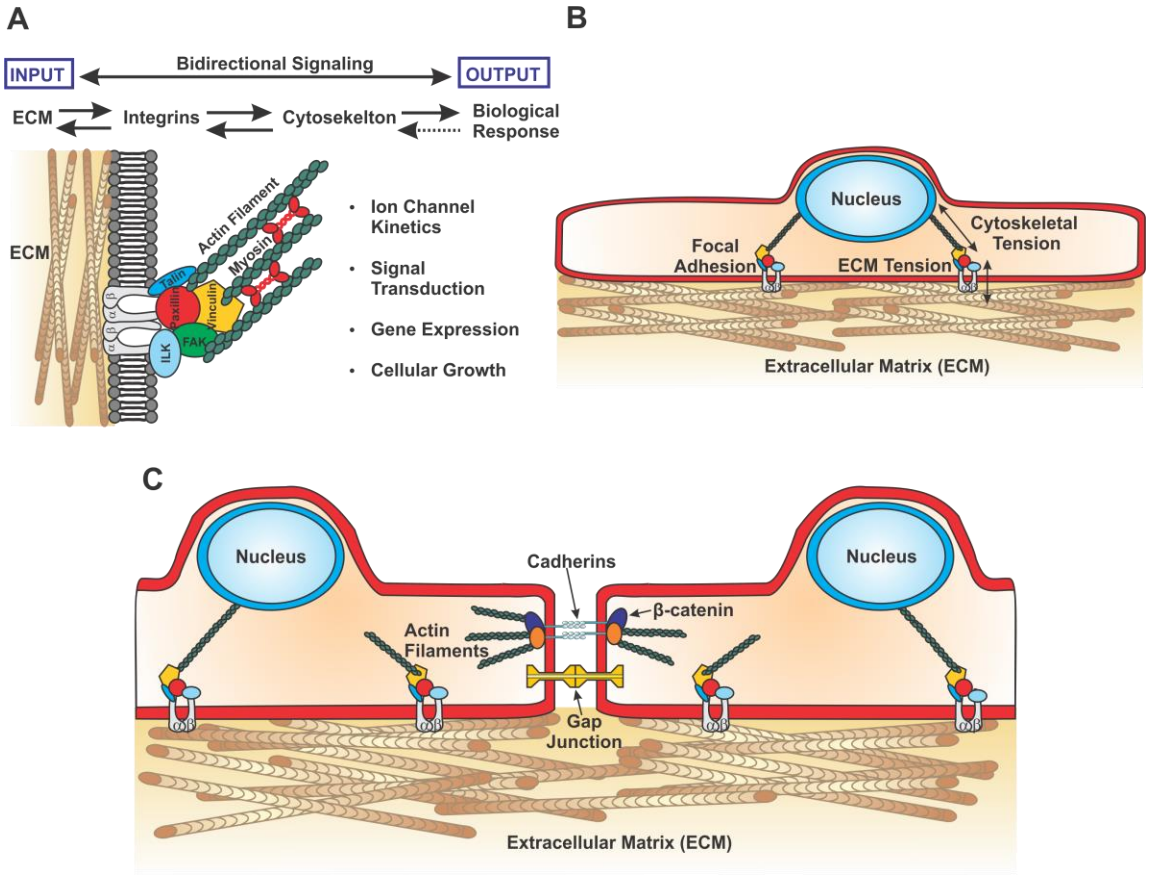

Figure 1-2: Bi-directional signaling interfaces in engineered myocardium.

(A) External mechanical cues are transmitted from the ECM to intracellular compartments via transmembrane integrin receptors that physically link it to the cytoskeleton. These mechanical signals elicit a number of biological responses ranging from ion channel activity to programmed cell death, and in turn these biological processes can feed information back to the extracellular space via the same mechanical pathway. (B) Transmembrane integrin receptors form a direct physical linkage between the ECM and the cytoskeleton through focal adhesions that provides a conduit for transmitting mechanical signals directly to intracellular compartments, such as the nucleus. (C) In addition to mechanotransduction through the integrin-ECM interface,

(Continued) cardiomyocytes also respond to mechanical signals from neighboring cells through intercellular junctions and direct transmembrane ligand-receptor interactions.

cap and titin at the Z-disc, providing an interface through which mechanical forces can be transmitted between the ECM and titin to initiate signaling events at the titin catalytic domain in response to hemodynamic load [61-63].

An intriguing alternative signaling paradigm is the transduction of mechanical signals through the ECM-cytoskeletal network to structures deep within the cytoplasm, such as the nucleus (Figure 1-2B), where they can alter enzymatic activity or gene expression by modulating nuclear shape or physically deforming genomic structures within the nuclear compartment [64, 65]. This hypothesis is supported by *in situ* PCR measurements taken from osteoblasts that revealed cell shape-dependent alterations in nuclear morphology resulted in differential regulation of osteocalcin expression, suggesting that cytoskeletal tension directly impacted transcriptional activity [66]. Given the kinetic nature of the myocardium, and observations that cardiomyocyte nuclei reversibly deform during each contraction cycle [67], the possibility exists that mechanical effects on nuclear morphology may influence the expression of genes in cardiomyocytes as well.

Experimental data suggests that individual filaments of the cytoskeleton bear tensile and compressive loads and give rise to a mechanical network under isometric tension that propagates physical signals throughout the cell at a velocity far exceeding the limits of chemical diffusion [42, 50, 68, 69]. Neonatal rat ventricular myocytes (NRVMs) cultured on micro-contact printed ECM substrates that imposed an anisotropic

morphology and organization possessed elongated nuclei that demonstrated a high degree of mutual alignment across the tissue constructs and underwent dynamic deformation during contraction [67]. Genes encoding proteins involved in tissue remodeling processes have been found to be susceptible to changes in cellular morphology induced as a consequence of direct perturbation of cytoskeletal structure with actin and microtubule disrupting agents, such as cytochalasin D and colchicine [70]. Studies of the link between cytoskeletal dynamics, motility, and gene expression during myocardial development revealed that myocardin-related transcription factors (MRTFs) are physically bound to globular actin monomers until they are incorporated into actin filaments. Upon release from actin monomers, the MRTFs are free to translocate to the nucleus, where they interact with the transcription factor serum response factor (SRF) to promote the expression of genes under its control [71]. This relationship between actin cytoskeletal assembly and regulation of cardiac gene expression by MRTF-SRF has been shown to be mediated through a Rho-dependent mechanism that may provide a feed-forward loop for driving the expression of genes necessary for myofibrillogenesis during myocardial development and in response to hypertrophic stimuli [72, 73].

Many genetic markers of vascular smooth muscle-specific differentiation code for proteins associated with contractility, giving rise to a potential role for Rho-dependent changes in smooth muscle contractility in regulating smooth muscle gene expression during vascular development [74]. Experiments conducted on capillary network formation by human microvascular endothelial cells *in vitro* and retinal angiogenesis *in vivo* using the Rho inhibitor p190RhoGAP revealed that Rho-induced changes in cytoskeletal architecture regulated angiogenesis by modulating the activities of two

antagonistic transcription factors, TFII-1, and GATA2, that govern expression of the VEGF receptor in a manner that was sensitive to ECM elasticity [75]. Dynamic assembly and disassembly of cytoskeletal elements generates directed forces that perturb cell shape and guide the organization of cellular components [23, 49]. The evidence from these studies support the notion that mechanical force-balance influences cellular behavior by modulating gene expression activity and may be an important factor for regulating cell fate decisions during co-development of the heart and circulatory system.

1.4 Signaling through Intercellular Junctions

In addition to force transmission across the integrin-ECM interface, cells also receive biomechanical input from their neighbors via intercellular junctions and through direct transmembrane ligand-receptor interactions (Figure 1- 2C)[76, 77]. Cytoskeletal tension arising from actomyosin crossbridges plays a key role in the formation and maintenance of intercellular junctions during cardiac tissue development [78-80]. *In vitro* studies have shown that the magnitude of tractional forces transmitted through the cytoskeletons of adjacent endothelial cells across adherens junctions was correlated to the size and strength of these junctions [81]. The phenotype and spatial organization of nascent cells during tissue formation require the coordinated regulation of gene expression and precise interactions between neighboring cells. Interactions that typically target transmembrane Notch receptors and the Wnt signaling intermediates localize to adherens junctions [82, 83]. The activity of the Notch and Wnt/β-catenin signaling pathways has been found to have reciprocal effects in cardiac progenitor cells during embryonic development of the heart [84-86]. In addition, canonical and non-canonical

Wnt signaling have differential, stage-dependent effects on cardiomyocyte maturation during normal heart development [83, 87]. Notch1 signaling promotes differentiation of cardiac progenitor cells and negatively regulates the activity of β-catenin. On the other hand, activation of β-catenin by the canonical Wnt pathway inhibits differentiation by negatively regulating cardiac transcription factors and instead promotes proliferation of cardiac progenitor cells [88]. In addition, Notch1 activation in cardiac progenitor cells gives rise to a population of Nkx2.5 expressing transit amplifying myocytes that are believed to mediate postnatal growth of the myocardium [85].

Notch and Wnt/β-catenin signaling pathways also play a role in regulating the incidence of endothelial-mesenchymal transformation (EMT) during valve development in a potentially mechano-sensitive manner [89, 90]. Formation of the heart valves during the early stages of heart development is traditionally considered to be a product of VEGF signaling, but it coincides with increased fluid shear stress and mechanical strain [91-93]. *In vitro* studies of engineered valve endothelial cells showed that the incidence of EMT in these constructs was not only enhanced by the application of chronic cyclic stretch, but also that the magnitude of applied strain initiated EMT via different pathways [94]. A mechanical load of 10% strain initiated EMT via TGF-β1, while wnt/β-catenin signaling was implicated at 20% strain, providing evidence that cells not only respond to external mechanical cues, but can also distinguish loads of different magnitudes. Furthermore, a myofibroblast phenotype emerged concomitantly with an increased incidence of EMT in valve endothelial cells cultured on an ECM substrate that imposed an anisotropic cellular organization and subjected to orthogonal, 20% cyclic strain. Break down of adherens junctions is a hallmark of EMT, along with the expression of factors that inhibit

endothelial genes [95], suggesting that the magnitude of tension transmitted across intercellular junctions may serve as a mediator of phenotype switching during cardiac valve morphogenesis.

The assembly of gap junction channels in cardiomyocytes has been shown experimentally to be closely tied to the formation of adherens junctions [96], in which N-cadherin and connexin 43 share a temporal relationship in their expression and spatial co-localization during adherens junction formation [97]. Immunolabeling studies conducted on embryonic, adolescent, and adult rat hearts revealed that connexin 43 gap junction-related immunoreactivity could be observed in the ventricles as early as 10 days post-conception, and incorporation of connexin 43 gap junctions into the costameres of ventricular myocytes proceeded well into adolescence [98]. Dual voltage clamp measurements taken on pairs of NRVMs with pre-defined aspect ratios revealed that intercellular conductance increased with the volume of observed connexin 43 immunosignal as cellular aspect ratio increased [99]. Further, mechanical forces acting on myocytes during contraction *in vivo* and pulsatile stretch *in vitro* were found to cause a dramatic increase in the expression of connexin 43 and a concomitant increase in conduction velocity due to increased electrical coupling between myocytes [96]. Given the relationship between cell alignment and impulse propagation velocity in cardiac tissues [100, 101], mechanical forces transmitted between neighboring cardiomyocytes could be important for establishing and maintaining the anisotropic conduction pattern necessary for proper functioning of the heart.

1.5 Effects of the Mechanical Environment on Cardiomyocytes

When considering the cellular microenvironment, the traditional paradigm has been that of the diffusion of soluble mitogens in autocrine and paracrine signaling through the interstitial space. Over the last 10 to 15 years, an interdisciplinary group of cell biologists and engineers have postulated an alternative and supplementary vision of the cellular microenvironment as a mechanical network of cells coupled by the protein polymer network of the extracellular matrix that propagates information, encoded as mechanical forces, between cells at data rates that far exceed that of chemical diffusion. In the embryonic heart, evolving from a pulsatile tube to a cyclically-contracting 4-chambered structure, mechanical forces are imposed on maturing cardiomyocytes that vary in their magnitude and frequency over the course of development [11, 13]. Regional alterations in cell shape have been observed and postulated to contribute to the overall morphology that emerges during heart development [16, 102]. The *in vitro* cellular microenvironment can be engineered to force isolated cells to adopt the morphology and configuration of their native tissues so that researchers can study the contributions of tissue geometry to functionality [2, 100, 103-105]. Interactions between cardiomyocytes and the ECM cause changes in cell shape that direct actin filament orientation, sarcomere organization, and myofibrillogenesis *in vitro* [26]. Studies of cultured cardiovascular cells have shown that shape also influences a number of functional properties, such as voltage-gated ion currents, calcium dynamics, and contractility, suggesting that it is an important parameter to consider when designing engineered tissue constructs [106-109].

Phenomena, such as durotaxis, have led many researchers to postulate that the physical properties of the cellular microenvironment can influence cell phenotype and

tissue morphogenesis [110, 111]. Experiments conducted on stem cells encapsulated in RGD-modified matrices suggest a role for cellular tractional forces generated through interactions between the ECM and specific integrin isoforms in guiding lineage commitment [112, 113]. In addition, studies of embryonic cardiomyocytes reveal that changes in matrix rigidity associated with normal heart development and fibrotic ECM remodeling reminiscent of that observed after myocardial infarction dramatically affect rhythmic contraction of the cells [114, 115]. Isolated cardiomyocytes cultured on poly-acrylamide gels with tunable elastic moduli have repeatedly demonstrated increased contractile activity and myofibril organization when the stiffness of their underlying substrate resembles that measured for the healthy native myocardium (approximately 20 kPa), as opposed to culturing them on substrates with higher or lower elastic moduli [114, 116-118]. In the case of marrow-derived mesenchymal stem cells (MSCs), studies have shown that culturing naïve MSCs on elastic substrates with a modulus of approximately 10 kPa specifically induced a myogenic phenotype [119]. It is believed that cells sense the mechanical stiffness of the ECM through tractional forces generated by cross-bridge interactions between actin and myosin-II. *In vitro* experiments utilizing inhibitors of non-muscle myosin II isoforms lend support to this hypothesis, demonstrating that cytoskeletal tension plays a role in mediating mechano-sensation between focal adhesions and the ECM [120]. Force measurements collected on various types of cells cultured on elastomeric substrates revealed a linear relationship between apparent focal adhesion size and cellular force generation that was dependent upon actomyosin interactions [121]. While myocardial contractile activity is not considered to play a role in the early stages of heart development [10, 11, 122], there is evidence in zebrafish models that hemodynamic

load does alter cardiomyocyte shape, leading to aberrations in ventricular morphogenesis [91, 123]. Together, these findings demonstrate a clear role for the physical micro-environment in myocardial development that researchers may potentially harness in the creation of artificial tissue constructs.

Cardiomyocytes are constantly subjected to physical stretching as a result of the contractile activity of the heart, presenting the possibility that the motion of the myocardium may activate mechano-sensitive signaling pathways that affect the characteristics of cardiac cells [124]. Pulsatile stretch has been shown experimentally to promote parallel alignment of NRVMs and induce mechanotransductive signaling events through the β_1 integrin-ECM interface that were responsible for the up-regulation of N-cadherin and connexin 43 expression via activation of FAK and the ERK1/2 pathway [125-127]. Concomitant with the enhanced expression of connexin 43, cyclic stretch was also found to increase propagation velocity in NRVM monolayers [128]. Gene expression measurements taken on NRVM cultures exposed to pulsatile stretch show that the mechanical stimulus gives rise to a hypertrophic phenotype with expression of the "fetal gene program" and myosin heavy chain isoform switching that are hallmarks of cardiac hypertrophy [129-131]. All together, these studies reveal that the mechanical properties of the cellular microenvironment do contribute to the functional maturation of the myocardium and that there is a need for computational tools that will allow researchers to construct effective strategies for harnessing these mechanical cues to optimize engineered cardiac tissue self-assembly and contractile performance.

1.6 Computational Modeling of Mechanotransduction

The working myocardium is comprised of rectangular myocytes organized into a laminar arrangement that serves to optimize cooperative sarcomeric force output. It is postulated that the interplay between geometric cues encoded in the ECM and cardiomyocyte cytoskeletal dynamics confers these morphological characteristics that are vital to the proper functioning of the heart. Refinements in our understanding of cellular mechanobiology, facilitated in large part by advances in soft lithography, have given rise to mathematical models of the phenomena and parameters involved in mechano-sensation that may contribute to myocardial tissue development. The most pivotal of these experimental methodologies was the development of *in vitro* techniques to regulate ECM composition and geometry [132, 133] that have made it possible to engineer cells whose morphology and function are amenable to computational modeling, thus closing the loop between theory and experiment. This is important, because one poorly studied problem in cell biology is the post-translational self-assembly and self–organization of multimeric intracellular protein structures, such as the cytoskeleton.

A variety of models have been reported (summarized in Table 1) that examine the role of cell architecture and molecular motors in the self-assembly of the cytoskeletal network. A simple phenomenological model has been proposed that predicts the distribution of bound integrin complexes, and was validated in a square fibroblast cell [134]. This model explains possible mechanisms behind the higher concentration of focal adhesions (FA) at the edges and corners of cells (Table 1, column 2). While this simple phenomenological model lacks the features to predict fiber distributions in more complex cell shapes, it provides insight into actin cytoskeletal dynamics without taking into

account the mechanical interactions between the substrate, integrins, and the cytoskeleton. Finite element models that include these interactions can replicate myofibril distributions in several epithelial and fibroblast cell shapes [135, 136]. A chemo-mechanical model that explores the FA complex formation without modeling the cell as a whole produces a detailed prediction of both stresses and strains in the FA [137](Table 1, column 3). These models predict the simple assembly of the actin network or integrin clustering in the vicinity of the focal adhesion in cells with simple cytoskeletal architecture. However, the assembly of myofibrils in cardiac myocytes represents a more challenging phenomenon to model due to its heightened complexity. Cardiomyocytes, like skeletal muscle, are striated myocytes that utilize the actin cytoskeleton as a scaffold for the clustering and assembly of other proteins in sarcomeres, aligned serially in a contractile structure known as the myofibril. To date, most models of myofibrillogenesis are qualitative and give detailed descriptions of how sarcomeric proteins sequentially appear in the sarcomere. Most computational models of cytoskeletal self- assembly focused on the architecture of the actin cytoskeleton and were not designed to recapitulate the rather specialized case of striated muscle, where the maturation from pre-myofibril to nascent myofibrils and their active mutual alignment in cardiomyocytes represent an important developmental step in the spatiotemporal coordination of rhythmic, cellular contraction and ordered cardiac myocyte shortening.

We reported a model that describes the kinetics of myofibrillogenesis in a cardiomyocyte subjected to ECM boundary conditions that impose a particular shape on

Table 1-1: Contrasting features of a selection of myofibrillogenesis computational models.

Comparison of the strengths and weaknesses of a selection of *in silico* models proposed to model the process of myofibril self-assembly.

Model Property	**Novak et al. (2004)**	**Deshpande et al.(2006/(2008)**	**Paszek et al. (2009)**	**Grosberg et al. (2011)**
Model type	Phenomeno-logical	Finite element/ solid mechanics	Chemo-mechanical	Phenomeno-logical
Model compared to cell type	NIH3T3 fibroblasts	Retinal pigment epithelial human cells or fibroblast cells	No specific cell type	Neonatal rat ventricular myocytes
Integrins have a free and bound state (or high/low affinity)	Yes	Yes	Yes	Yes
Focal adhesions more stable with greater	Yes	Yes	Yes	Yes
Myofibrils/stress fibers included in	Yes	Yes	No	Yes
Fiber length-force dependence	No	Not explicitly	No	Yes
Differentiating between pre-myofibril and nascent myofibril	No	No	N/A	Yes
Myofibril actively mutually align	No	No	N/A	Yes
Testing boundary conditions/symmetry breaking	No	No	No	Yes
Detailed model of solid mechanics of the interface	No	Yes	Yes	No
Substrate mechanical load	No	Yes, but not the deformation of the substrate	Yes and Detailed, i.e. both stress and strain - deformation	Yes, but very simply (only traction)
Computationally complex	No	Yes	Yes	No

the cell as the product of cooperative interaction between focal adhesions and premyofibrils, along with parallel bundling of nascent myofibrils [138] (Table 1, column 4). This model, borrowing from Novak et al.'s model of focal adhesion distribution, was tested with *in vitro* experiments conducted on engineered NRVMs to gauge its effectiveness in predicting the architecture of the myofibrillar network in response to extracellular boundary conditions, i.e. cell shape. Unlike previous models, ours accounted for the increased force produced by longer myofibrils and their active parallel coupling. As a result, our model predicted the steady state localization of focal adhesions. Additionally, our model showed that, in the absence of symmetry breaking boundary conditions, the myofibrillar network requires a longer period of time to self-organize into a steady state configuration. Thus, the cell never polarizes unless parallel coupling of the myofibrils is appropriately accounted for.

For example, a neonatal mouse ventricular myocyte seeded on a micro-patterned square fibronectin island in culture will reliably self-organize to have a distinct myofibrillar network, with the myofibrils aligned along the diagonals of the square, anchored at the corners by focal adhesions (Figure 1-3Ai)[26, 138, 139]. Further, when seeded on FN islands with homogenous boundary conditions, the myocytes can potentially polarize in an arbitrary direction (Figure 1-3Aii)[26, 138, 139]. Using a combination of *in vitro* and *in silico* methods, we show that, in the presence of mutual alignment of myofibrils, it is possible to predict the polarization of cells on islands with both homogenous and non-homogenous boundary conditions for cardiomyocytes from multiple species (Figure 1-3B)[138].

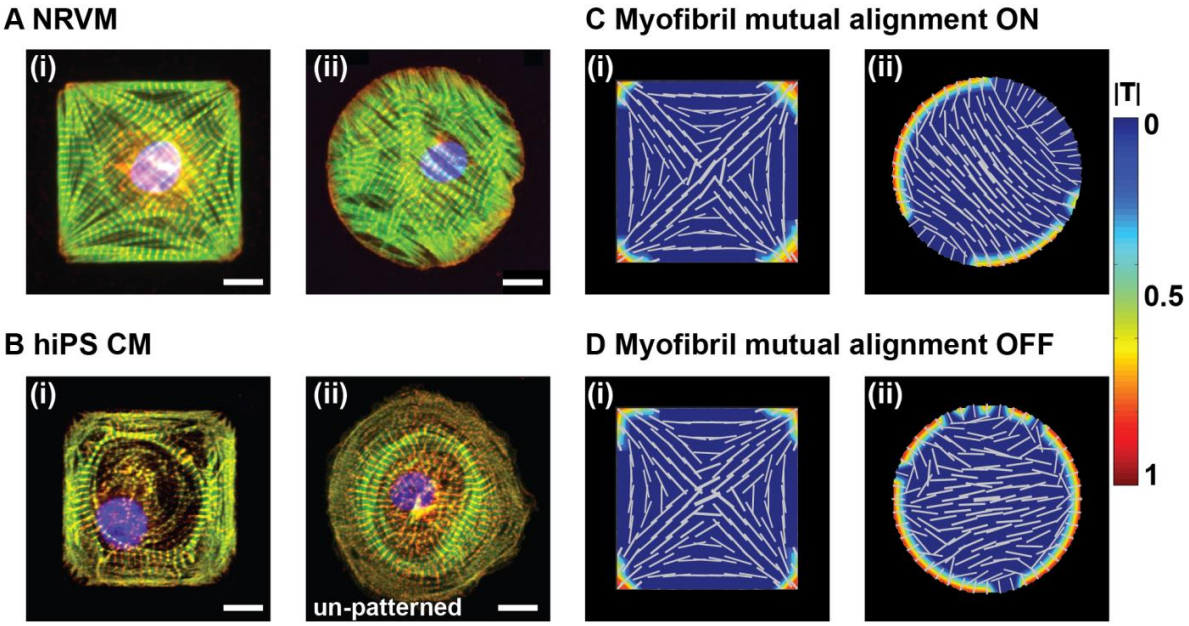

Figure 1-3: Comparison of myofibrillogenesis observed in primary and stem cell-derived cardiomyocytes *in vitro* with *in silico* simulations.

(A) NMVM on patterned FN at day 3 after seeding (i) square, (ii) circle; (B) Computational model of a (i) square and (ii) circular cell with myofibril mutual alignment turned on showing polarization in both cell shapes; (C) human iPS-derived cardiomyocytes on (i) patterned FN square, and (ii) isotropic FN; (D) Computational model of a (i) square and (ii) circular cell with myofibril mutual alignment turned off showing polarization only in the cell type with non-homogenous boundary conditions; (A, C) scale bar = 10 μm; (B, D) color bar shows normalized traction stress (|T|) see [138] for details on the model.

Commercially available human iPS-derived cardiomyocytes (hiPS-CM) do not polarize on a square FN island, but instead the myofibrils take on a circular architecture with no single direction (Figure 1-3Ci). Furthermore, these cells, when seeded on isotropic FN, often take on a pin-wheel circular myofibril architecture (Figure 1-3Cii).

The pin-wheel architecture is reminiscent of the non-polarized circular cell produced by the model with mutual parallel coupling of the myofibrils turned off (Figure 1-3D). However, the current model is unable to predict the other features lacking in the hiPS-CMs because these cells do not respond to non-homogeneous boundary conditions in the same manner as the *in silico* or primary cardiomyocytes (Figure 1-3Bi & 3Di). This example illustrates the gap in knowledge between our current observations of stem cell differentiation and maturation *in vitro* and the state of the art in computational modeling of post-translational cellular development. It is intended to elucidate the potential role of cellular mechano-modeling in understanding developmental cell biology.

In addition to mathematical descriptions of single cell *in vitro* model systems, researchers have also begun to develop computation simulations of tissue- and organ-scale *in vivo* myocardial environments to guide the development of engineered tissues for therapeutic applications [140]. A multi-scale mathematical model of strain-driven eccentric growth and stress-driven concentric growth of the myocardium during ischemic injury has been reported that allows researchers to explore the effects of local changes in stress/strain distribution caused by fibrosis on cardiac function [141]. These models suggest a foundation for quantitative descriptions of the role that mechanical forces play in the self-assembly of myocardial cells into contractile tissues and serve to guide researchers in developing microenvironments that give rise to engineered myocardial tissues that can be used to accurately simulate the function of the heart *in vitro*. However, none of these models have been applied to stem-cell derived cardiomyocytes, and as the unique physiology of these cells pose new challenges to our understanding of cellular

self-assembly, it is essential that the modeling community provide support by creating new mathematical descriptions of these phenomena.

1.7 Conclusions

Physical micro-environmental cues are believed to be fundamental to proper myocardial development and may be a necessary component to experimental strategies for constructing accurate heart tissue analogs from stem cell-derived cardiomyocytes in the laboratory. Mechanical signals are received by cells through integrin-ECM interactions and intercellular junctions, where they are transmitted across the cytoskeleton to intracellular relays that activate intracellular biochemical processes. To fully realize the impact of mechanical cues on cardiac development, further research is necessary to tease apart the contributions of soluble cytokines and physical perturbations to myocardial lineage specification and determine how to incorporate appropriate mechanical cues into existing *in vitro* model systems. While the details of mechanotransduction remain to be fully elucidated, researchers have developed a basic understanding of the role that the cytoskeleton plays in this signaling modality, and are beginning to use this information to create custom ECM microenvironments that utilize the integrin-ECM interface and intercellular junctions to modulate engineered myocardial tissue form and function. However, these engineered tissues are typically much less sophisticated than their *in vivo* counterpart, consisting of two-dimensional monolayers of a homotypic cell population cultured on a matrix comprised of a single type of ECM protein. To better recapitulate the native myocardium, it will be necessary to develop new methods for fabricating 3-dimensional tissue constructs with the same diversity in

ECM protein composition and cellular phenotypes. Furthermore, mathematical models are emerging that quantitatively describe the effects of mechanical cues on cellular processes, such as myofibrillogenesis and contractility. Refinement of these mathematical models to capture the complex interplay between large populations of heterotypic cells interacting in a three-dimensional matrix, combined with experimental techniques to recapitulate the *in vivo* microenvironment, may provide researchers with the necessary tools to fabricate artificial myocardial tissue constructs with equivalent structural and functional characteristics to natural heart tissue, and replace costly animal models of cardiotoxicity with cheaper, human-relevant *in vitro* alternatives.

2 Tissue Anisotropy Promotes an Adult-Like Phenotype in Engineered Myocardium

Specification and maturation of the specialized myocardial lineages comprising the working myocardium arise from the integration of multiple dynamic chemical and mechanical signaling cues present during pre-natal heart development. Advances in the field of cellular biomechanics are beginning to explain how physical forces and mechanical structures impact information processing and cellular decision making during organogenesis (reviewed in [142]). In the musculature of the heart, interactions between cardiomyocytes and the extracellular matrix (ECM) give rise to changes in cell shape and tissue architecture that have vast influence over its functional performance under both physiological and pathological conditions [11, 14, 143]. We hypothesized that fabricating engineered cardiac tissues to mimic the anisotropic architecture of the ventricular myocardium promotes *in vitro* maturation toward the adult phenotype. To test this hypothesis, we constructed anisotropic 2D engineered tissues comprised of neonatal rat ventricular myocytes (NRVMs) and compared their gene expression profile, myofibril architecture, and contractility to tissues comprised of randomly organized NRVMs that are typically used for *in vitro* studies, and to the adult rat myocardium. We found that anisotropic engineered myocardium exhibited a gene expression profile, sarcomere organization, and contractile output that recapitulated what was observed in the adult rat myocardium, while isotropic NRVM monolayers did not. The results of this study provide evidence supporting the role of cell-ECM interactions in promoting cardiomyocyte maturation *in vitro*. These results may provide valuable insight for

building engineered cardiac tissues that more accurately represent the native myocardium for *in vitro* cardiotoxicity assays and regenerative medicine applications.

2.1 Introduction

Cardiomyocytes are the basic working unit of the myocardium and exist as a diversity of functional subtypes whose performance characteristics are tuned to the developmental stage of the heart as well as their specific location [15]. As embryonic development proceeds, cardiac progenitor cells are organized into increasingly complex and compartmentalized structures and are exposed to a myriad of mechanical strain regimens arising from the contraction of the muscle tissue as it adapts to the increasing pressure it must work against to propel blood through the expanding circulatory system. To date, there has been a tremendous amount of insight gained on the earliest stages of heart development, but much remains to be elucidated about the mechanisms of fetal and post-natal cardiomyocyte maturation [15]. During myogenesis, the heart begins as a tube then loops to become a four chambered heart [144]. As the architecture of the heart self-organizes into sheets of laminar muscle wrapping around the two ventricular cavities [145-147], cardiomyocytes experience different mechanical cues, and they continue to mature post-natally [118, 148]. *In vitro*, such changes have been shown to impact the contractile and electrophysiological function of cardiomyocytes even in two-dimensional monolayers [100, 149]. The change in functional output suggests an *in vitro* maturation of the cells, but has not been systematically confirmed.

A failure to detect cardiotoxicity of drugs during the initial *in vitro* screening process is one of the leading causes of the high attrition rate of drugs [150]. Standard

screening assays would hold more predictive power if they were based on more adult cardiomyocyte phenotypes, yet neonatal cardiomyocytes are more plastic and can be used in a wider range of assays [150, 151].The electrophysiological properties of the rat heart during development have been extensively studied [152-155]. It has been shown that at the neonatal stage the cardiomyocytes mainly express T-type calcium channels [153], while adult rat myocytes express L-type calcium channels [154]. This has significant implications on the shape of the action potential [155], and therefore on the accuracy of neonatal *in vitro* models in predicting cardiotoxicity of drugs. It is also known that the contractile apparatus of the cardiomyocytes matures during development [156, 157]. Measuring contractility of isolated cardiomyocytes with a neonatal phenotype introduces a risk of missing a drug's impact on contractility because the weak contraction might mask the effect. We have previously shown that extracellular cues can be used to guide myofibrillogenesis [26, 104, 139, 158]. These reports suggest that geometrical cues might play an important role in inducing a more mature phenotype thus positively affecting function.

We reasoned that if we used extracellular matrix (ECM) patterns to guide the tissue to self-assemble to mimic the organization of the adult myocardium both the function and levels of relevant gene expression have to approach a more adult phenotype. To this end, we quantitatively compared the organization of sarcomeres in the isotropic NRVM tissues, aligned NRVM engineered tissues, and the adult myocardium. We then confirmed the impact of different intracellular organization on contractile function. Finally, we showed the corresponding change in the expression level of genes that impact cardiomyocyte tissue function. This illustrates that the changes in function are not simply

an effect of geometry, but they have underlying biological implication. Taken together, these results show the potential of utilizing physical microenvironmental cues to create *in vitro* models of the myocardium that provide patient-relevant physiological output.

2.2 Results

2.2.1 Comparison of Sarcomere Organization in Engineered and Adult Myocardium

Previous studies have shown that tissue architecture influences a number of functional aspects of engineered myocardium, such as Ca2+ transient dynamics, electrical activity, and contractile stress generation [158-160]. However, it is still unclear how closely the physiological characteristics of these engineered heart tissues match those of the native myocardium and what role tissue architecture plays in influencing these properties. To examine the relationship between tissue architecture and in vitro maturation of engineered myocardium, we used micro-contact printing (Figure 2-1A) to fabricate cell culture substrates with ECM patterns designed to promote parallel myocyte alignment. As a control, we cultured isolated cardiac myocytes substrates coated with a uniform layer of fibronectin (FN), in the manner typically used for in vitro studies, that provided no specific geometric guidance cues to the cells (Figure 2-1B). In contrast, we designed two ECM patterns, 15 μm wide lines of FN spaced 15 μm apart (Figure 2-1C), and 15 μm wide lines of FN spaced 2 μm apart (Figure 2-1D) that present cultured myocytes with boundary conditions intended to orient them into laminar architectures. The 15 μm wide lines spaced 15 μm apart (In vitro Lines) pattern was designed to impose

the highest degree of parallel alignment by forcing the cardiac myocytes to grow on FN lines just wide enough for them to attach to the substrate end-to-end and form parallel

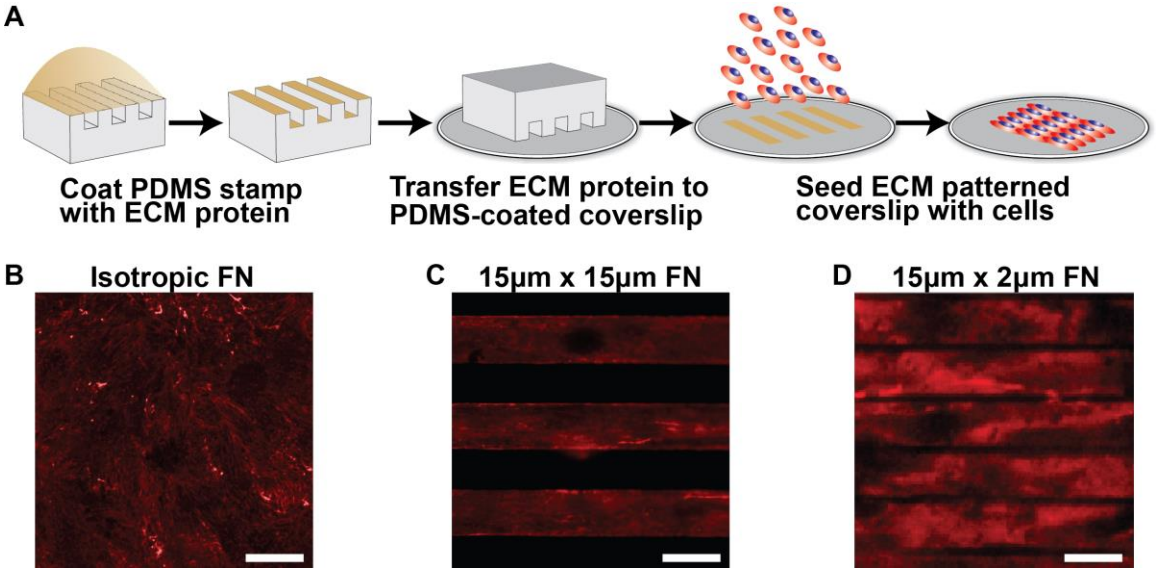

Figure 2-1: Regulation of engineered myocardium tissue architecture using micro-contact printed extracellular matrix.

(A) The architecture of engineered cardiac tissues was regulated by micro-contact printing the ECM protein fibronectin (FN) onto PDMS-coated coverslips into the desired pattern. Cardiac myocytes seeded onto these micropatterned FN substrates self-assembled into tissues according to the pattern encoded in the ECM. Three distinct ECM patterns were chosen for this study to assess the contribution of tissue architecture to the maturation of engineered myocardium in vitro. Fluorescence images of (B) unpatterned, isotropic FN coated coverslip, (C) micro-patterned 15 μm wide FN lines spaced 15 μm apart to create linear arrays of cardiac myocytes arranged end to end, and (D) micro-patterned 15 μm wide FN lines spaced 2 μm apart to create confluent, anisotropic sheets of cardiac myocytes. All scale bars = 10 μm.

arrays of muscle fibers. However, the spacing in between these linear constructs does not give rise to engineered myocardium that accurately recapitulate the sheet-like architecture of the myocardium, so we designed a second pattern of 15 μm wide lines of FN spaced 2 μm apart (*In vitro* Aniso) that forces the cardiac myocytes to align in a parallel fashion, while still allowing transverse coupling between neighboring cells. To assess the influence of ECM guidance cues on the myofibril architecture of engineered myocardium, immunofluorescence imaging of sarcomeric α-actinin was used to visualize z-line orientation. NRVMs cultured on isotropic FN substrates (*In vitro* Iso) self-assembled into monolayers with random cellular organization, as judged by the spread in the z-line orientation angles observed in the α-actinin micrographs (Figure 2-2Ai). In contrast, NRVMs cultured on micro-patterned 15 μm wide lines of FN spaced 15 μm apart (Figure 2-2Aii), and 15 μm wide lines of FN spaced 2 μm apart (Figure 2-2Aiii) exhibited high degrees of uniaxial, parallel z-line alignment. Sarcomeric α-actinin immunofluorescence imaging of longitudinal sections taken through the adult rat ventricular myocardium (Figure 2-2Aiv) revealed that the z-line organization observed in the *In vitro* Line and *In vitro* Aniso engineered myocardium resembled the pattern observed in the adult myocardium. To quantitatively compare the differences in global z-line alignment between the different conditions, custom image processing software was used to measure the orientation angles of the z-lines observed in the α-actinin micrographs and use those angles to calculate the orientational order parameter (OOP) for each tissue architecture [160]. The OOP can take on a value between zero, representing completely random organization, and one, representing perfect parallel alignment, that we used to perform statistical comparisons of global sarcomere alignment between our engineered

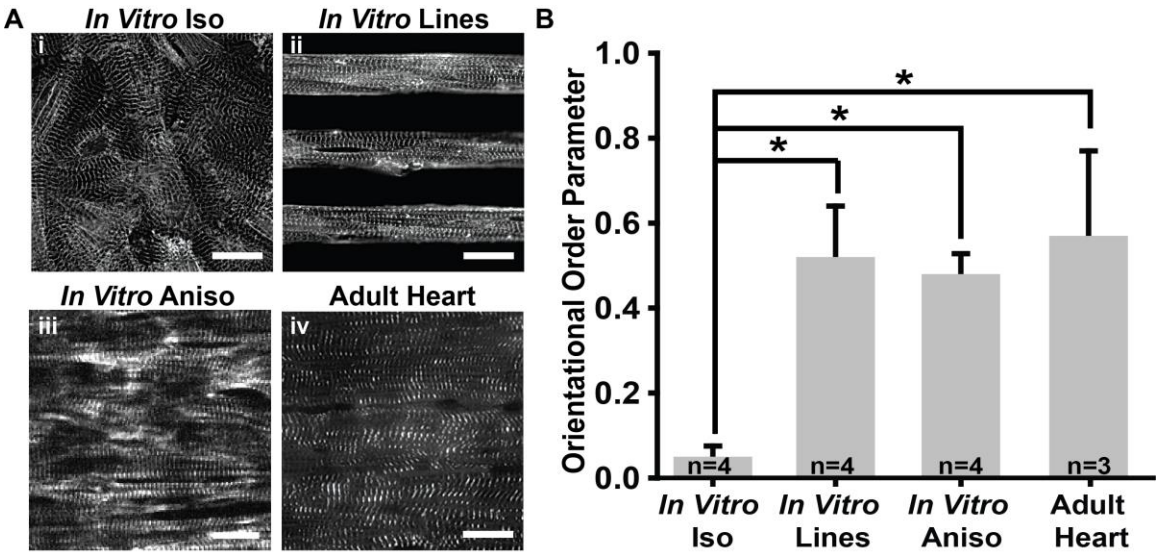

Figure 2-2: Quantification and comparison of global sarcomere alignment in engineered and adult myocardium.

(A) NRVMs seeded onto FN coated PDMS substrates self-assembled into tissues according to the pattern encoded in the ECM. Fluorescence imaging of sarcomeric α-actinin revealed (i) random z-line orientation in cardiac myocytes cultured on isotropic FN substrates, but a high degree of parallel alignment in cardiac myocytes cultured on (ii) 15 μm wide FN lines spaced 15 μm apart, and (iii) 15 μm wide FN lines spaced 2 μm apart similar to what is observed in (iv) histological sections of the adult rat ventricular myocardium. (B) Statistical comparison of global sarcomere alignment quantified using the Orientational Order Parameter (i.e. a value of 1 indicates perfect parallel alignment, whereas a value of 0 indicates completely random alignment) reveals that the isotropic engineered tissues exhibited significantly lower global z-line alignment than both of the micro-patterned anisotropic engineered tissues, as well as, the adult rat myocardium. In contrast, the anisotropic engineered myocardium showed similar levels of alignment to the adult rat ventricular myocardium. * = $p < 0.05$ vs. In vitro Iso. All scale bars = 10 μm.

myocardium and histological sections of adult rat myocardium (Figure 2-2B). The sarcomeric OOP of the *In vitro* Iso engineered tissues was close to zero, corresponding to the large distribution of z-line orientation angles observed in these samples. In contrast, the sarcomeric OOP values for the In vitro Lines and In vitro Aniso engineered myocardium were significantly higher ($p<0.05$) than those observed in the In vitro Iso tissues. Moreover, the adult rat heart exhibited a sarcomeric OOP value that was significantly higher ($p<0.05$) than the In vitro Iso engineered tissues, but closely matched the OOP values for the In vitro Lines and In vitro Aniso engineered myocardium. These results indicate that the guidance cues encoded in micro-patterned ECM promote sarcomere organization reminiscent of what is found in the in vivo myocardium, potentially giving rise to engineered myocardium that better recapitulate the myofibril architecture of the adult heart than traditional isotropic cultures.

2.2.2 Comparison of Engineered and Adult Myocardium Gene Expression Profiles

Alterations in cardiomyocyte shape mediated by cytoskeletal remodeling have been shown to influence gene expression during cardiac morphogenesis [16, 18, 19]. We postulated that recapitulating the cellular architecture and parallel alignment observed in the *in vivo* myocardium would influence the expression of cardiac genes *in vitro* toward expression levels observed in the post-natal myocardium. To test this, we performed real-time qPCR measurements of the expression of a panel of genes associated with myocardial development and function (See table in Appendix 6-2) in isotropic NRVM monolayers and micropatterned lines of NRVMs at day 4 in culture when structural and

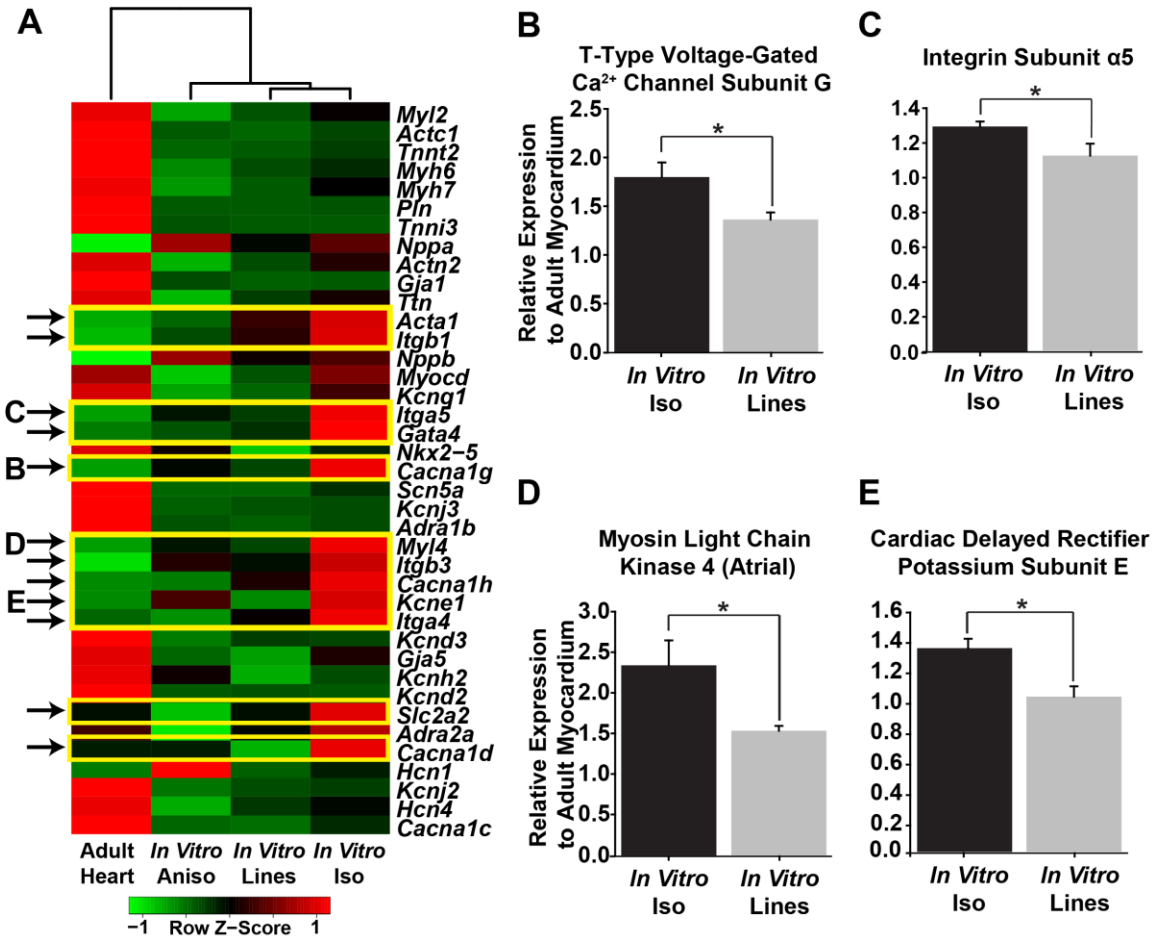

Figure 2-3: Comparison of gene expression profiles in engineered and adult rat myocardium.

Real-time qPCR measurements were made for a panel of genes associated with myocardial development (see Appendix 6-2) on isotropic and micropatterned lines of NRVMs, as well as explants from the ventricular myocardium of 2 month old rats. (A) Heatmap illustrating hierarchical clustering of the three myocardial tissue types based on mean 2-ΔCt expression values. Genes highlighted in yellow and indicated with arrows demonstrated expression profiles wherein the expression levels of the adult myocardium samples and micropatterned line NRVM tissues were very similar to each other, but different from the expression levels of the isotropic NRVM samples. Fold change versus

(Continued) adult myocardium was computed for this set of genes in the isotropic and micropatterned line NRVM samples and statistical comparison revealed a number of significantly differentially expressed genes between the two types of in vitro cardiac tissues, including (B) atrial myosin light chain kinase (Myl4), (C) integrin α5 (Itga5), (D) T-type calcium channel subunit G (Cacna1g), and (E) cardiac delayed rectifier potassium subunit E (Kcne1) that may have important implications for the effects of tissue architecture on myocardial development in vitro. n=3 for all samples, * = $p<0.05$. Data presented as mean ± S.E.M.

functional characterization were performed. In addition, real-time qPCR measurements of these genes were carried out on explanted tissue samples from the ventricular myocardium of 3 month-old Sprague Dawley rats to serve as a reference profile of mature cardiac gene expression. Hierarchical clustering analysis of the *in vitro* isotropic, *in vitro* lines, and adult ventricular muscle gene expression profiles (Figure 2-3A) revealed a number of genes with expression levels that were similar between the *in vitro* lines engineered tissues and the adult ventricular heart tissues, but substantially different from the *in vitro* isotropic tissues (highlighted in yellow boxes). Calculation of fold change versus adult myocardium in the *in vitro* isotropic and *in vitro* lines samples for this set of genes revealed a number of significantly-differentially expressed ($p<0.05$) genes that play important roles in myocardial development (Figure 2-3B-E).

2.2.3 Comparison of Contractile Stress Generation in Engineered and Adult Myocardium

The characteristic shape and organization of cardiac myocytes in the myocardium has been shown to have a strong association with the contractile output of the heart during the progression of both normal development and disease [14, 123]. Therefore, the tissue with better aligned sarcomeres was expected to generate more force than tissues with isotropic sarcomeres. The relationship between tissue architecture and contractility was assessed in our engineered myocardium using the muscular thin film (MTF) contractility assay recently developed in our laboratory [149, 161]. These MTF constructs consisted of a layer of cardiac myocytes cultured on top of thin, rectangular elastic films attached to a glass coverslip. Once the free edges of the MTFs were released from the coverslip, shortening of the cardiac myocytes during each contraction cycle caused the films to bend up out of the plane of the coverslip, with the MTFs lying flat against the substrate during diastole, and at maximum curvature during peak systole (Figure 2-4A). High speed imaging of film curvature allowed visualization of the temporal profile of MTF bending, and was used to calculate the amount of contractile stress generated by the engineered myocardium attached to it [161]. Isotropic monolayers of NRVMs exhibited a flat contractile stress profile, indicative of the inability of the randomly organized cardiac myocytes to generate a substantial amount of uniaxial contractile stress capable of bending the MTF cantilever (Figure 2-4Bi). In contrast, the more highly aligned *In vitro* Lines (Figure 2-4Bii) and *In vitro* Aniso (Figure 2-4Biii) engineered myocardium demonstrated contractile stress profiles indicative of greater contractile stress generation

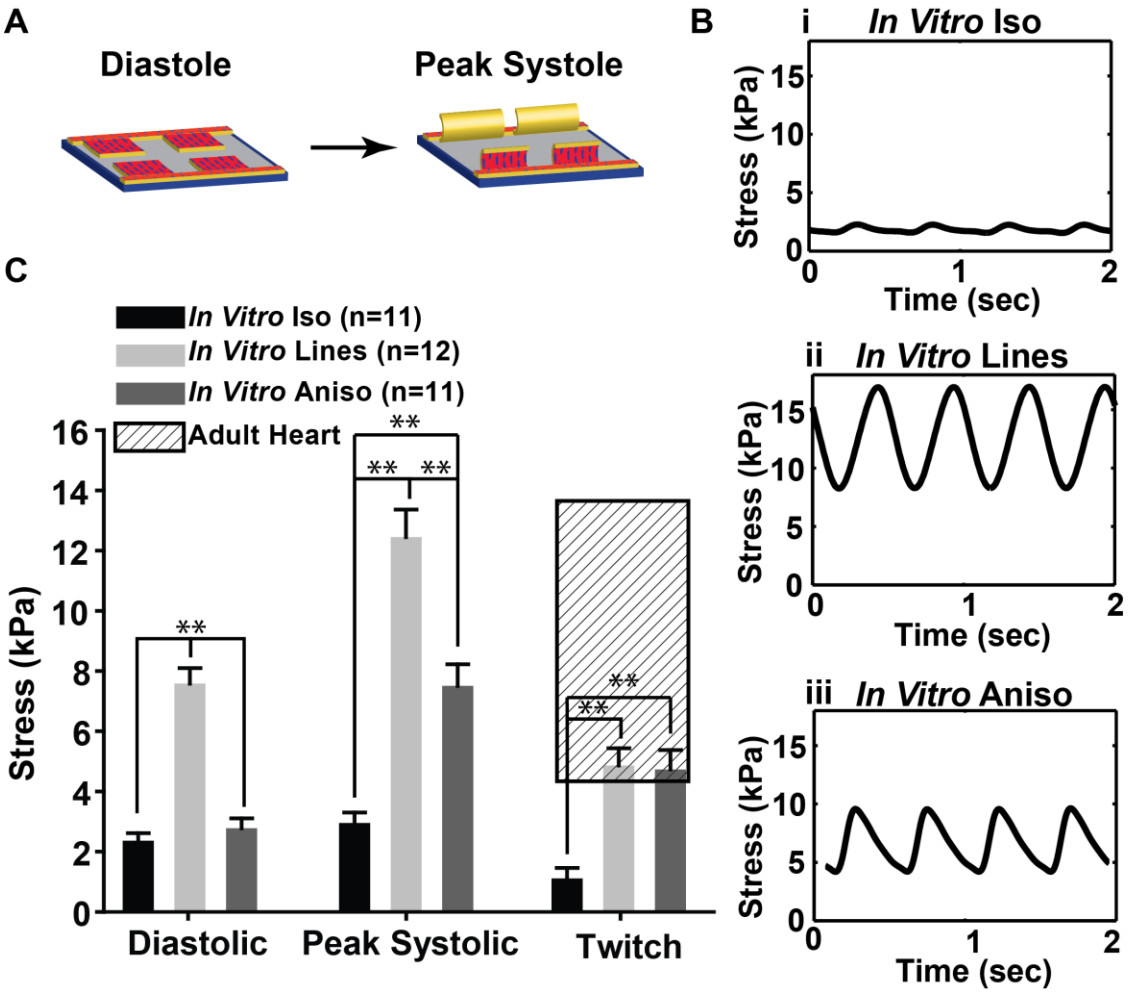

Figure 2-4: Measurement and comparison of contractile performance in engineered and adult rat myocardium.

(A) Schematic representation of the muscular thin film (MTF) contractility assay. Engineered myocardium is cultured on elastomeric cantilevers that lay flat during diastole and curl up during systolic contraction. (B) High speed video recording allows calculation of stress traces during contraction cycles. Example stress traces for engineered tissues (i-isotropic, ii – engineered lines); (C) Comparison of diastolic (rest), peak systolic (maximum contraction), and active (difference between systolic and diastolic) stresses. Each type of stress is significantly different between lines and

(Continued) isotropic tissues ($p<0.001$) (lines n=12 films, #chips=3; isotropic n=11 films, #chips = 3). Data presented as mean ± S.E.M.

with temporal profiles consistent with the 2 Hz pacing stimulus applied to them during the experiment. Statistical comparison of the diastolic and peak systolic stresses generated by the *In vitro* Iso, *In vitro* Lines, and *In vitro* Aniso engineered myocardium revealed that the *In vitro* Lines and *In vitro* Aniso engineered tissues both generated significantly ($p<0.05$) higher values than the *In vitro* Iso tissues (Figure 2-4C). Comparison of the twitch stress (*i.e.* the difference between the diastolic and peak systolic stresses) generated by each type of engineered tissue revealed that the *In vitro* Lines and *In vitro* Aniso engineered tissues both generated significantly ($p<0.05$) higher values than the *In vitro* Iso tissues. Furthermore, comparison of the twitch stress values for the engineered myocardium to those reported in the literature for ventricular papillary muscle strips showed that the *In vitro* Lines and *In vitro* Aniso, but not *In vitro* Iso engineered cardiac tissues exhibited values within the same range [162-164]. Taken together, these results indicate that the anisotropic myofibril architecture imposed by the micro-patterned ECM cues give rise to engineered myocardium with contractile performance on par with isolated adult papillary muscle strips commonly used for studies of cardiac contractility and inotropic response to drug compounds [165].

2.3 Discussion

In this study, we asked if anisotropic engineered myocardium comprised of isolated NRVMs cultured on micro-patterned ECM substrates could recapitulate the

phenotype of the adult rat ventricular myocardium. We have previously shown that geometric cues encoded in the ECM can be used to precisely direct sarcomere organization *in vitro*, [138] and that parallel alignment of sarcomeres directly influences the contractile performance of engineered NRVM myocardium [160]. This study provides the first evidence that the sarcomere organization and contractile stress generation in engineered myocardium matches the adult myocardium. We have quantitatively shown that it is possible to tissue-engineer cardiomyocyte two-dimensional cultures that are similar to adult myocardium in their distributions of sarcomere orientation. This architectural design has implications in the possible force generation of the constructs built with these cells. Gene expression analysis reveals that tissue architecture influences cardiac gene expression, with aligned cardiomyocytes demonstrating an expression profile that more closely resembles the adult expression profile than poorly organized cardiomyocytes, supporting the role of cell-ECM interactions in promoting cardiomyocyte maturation *in vitro*.

These results suggest that two-dimensional micropatterning, which gives intricate control over cell and tissue architecture, is sufficient to cause an apparent maturation in isolated cardiomyocyte culture. It has been shown previously that three-dimensional substrates can induce a genetic change in the cells [166], but our results suggest that it is not necessary to provide a three-dimensional environment to induce such changes. Indeed providing two-dimensional ECM cues is sufficient to direct self-assembly of specific myofibril architecture [158], and therefore affect function through both cell geometry and gene expression.

A significant body of research exists on the earliest stages of heart development, but much remains to be elucidated about the maturation of cardiomyocytes from the late fetal stage onwards. The results of this study provide evidence supporting the role of cell-ECM interactions in promoting cardiomyocyte maturation *in vitro*. These results may provide valuable insight for building engineered cardiac tissues that more accurately represent the native myocardium for *in vitro* cardiotoxicity assays and regenerative medicine applications.

2.4 Materials and Methods

2.4.1 Cell Culture Substrate Fabrication

2.4.1.1 Photolithography

Photolithographic masks with 15 µm wide ridges separated by 15 µm wide grooves, or 15 µm wide ridges separated by 2 µm wide grooves for microcontact printing were designed in AutoCAD (Autodesk Inc., Mill Valley, CA) and fabricated at the Center for Nanoscale Systems facility. Silicon wafers (Wafer World, West Palm Beach, FL) were spin-coated with SU-8 2002 negative photoresist (MicroChem Corp., Newton, MA) were exposed to ultra-violet light for 4 seconds. Uncross-linked photoresist was removed by rinsing in propylene glycol methyl ether acetate, followed by rinsing in isopropyl alcohol, and drying with a nitrogen gun. Wafers were treated with Tridecafluoro-1,1,2,2-tetrahydroctyl-1-trichlorosilane (UCT Specialties, Bristol, PA) under vacuum for approximately 12 hours prior to PDMS stamp molding to allow easy separation of the cured PDMS from the wafer during stamp fabrication.

2.4.1.2 Cell Culture Substrate Fabrication

For all experiments except contractility measurements, substrates were manufactured from 25 mm glass cover slips cleaned by sonication in 50% ethanol in distilled, deionized water for 30 minutes, then air dried. Sylgard 184 (Dow Corning, Midland, MI) polydimethylsiloxane (PDMS) elastomer was mixed with the curing agent (10:1 w/w), and the mixture was spin-coated onto the cover slip (4000 rpm ramp protocol over 2 minutes). The PDMS was allowed to cure at 65ºC for at least 12 hours before use.

2.4.1.3 Muscular Thin Film Substrate Fabrication

For contractility experiments, muscular thin film (MTF) chips were made by covering a large section of glass (7.5x11 cm) on both sides with a protective film (Static Cling Film, McMaster-Carr, Robbinsville, NJ). Strips of 5-8 mm were removed from the top protective film using a razor blade, and then an excess of poly(N-isopropylacrylamide), (PIPAAm, Polysciences, Inc., Warrington, PA), dissolved in 99.4% 1-butanol at 10%wt (w/v), was deposited onto the exposed glass. After the PIPAAm was spin coated at 6000 rpm for one minute, the remaining strips of the protective film were removed from the top of the glass. PDMS was pre-cured at room temperature for 2-4 hours before being spin coated onto the whole glass section. After the PDMS was cured for at least 12 hours, the bottom protective film was removed, and the glass sections were cut into cover slips (~1.5 x 1.2 mm) with a diamond glass cutter.

2.4.1.4 Micro-contact Printing

Silicone stamps designed to have a pattern consisting of 15 μm wide ridges separated by 15 μm wide grooves were sonicated in a 50% solution of ethanol in distilled,

deionized water for 30 minutes. The stamps were then air dried within a biosafety cabinet to maintain sterility. The patterned surface of the sterilized stamps was coated with a 50 µg/mL solution of fibronectin (FN)(BD Biosciences, Sparks, MD) in distilled, deionized water. The FN solution was incubated on the stamps for one hour at room temperature within a biosafety cabinet. The FN was then transferred from the surface of the stamp to the PDMS surface of PDMS-coated coverslips that had been UVO treated for 8 minutes prior to the transfer (UV ozone Model No. 342, Jelight Company, Inc., Phoenix, AZ). For MTF constructs the pattern was placed perpendicular to the PIPAAm strips visible under the PDMS. After transfer of the patterned FN, the cover slip was coated with a sterile 1% wt/vol solution of Pluronics F-127 (BASF, Florham Park, NJ) in distilled deionized water at room temperature for 10 minutes to prevent cell adhesion to unstamped regions of the substrate. For isotropic constructs, cover slips that have been UVO treated for 8 minutes were submerged in 50µg/mL FN for 1 hour at room temperature. All cover slips were rinsed three times with sterile room temperature PBS (Invitrogen, Carlsbad, CA) prior to cell seeding.

2.4.2 Cardiac Myocyte Isolation and Culture

2.4.2.1 Neonatal Rat Ventricular Myocytes

Ventricular myocytes were isolated from 2-day old Sprague Dawley rats (Charles River Laboratories, Wilmington, MA) in accordance with procedures approved by the Harvard University Animal Care and Use Committee. Briefly, excised ventricular tissue was incubated in a 0.1% (w/v) trypsin (USB Corp., Cleveland, OH) at 4°C for 12 hours with agitation. Ventricular tissue was subsequently dissociated into a single cell

suspension via serial 2 minute incubations in a 0.1% (w/v) solution of collagenase type II (Worthington Biochemical, Lakewood, NJ) at 37º C. Two 45 minute pre-plating steps were used to enrich the cardiac myocyte population. Isolated cardiac myocytes were maintained in a culture medium consisting of Medium 199 (Invitrogen, Carlsbad, CA) supplemented with 10% (v/v) heat-inactivated fetal bovine serum (FBS), 10 mM HEPES, 20 mM glucose, 2 mM L-glutamine, 1.5 µM vitamin B-12, and 50 U/ml penicillin and seeded at a density of 200,000 cells/cm^2. The FBS concentration was reduced to 2% (v/v) from the second day of culture onward, and medium was exchanged every 48 hours.

2.4.2.2 Adult Rat Ventricular Myocytes

For qPCR gene expression measurements, 1 mm^3 samples of left ventricular myocardium weighing between 20-25 mg were surgically excised from 3 month old female Sprague Dawley rats (Charles River Laboratories, Wilmington, MA). Tissue samples were submerged in ice cold lysis buffer immediately after isolation and homogenized using a LabGEN 125 soft tissue homogenizer (Cole-Parmer, Vernon Hills, IL).

2.4.3 Real-Time qPCR Gene Expression Measurements

Total RNA was collected in triplicate from isotropic and micropatterned anisotropic samples using an RNeasy mini kit (Qiagen Inc, Valencia, CA) according to the manufacturer's instructions, and in triplicate from 3 month old Sprague Dawley rat ventricular tissue using an RNeasy mini fibrous tissue kit (Qiagen Inc, Valencia, CA). Genomic DNA contamination was eliminated by incubating the RNA lysates in DNase I

digestion buffer at 37ºC for 15 minutes during the RNA purification procedure. The quantity and purity of RNA lysates was assessed using a Nanodrop spectrophotometer (Thermo Scientific, Wilmington, DE). Purified total RNA lysates with OD 260/280 ratios greater than 1.8 were used for RT-qPCR measurements. Complementary DNA strands were synthesized for genes of interest using an RT2 first strand synthesis kit (Qiagen Inc, Valencia, CA). 500 ng of total RNA were used from each lysate for each first strand synthesis reaction. Expression levels for specific genes of interest were measured using custom RT2 Profiler RT-PCR arrays (Qiagen Inc, Valencia, CA) and a Bio-Rad CFX96 RT-PCR detection system (Hercules, CA). Statistical analysis of RT-qPCR threshold cycle data was carried out with the web-based RT2 Profiler PCR Array Data Analysis Suite version 3.5 (Qiagen Inc, Valencia, CA) according to published guidelines [167].

2.4.4 Immunohistochemical Labeling and Fluorescence Imaging

2.4.4.1 Neonatal Rat Ventricular Myocyte Engineered Myocardium

Samples were fixed in 4% (v/v) paraformaldehyde with 0.05% (v/v) Triton X-100 in PBS at room temperature for 15 minutes. Cells were incubated in a solution containing 1:200 dilutions of monoclonal anti-sarcomeric α-actinin antibody (A7811, clone EA-53, Sigma Aldrich, St. Louis, MO), polyclonal anti-fibronectin antibody (F3648, Sigma-Aldrich, St. Louis, MO), 4',6'-diamidino-2-phenylindole hydrochloride (DAPI, Invitrogen, Carlsbad, CA), and Alexa Fluor 633-conjugated phalloidin (Invitrogen, Carlsbad, CA) for one hour at room temperature. Samples were then incubated in 1:200 dilutions of Alexa Fluor 488-conjugated goat anti-mouse IgG and

Alexa Fluor 546-conjugated goat anti-rabbit IgG secondary antibodies (Invitrogen, Carlsbad, CA) for 1 hour at room temperature. Labeled samples were imaged with a Zeiss LSM confocal microscope (Carl Zeiss Microscopy, Jena, Germany).

2.4.4.2 Adult Rat Ventricular Myocardium

Three naïve male Crl:CD (SD) rats (Charles River Laboratories, Inc., Raleigh, NC) aged 10 to 11 weeks were used for immunohistochemical labeling. Rats were euthanized under isoflurane anesthesia and the heart from each rat was removed and bisected longitudinally so that each half contained both the left and right atria and the left and right ventricles. Each half of the heart was embedded in Optimal Cutting Temperature (OCT) media (BD, Franklin Lakes, NJ), snap-frozen with isopentane, and stored at or below -70°C prior to sectioning. Immunohistochemical staining was conducted using a Leica Bond Max IHC stainer. Sections were cut at 5 microns and air dried at room temperature for 2 hours, then fixed in 4% paraformaldehyde for 10 minutes and transferred to Bond wash buffer (TRIS+Tween). Following incubation in Rodent Block R (Biocare Medical) for 15 minutes at room temperature, the primary antibody mouse anti sarcomeric α-actinin (Abcam ab9465) at 1/50 dilution in Bond Antibody Diluent was applied for 60 minutes at room temperature. The secondary antibody incubation consisted of donkey anti-mouse Alexa Fluor 647 (Invitrogen) diluted 1/200 in Bond wash buffer for 30 minutes at room temperature. Between each of these steps, wash buffer rinses were applied 3 times for 2 minutes each. The images were collected in regions of the left ventricle with that showed longitudinal fibers. For each rat heart, six images were collected using the Zeiss 510 Meta Confocal Microscope (Carl Zeiss

Microimaging). All procedures were conducted in accordance with published guidelines (National Research Council's Guide for the Care and Use of Laboratory Animals) and the U.S. Department of Agriculture's Animal Welfare Act and approved by GSK's Institutional Animal Care and Use Committee.

2.4.5 Quantitative Image Analysis of Sarcomere Organization

Global sarcomere organization in engineered myocardium and histology slices of adult ventricular myocardium was measured using immunofluorescence micrographs of sarcomeric α-actinin taken as described above, and processed using custom image analysis software. Fluorescence micrographs were first pre-processed to highlight the filamentous structure of the cytoskeleton using a "tubeness" operator [168] that replaced each pixel in the image with the largest non-positive eigenvalue of the image Hessian matrix. The orientations of sarcomeric α-actinin positive pixels were then determined using an adapted structure-tensor method [169] and the orientational order parameter (OOP), a measure of the global alignment of the sarcomeres, [170] was calculated from the observed orientations. The sarcomere length, defined as the distance between adjacent z-lines, was determined by processing the fluorescence images with a 2D Fast Fourier Transform algorithm.

2.4.6 Muscular Thin Film Contractility Measurements

The muscular thin film (MTF) chips were transferred to a stereomicroscope (Model MZ6 with darkfield base, Leica Microsystems, Inc., Wetzlar, Germany) in a 60 mm Petri dish filled with a normal Tyrode's solution (mM, 5.0 HEPES, 5.0 glucose, 1.8

$CaCl_2$, 1.0 $MgCl_2$, 5.4 KCl, 135.0 NaCl, and 0.33 NaH_2PO_4; reagents from Sigma, St. Louis, MO) at 37ºC. The MTF was cut using a straight-blade razor and excess film was removed to create an array of 2-8 rectangular films over the PIPAAm area of the chip. The rectangular MTFs were 1-2 mm in width, 2-5 mm in length, and were separated by 0.5-1 mm spacing. Once the temperature of the bath equilibrated to room temperature, PIPAAm dissolved and the films were released from the substrate by gently pulling on the corner of each film with a pair of tweezers. As a result the films were attached to the chip by one edge only, and would bend as the cardiomyocyte contracted. The MTF length (prior to peeling the films off) and the projections the MTFs projection on the substrate plane was recorded with a fast camera (120 fps) (A602f Basler Inc, Exton, PA) controlled by LabView (National Instruments, Austin, TX). The cardiomyocytes were paced at 2 Hz (5-10 V, 10 msec pulse) using an external field stimulator (Myopacer, IonOptix Corp., Milton, MA) in a temperature controlled bath (34ºC-37ºC) throughout the experiment.

The stress produced by the engineered cardiac tissues was calculated from the amount of bending of the MTF. The bending was measured as a radius of curvature. Briefly, the length (L) the projection of the MTFs (x) was measured using ImageJ code (NIH). The radius of curvature was numerically calculated according to:

$$x = \begin{cases} r\sin\left(\frac{L}{r}\right) \Rightarrow \frac{2L}{\pi} < x < L \\ r \Rightarrow \frac{L}{2\pi} < x < \frac{2L}{\pi} \end{cases} . \quad (1)$$

The stress produced by the films was numerically calculated using previously described methods [161]. The radius of curvature and the thickness of the PDMS layer of the MTF were input for every film, analyzed by MatLab (Mathworks, Natick, MA) to calculate the stress according to a volumetric growth method [171, 172]. The systolic and

diastolic stresses were calculated as the average of the maxima and minima in the oscillating stress trace, respectively. The active stress was calculated as the difference between the systolic and diastolic stresses.

3 Quality Metrics for Stem Cell-Derived Cardiac Myocytes

Advances in stem cell manufacturing methods have made it possible to produce stem cell-derived cardiac myocytes at industrial scales for *in vitro* muscle physiology research purposes. While FDA-mandated quality assurance metrics exist for safety issues in the manufacture of stem cell-based products, no standardized guidelines currently exist for the evaluation of stem cell-derived myocyte functionality. As a result, it is unclear whether the various stem cell-derived myocyte cell lines on the market exhibit comparable performance to one another, or if any of them accurately recapitulate the characteristics of native cardiac myocytes. We propose a multi-parametric quality assessment rubric where genetic, structural, electrophysiological, and contractile measurements are coupled with comparison against values for these measurements that are representative of the ventricular myocyte phenotype. We demonstrated this procedure using commercially-available, mass-produced murine ES- and iPS- derived myocytes compared against a neonatal mouse ventricular myocyte target phenotype in coupled *in vitro* assays.

3.1 Introduction

In response to widespread efforts to commercialize differentiated stem cells, [173] the U.S. Food and Drug Administration (FDA) established a set of regulations and guidelines for manufacturing and quality control evaluation of human cellular and tissue-based products derived from stem cells [174]. The recommendations outlined for evaluating differentiated stem cell phenotype were developed specifically to address patient safety concerns, such as tumorigenicity and immunologic incompatibility due to

the initial focus of the industry on regenerative medicine applications [175]. Concerns over patient safety may have slowed the commercialization of regenerative therapies [176], but the use of industrial stem cell-based products for *in vitro* research, particularly pharmaceutical screening applications [177-180] is a promising goal that can potentially be reached in the near term. Due to the mandate to test all drug compounds for potential adverse effects on the heart, *in vitro* cardiac toxicity screening is a particularly important application that has prompted the development of commercial stem cell-derived cardiac myocytes by a number of companies [181]. In this context, the focus of quality assurance shifts from patient safety concerns to the development and adoption of measures that ensure these cells reliably mimic cardiac myocytes found *in vivo*.

In order to develop quality assurance standards for assessing stem cell-derived myocyte differentiation, it is necessary to first establish the set of characteristics that reliably define cardiac myocyte identity. We reasoned that the most effective way to delineate these standards was to comprehensively evaluate the aspects of form and function that give rise to the contractile properties of cardiac myocytes in the healthy, post-natal heart [143]. No standardized approach currently exists for evaluating cardiac differentiation. Basic characterization involves the use of one or more assays with stringencies ranging from the observation of spontaneous beating activity to electrophysiological recordings, wherein the use of gene expression profiling is one of the most common [182]. In addition to measuring the expression of cardiac biomarker genes, [183, 184] we also examined the organizational characteristics of the contractile myofibrils [160], the electrical activity that regulates myofibril contraction [185], and contractile force output directly [161]. Since human ventricular myocytes are not readily

available, we utilized commercially-available murine ES- (mESC) and iPS- (miPSC) derived myocytes and compared them against ventricular myocytes freshly isolated from neonatal mice (neonate). Though the cardiac physiology of humans and mice differ, the goal was to determine the utility of comparing industrially manufactured stem cell-derived myocytes and isolated cardiac myocytes possessing the desired phenotype using a multi-factorial comparison of high level myocardial tissue architectural and functional characteristics.

3.2 Results

3.2.1 Gene Expression Profiling of mES, miPS, and Neonate Engineered Tissues

We previously reported the influence of tissue architecture on the contractile performance of engineered myocardium *in vitro*, so we began our characterization of the commercially-available mES and miPS myocytes by evaluating their response to geometric cues encoded in the ECM, [160] and measuring the expression of genes that are commonly used to delineate the cardiac myocyte lineage [186, 187]. Culturing the mES (Figure 3-1Ai) and miPS (Figure 3-1Aii) myocytes on a substrate coated uniformly with fibronectin (FN) gave rise to monolayers with an isotropic cellular arrangement similar to the arrangement observed when neonate ventricular myocytes (Figure 3-1Aiii) were cultured in a similar manner. Moreover, mES (Figure 3-2Ai), miPS (Figure 3-2Aii), and neonate (Figure 3-2Aiii)

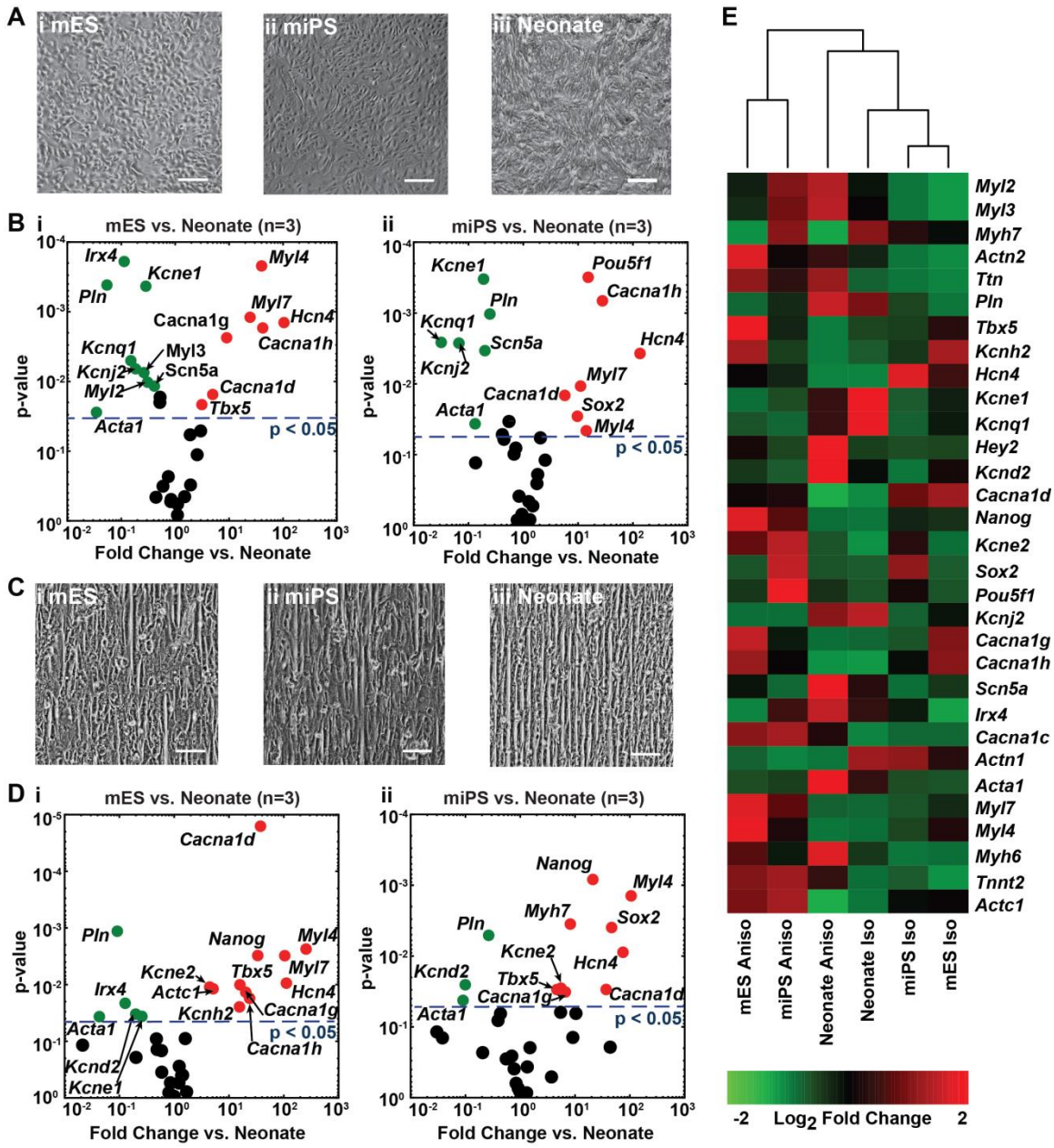

Figure 3-1: Comparison of mES, miPS, and neonate gene expression profiles on isotropic and anisotropic ECM substrates.

(A) Culturing (i) mES, (ii) miPS, and (iii) neonate myocytes on substrates with a uniform coating of FN resulted in isotropic cellular arrangement. (B) Volcano plots showing the negative log of p-values (two-tailed T-test, n = 3 for all conditions) versus log fold-change values for the comparison of qPCR measurements of cardiac genes

(Continued) between (i) mES and neonate isotropic monolayers, (Continued) and between (ii) miPS and neonate isotropic monolayers reveal significant differences for a number of genes (points on the plot colored green or red represent genes with $p < 0.05$) (C) Culturing (i) mES, (ii) miPS, and (iii) neonate myocytes on substrates with micro-contact printed lines of FN that were 20 μm wide and spaced 4 μm apart resulted in anisotropic cellular arrangement in all three cell types. (D) Volcano plots showing the negative log of p-values (two-tailed T-test, n = 3 for all conditions) versus log fold-change values for the comparison of qPCR measurements of cardiac genes between (i) mES and neonate anisotropic monolayers, and between (ii) miPS and neonate anisotropic monolayers reveal slightly fewer genes demonstrating significant differences than in the isotropic cultures (points on the plot colored green or red represent genes with $p < 0.05$) (E) Hierarchical clustering of mean $2^{-\Delta Ct}$ values for a select panel of cardiac genes revealed that the isotropic and anisotropic neonate tissue expression profiles clustered together in the center columns of the heatmap, while the anisotropic mES and miPS expression profiles formed a separate cluster on the right sides of the heatmap, and the isotropic mES and miPS profiles clustered together on the left side of the heat map . Scale bars = 100 μm.

myocytes all assumed a pleomorphic morphology when cultured sparsely on isotropic FN (Figure 3-2B), even though the neonate cardiac myocytes displayed a smaller surface area than the mES and miPS myocytes (Figure 3-2C). Comparison of the expression profiles for isotropic mES (Figure 3-1Bi) and miPS (Figure 3-1Bii) derived tissues versus the neonate tissues revealed a number of significant differences associated

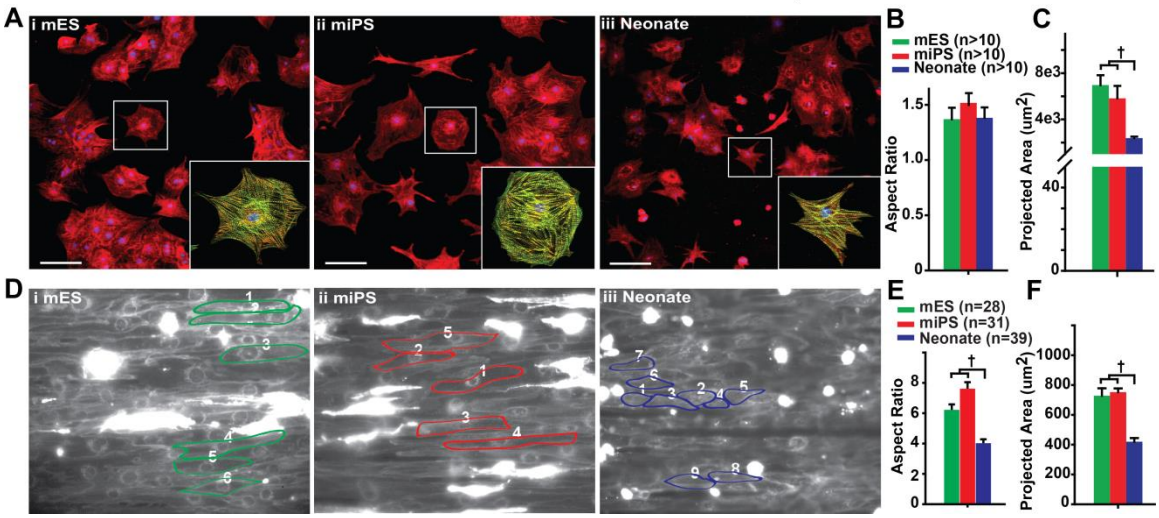

Figure 3-2: Evaluation of cardiac myocyte morphology on isotropic and anisotropic ECM substrates.

(A) Isotropic cultures of (i) mES, (ii) miPS, and (iii) neonate cardiac myocytes were fixed and immunostained for the presence of sarcomeric α-actinin (red), F-actin (green), and chromatin (blue). Cardiac myocytes were identified by the presence of sarcomeric α-actinin positive z-lines, and the boundaries of fully spread, mono-nucleated myocytes were manually traced using the polygon tool in ImageJ. The total number of pixels contained within each traced polygon was used to calculate (B) cellular aspect ratio, and (C) the total spread surface area for each cell type. (D) Similarly, the voltage sensitive dye RH237 used for optical mapping experiments allowed identification of myocyte boundaries in anisotropic monolayers of (i) mES, (ii) miPS, and (iii) neonate cardiac myocytes. The total number of pixels contained in each manually traced outline was used to calculate (E) aspect ratio, and (F) total spread surface area for each type of myocyte. All results presented as mean ± standard error of the mean. Statistical tests used was ANOVA on ranks († = $p < 0.05$). Scale bars = 20 μm.

with ion channel subunits and components of the sarcomere. In particular, the mES tissues exhibited significantly higher expression of the L-type Ca^{2+} channel subunit *Cacna1d* (4.9 fold, $p<0.05$), as well as the T-type subunits *Cacna1g* (9.0 fold, $p<0.05$) and *Cacna1h* (42.2 fold, $p<0.05$) versus neonate tissues. Isotropic mES tissues also showed significantly lower expression of *Irx4* (-9.1 fold, $p<0.001$), *Myl2* (-3.2 fold, $p<0.05$), and *Myl3* (-3.8 fold, $p<0.01$) commonly associated with the ventricular myocyte phenotype [183], and significantly higher expression of the atrial marker genes *Myl4* (40.2 fold, $p<0.001$), and *Myl7* (24.5 fold, $p<0.01$) than the neonate isotropic tissues. In contrast, the miPS isotropic tissues showed significant differences in expression for *Cacna1d* (5.7 fold, $p<0.05$), *Cacna1h* (27.9 fold, $p<0.001$), *Myl4* (14.1 fold, $p<0.05$) and *Myl7* (11.1, $p<0.05$) versus the neonate isotropic tissues. These observations suggest that the miPS-derived myocytes exhibited an expression profile that more closely resembled the profile of the neonate ventricular myocytes than the mES-derived myocytes.

Based on previous studies, we recognized that the gene expression profile of cardiac myocytes changed as a function of the tissue architecture within which they are embedded [188]. We engineered laminar, anisotropic myocardium from mES (Figure 3-1Ci), miPS (Figure 3-1Cii), and neonate cardiac myocytes by culturing them on micro-contact printed FN, where the cells spontaneously formed cell-cell junctions and aligned with the geometric cues within the matrix to form a contiguous tissue of high aspect ratio cells (Figure 3-2D, E). After several days in culture, we measured and compared the expression profiles of these engineered tissues. Comparison of the expression profiles for anisotropic neonate and mES tissues (Figure 3-1Di) revealed a number of differences associated with Ca^{2+} channel subunits, such as the L-type Ca^{2+} channel subunit *Cacna1d*

(37.5 fold, $p<0.0001$), as well as the T-type subunits *Cacna1g* (20.2 fold, $p<0.05$), and *Cacna1h* (23.8 fold, $p<0.05$). Additionally, the mES anisotropic tissues showed significantly lower expression of the ventricular marker *Irx4* (-7.7 fold, $p<0.05$), and significantly higher expression of the atrial markers *Myl4* (254.8 fold, $p<0.01$), and *Myl7* (104.0 fold, $p<0.01$) versus the neonate tissues.

In contrast, the miPS anisotropic tissues exhibited significant differences from the neonate tissues (Fig. 1Dii) for the Ca^{2+} channel subunits *Cacna1d* (36.9 fold, $p<0.05$) and *Cacna1g* (6.6 fold, $p<0.05$), as well as the atrial myosin light chain kinase gene *Myl4* (105.5 fold, $p<0.01$). Hierarchical clustering of neonate, mES, and miPS gene expression measurements revealed a distinct separation of the expression profiles for isotropic and anisotropic tissues, regardless of myocyte type (Figure 3-1E). Moreover, the expression profiles for mES and miPS myocytes in both the isotropic and anisotropic cellular configurations clustered closer to each other than to the neonate tissues. This suggests that the mES and miPS myocytes exhibited global transcriptional profiles that were unique from the neonate expression pattern, despite differences in the relative expression profiles between the mES and miPS tissues.

3.2.2 Characterization of Myofibril Architecture and Global Sarcomere Alignment

One of the defining features of the ventricular myocardium is the laminar arrangement of cardiac myocytes that serves to organize and orient the contractile sarcomeres to facilitate efficient pump function [14]. We evaluated the ability of mES and miPS engineered tissues to self-assemble myofibrils with alignment comparable to

neonate ventricular myocytes using custom image analysis software developed in our lab (Figure 3-3A). Immunofluorescence micrographs of sarcomeric α-actinin allowed us to visualize the orientations of the z-lines outlining the lateral edges of sarcomeres and

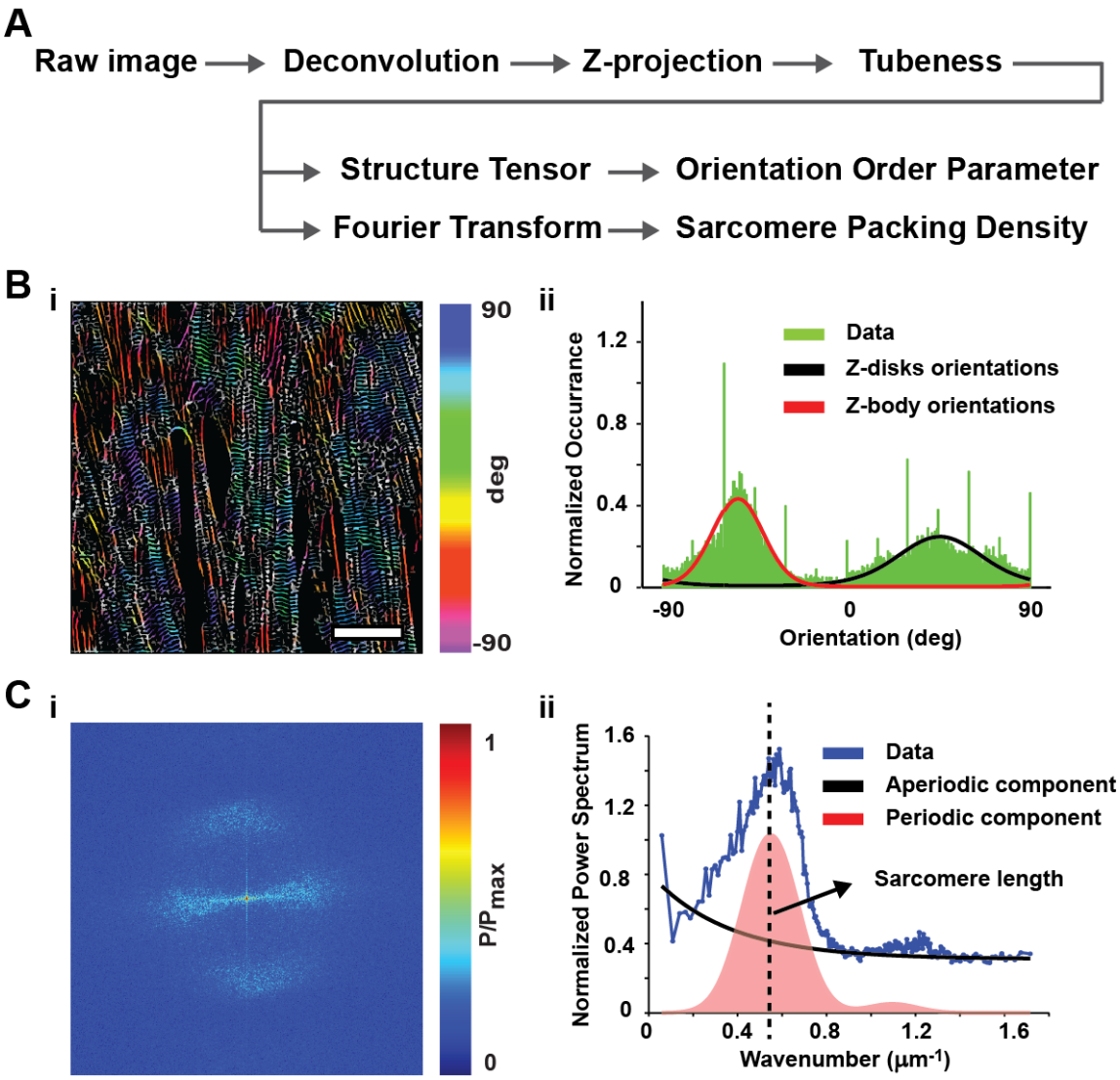

Figure 3-3: Image analysis procedure for sarcomere organization and structural characterization.

(A) Image processing flow: sarcomeric a-actinin immunographs were deconvolved, projected onto a single 2D image and then processed with a tubeness operator before further processing. (B) The orientations of sarcomeric a-actinin positive pixels were

(Continued) detected with a structure tensor method, color coded using the hsv digital image representation (i) and finally displayed into a histogram (ii) of the normalized occurrences of each orientation (C) The sarcomere length and the overall regularity of the cytoskeletal structure were detected processing the immunograph 2D Fast Fourier Transform algorithm. The detected power spectrum (i), for representation purpose a gamma correction of 0.1 was applied) was then integrated and normalized by the total energy. (ii) The sarcomere packing density was defined as the area under the signal peaks (red curve) whose location related with the sarcomere length.

quantitatively assess sarcomere organization in our engineered tissues (Figure 3-3Bi-ii). Visualization of global z-line registration in isotropic monolayers of mES (Figure 3-4Ai), miPS (Figure 3-4Aii), and neonate (Figure 3-4Aiii) myocytes revealed random orientation patterns. In contrast, the anisotropic mES (Figure 3-4Bi), miPS (Figure 3-4Bii), and neonate (Figure 3-4Biii) tissues demonstrated a greater degree of uniaxial z-line registration. To quantify the differences in global sarcomere organization between the mES, and miPS tissues, versus the neonate tissues (Figure 3-4C), we utilized a metric known as the orientational order parameter (OOP) that is commonly used to characterize the alignment of liquid crystals [189], and ranges from zero (random organization) to one (perfect alignment). It has been shown previously that this metric can be successfully adapted to measure and compare z-line registration in engineered cardiac tissues, and that it provides insight into the contractile strength of the tissues [160]. The anisotropic neonate tissues exhibited a significantly higher OOP value than both the mES and miPS tissues, suggesting that both types of stem cell-derived cardiac myocytes were unable to

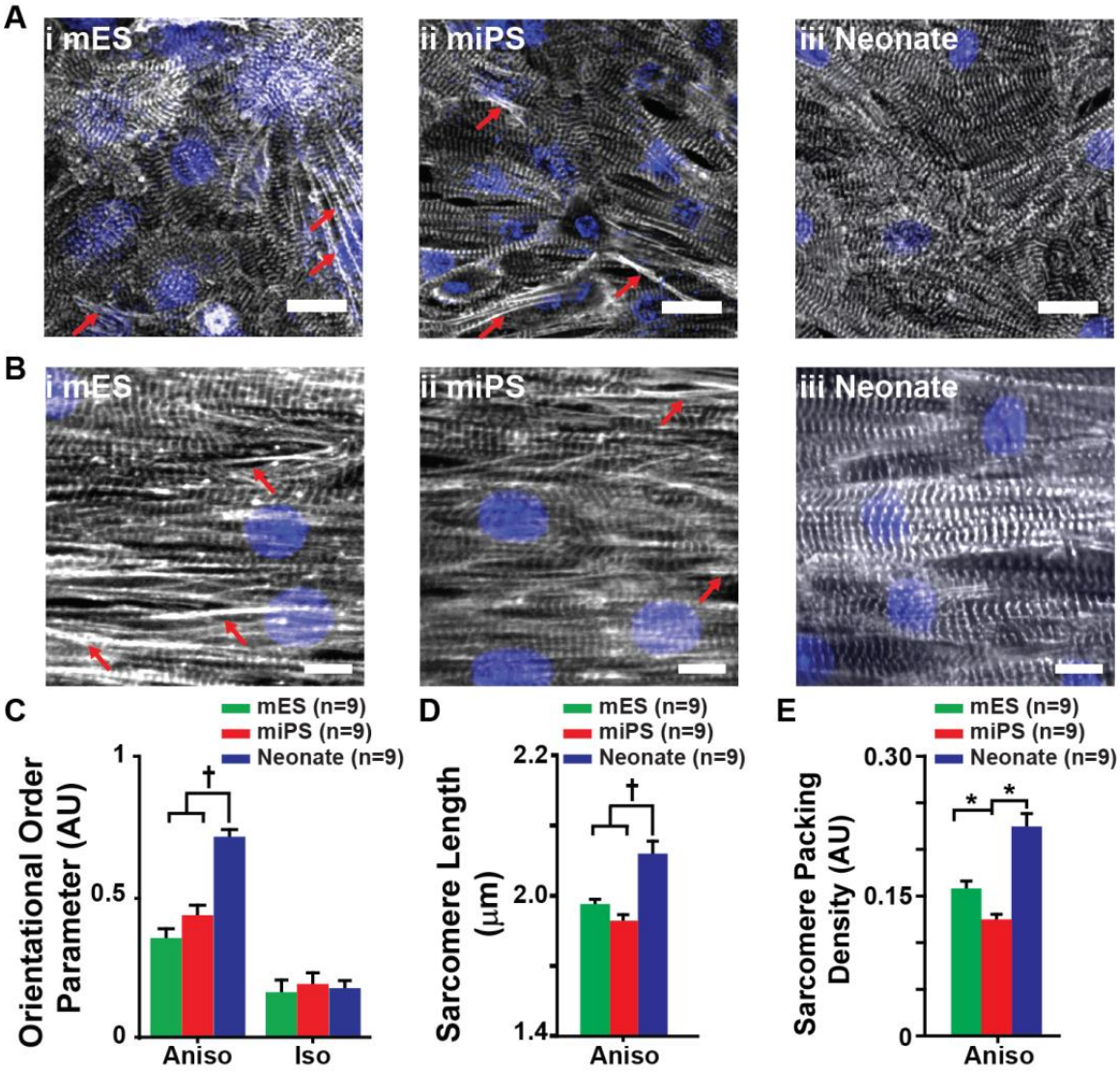

Figure 3-4: Comparison of myofibril architecture in mES, miPS, and neonate engineered tissues.

Immunofluorescence visualization of sarcomeric α-actinin in (A) isotropic monolayers of (i) mES, (ii) miPS, and (iii) neonate myocytes and (B) anisotropic monolayers of (i) mES, (ii) miPS, and (iii) neonate myocytes revealed the pattern of sarcomere organization adopted by each cell type in response to geometric cues encoded in the ECM. Immature pre-myofibrils (red arrows) were observed exclusively in mES and miPS engineered tissues. Quantitative evaluation of sarcomeric α-actinin immunofluorescence micrographs

(Continued) allowed statistical comparison of sarcomere organization and architecture. (C) Orientational order parameter (OOP) was used as a metric of global sarcomere alignment within the engineered tissues and showed that anisotropic neonate tissues exhibited significantly greater overall sarcomere alignment than the mES and miPS anisotropic tissues. No significant differences in global sarcomere alignment were observed between the isotropic mES, miPS, and neonate tissues. (D) Comparison of z-line spacing revealed that the neonate anisotropic tissues exhibited significantly greater sarcomere length than both the mES and miPS anisotropic tissues. (E) From the measurements of sarcomere length, sarcomere packing density was calculated for anisotropic tissues of each cell type. All three cell types exhibited significantly different sarcomere packing densities from one another. Statistical tests used were either ANOVA (* = $p < 0.05$), or ANOVA on ranks († = $p < 0.05$). Data are presented as mean ± SEM. Scale bars = 10 μm.

generate myofibrils with the same degree of global sarcomere alignment as the neonate myocytes. Isotropic tissues had low OOP values, due to the random organization of the cardiac myocytes. Measurement of registered z-line spacing also revealed that the anisotropic mES and miPS tissues displayed significantly shorter sarcomere lengths than the neonate tissues (Figure3-4D). Moreover, quantification of "sarcomere packing density," *i.e.* the proportion of α-actinin localized to z-lines indicative of the presence of fully-formed sarcomeres, showed that the anisotropic neonate tissues exhibited significantly higher sarcomere packing density than the mES and miPS tissues. Taken together, these analyses revealed that the mES- and miPS-derived myocytes responded to

ECM cues in a similar manner to the neonate myocytes, but exhibited sarcomere organization reminiscent of immature pre-myofibrils observed in embryonic cardiac myocytes [138, 190, 191].

3.2.3 Measurement of mES, miPS, and Neonate Electrophysiological Performance

The electrical activity of cardiac myocytes regulates the initiation of myofibril contraction and is commonly measured as an indicator of myocyte identity and functionality [185, 187, 192]. We used planar patch clamp recordings to compare and contrast the action potential characteristics of isolated mES, miPS, and neonate myocytes. We identified two different demographics of cell types as demonstrated by action potential (AP) morphology [187]. Neonate myocytes primarily demonstrated ventricular-like APs (Figure 3-5Ai), whereas, mES- and miPS-derived myocytes exhibited APs that were evenly distributed between the ventricular-like and atrial-like (Figure 3-5Aii) morphologies. Both the mES- and miPS-derived myocytes primarily exhibited APs as shown in Figure 3-5Aii, whereas the neonate ventricular myocytes demonstrated APs illustrated in Figure 3-5Ai. Analysis of AP characteristics, such as maximum voltage (Vmax), action potential duration at 50% repolarization (APD50), and action potential duration at 90% repolarization (APD90), revealed that the mES and miPS myocytes exhibited roughly equal incidences of atrial-like and ventricular-like APs, whereas the neonate cardiac myocytes displayed ventricular-like AP characteristics (Figure 3-5B). In addition to AP characterization, we also measured the electrical conduction properties of the anisotropic mES (Figure 3-5Ci), miPS (Figure 3-5Cii), and neonate (Figure 3-5Ciii) tissues using optical mapping and the voltage-sensitive fluorescent dye RH-237 [100, 192,

193] to evaluate the ability of the stem cell-derived myocytes to form the electromechanical syncytium that typifies the myocardium [185]. We did not observe any significant differences in the longitudinal (LCV) or transverse (TCV) conduction velocities between the mES, miPS, and neonate tissues (Figure 3-5D). However, we did observe substantial differences in the cellular dimensions (*l* x *w*) of mES (72.04 μm x 12.07 μm) and miPS (82.30 μm x 11.25 μm) versus neonate (44.93 μm x 11.35 μm) cardiac myocytes that may influence the magnitude of the LCV and TCV in engineered tissues comprised of these cells, making them appear faster than they actually are. AP duration measurements revealed no significant differences at 50% repolarization (APD50), but a significant ($p<0.05$) difference was observed at 90% repolarization (APD90) between the neonate and mES anisotropic tissues (Figure 3-5E).

Ca^{2+} plays a crucial role in coupling myocyte excitation and contractile activity [194]. We measured Ca^{2+} transient activity in engineered anisotropic tissues, as well as the Ca^{2+} current profiles of isolated mES, miPS, and neonate myocytes. Ca^{2+} transients measured in anisotropic tissues revealed a significantly ($p<0.05$) shorter 50% decay time in the miPS, but not the mES tissues, as compared to the neonate, and significantly ($p<0.05$) shorter 90% decay time in both the mES and miPS tissues versus the neonate tissues (Figure 3-5F). Planar patch clamp recordings of L- (Figure 3-5Gi) and T- (Figure 3-5Gii) type Ca^{2+} current profiles revealed significantly ($p<0.05$) higher total (TOT) and T-type (TCC) maximum Ca^{2+} current densities in the neonate myocytes versus the mES-derived, but not the miPS-derived myocytes (Figure 3-5H). Taken together, these data suggest that the mES and miPS myocytes possessed electrophysiological properties

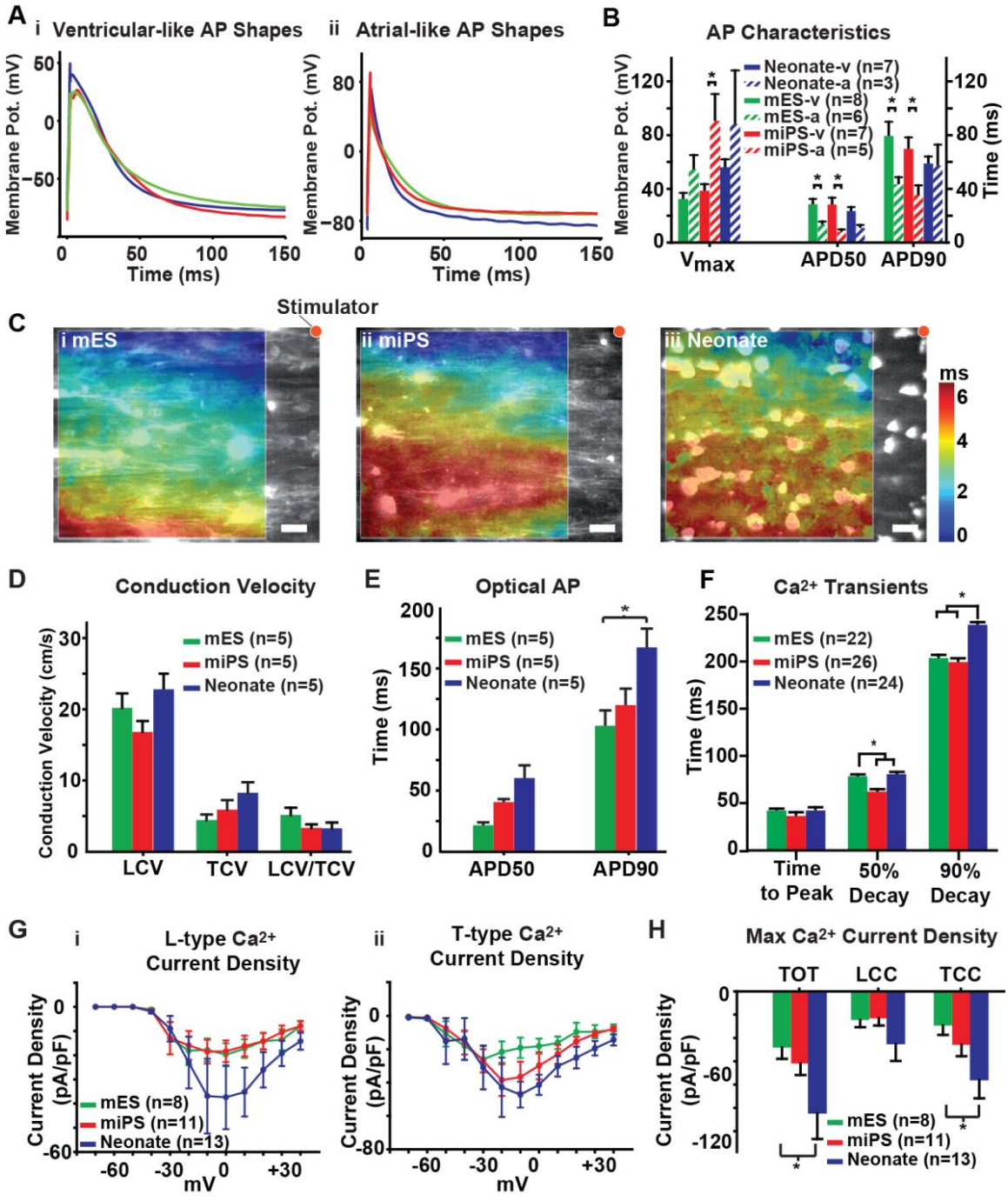

Figure 3-5: Comparison of electrical activity in mES, miPS, and neonate engineered tissues.

(A) Patch clamp recordings taken on isolated mES, miPS, and neonate myocytes exhibited action potentials (AP) with both (i) ventricular-like, and (ii) atrial-like profiles.

(Continued) (B) Characterization of the AP traces revealed no significant differences between the three cell types, but the mES and miPS myocytes exhibited an equal proportion of ventricular-like (mES-v, miPS-v) and atrial-like (mES-a, miPS-a) AP traces, whereas the neonates exhibited primarily ventricular-like (neonate-v) AP profiles. (C) The electrophysiological characteristics of anisotropic (i) mES, (ii) miPS, and (iii) neonate tissues were assessed using optical mapping and the photovoltaic dye RH237. (D) Comparison of conduction properties between the mES, miPS, and neonate tissues revealed no significant differences in either longitudinal (LCV) or transverse (TCV) conduction velocity. (E) Evaluation of optical AP duration in anisotropic tissues revealed no significant differences in APD50, but a significant difference in APD90 between the mES and neonate tissues was observed. (F) Comparison of Ca2+ transients measured in anisotropic tissues revealed that the 50% decay time of the miPS tissues was significantly lower than the both the mES and neonate tissues, but the 90% decay time of both the mES and miPS tissues was significantly lower than the neonate tissues. (G) Patch clamp recordings were collected on isolated mES, miPS, and neonate myocytes to measure and compare (i) L-type, and (ii) T-type Ca2+ current densities elicited at various holding potentials. (H) Patch clamp recordings of maximum Ca2+ current density in isolated mES, miPS, and neonate myocytes revealed a significant difference in total Ca2+ current density (TOT) between the neonate and mES myocytes. No significant differences in L-type Ca2+ current density (LCC) were observed, but a significant difference in T-type Ca2+ current density (TCC) was observed between the neonate and mES myocytes. Statistical test used was ANOVA (* = $p < 0.05$). Data are presented as mean ± SEM. Scale bars = 20 μm.

similar to neonate cardiac myocytes, aside from differences in funny current and voltage-gated Ca^{2+} channel subunit expression, illustrated in Figure 3-1.

3.2.4 Measurement of mES, miPS, and Neonate Engineered Tissue Contractile Performance

With the muscular thin film (MTF) contractility assay, it is now possible to assess the diastolic (Figure 3-6Ai) and systolic (Figure 3-6Aii) function of engineered myocardium directly [149, 161, 170]. Using the "heart-on-a-chip" MTF assay [170], we measured the stress generation profiles of the anisotropic mES, miPS, and neonate tissues (Figure 3-6B), and compared their contractile performance. The anisotropic neonate tissues generated significantly ($p<0.05$) higher diastolic, peak systolic, and twitch stress than both the mES and miPS tissues (Figure 3-6C), with observed values for the neonate tissues within the range measured for isolated murine papillary muscle strips [195, 196]. The results of the contractility measurements clearly show a functional deficit in the mES- and miPS-derived myocytes that was not apparent in the electrophysiological measurements. The combined output of our electrophysiological, calcium transient and contractile force experimental measurements were used to create graphical representations of the excitation-contraction coupling profiles of the mES (Figure 3-6Di), miPS (Figure 3-6Dii), and neonate (Figure 3-6Diii) engineered tissues that clearly illustrate the similarities and differences in the excitation-contraction coupling amongst the cell types. These data illustrate that the miPS-derived myocytes are qualitatively more similar to the neonate myocytes than the mES-derived myocytes.

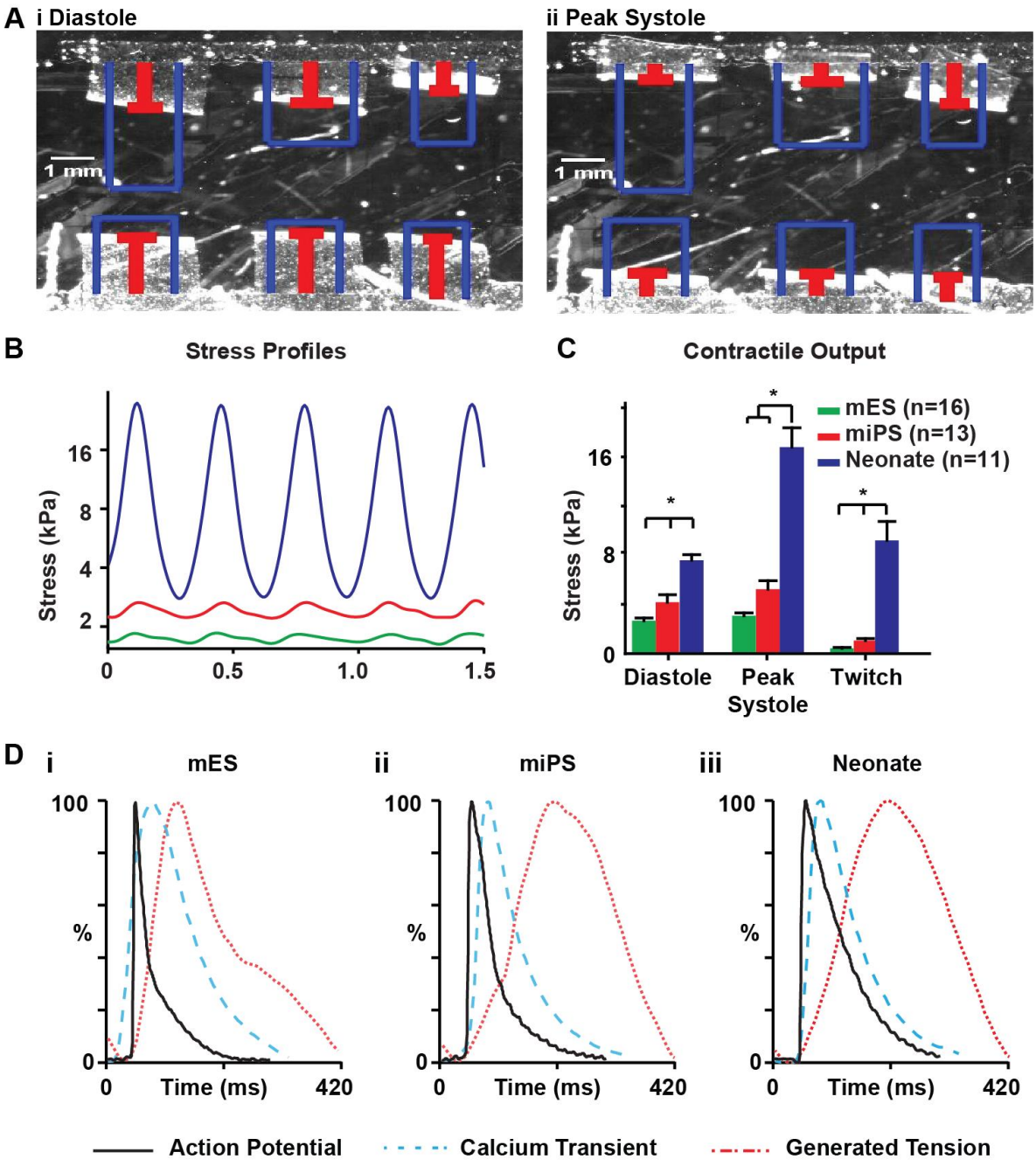

Figure 3-6: Comparison of contractile performance in mES, miPS, and neonate engineered tissues.

(A) Contractile performance of anisotropic mES, miPS, and neonate tissues was assessed using the muscular thin film (MTF) assay wherein the radius of curvature of the MTFs at (i) diastole and (ii) peak systole were used to calculate contractile stress. (B) The radius

(Continued) of curvature of the MTFs was used to calculate and compare the temporal contractile strength profiles of anisotropic mES (green), miPS (red), and neonate (blue) tissues. (C) Comparison of MTF contractile output revealed that neonate anisotropic tissues generated significantly greater diastolic, peak systolic, and twitch stress than both the mES and miPS tissues. (D) Graphical representation of action potential morphology (black solid line), Ca2+ transient morphology (blue dotted line), and contractility profile (red dotted line) during a typical excitation-contraction cycle of the mES, miPS, and neonate engineered anisotropic tissues. Statistical test used was ANOVA (* = $p < 0.05$). Data are presented as mean ± SEM.

3.2.5 Integration of Experimental Measurements to Evaluate Stem Cell-Derived Myocyte Cardiac Phenotype

To determine how closely the mES- and miPS-derived myocytes matched the phenotype of the neonate ventricular myocytes, we computationally-integrated the set of gene expression, morphology, electrophysiology, and contractility experimental measurements collected on each cell population, and calculate the difference between the unknown and target cell populations. This was achieved by evaluating measures of effect size, such as z-factor and Strictly Standardized Mean Difference (SSMD), that have been previously used to quantify biological population differences in high throughput screening applications [197]. We chose to use SSMD instead of z-factor in this case study because the SSMD is more robust to outliers, is not dependent on sample size, and can be used to evaluate non-normal data [198]. For each type of experimental measurement, we normalized the mean (μ_{norm}) values to the interval [0,1] by identifying

the maximum (μ_{max}) and minimum (μ_{min}) mean values observed for that measurement from all three cardiac myocyte sources, and calculating:

$$\mu_{norm} = \frac{\mu - \mu_{max}}{u_{max} - \mu_{min}} \quad (1)$$

Using these normalized values, the SSMD (β) quantifying the differences between each unknown population (*i.e.* mES, miPS) and the neonate target population was calculated as follows:

$$\beta = \frac{\mu_{target} - \mu_{unknown}}{\sqrt{\sigma^2_{target} + \sigma^2_{unknown}}} \quad (2)$$

where μ represents mean and σ represents standard deviation, to evaluate the magnitude of difference, taking into account the variance in the measurements, between the stem cell-derived myocytes and the neonate cardiac myocytes (Figure 3-7). This allowed us to identify the parameters that show the greatest degree of similarity and difference from the target neonate ventricular myocyte tissues. We then used the β values from each experimental measurement for the mES and miPS tissues and calculated the mean squared error (MSE) versus the neonate tissues as follows:

$$MSE = \frac{\mathbf{1}}{n}\sum_{i=1}^{n}\beta_i^2 \quad (3)$$

where n is the total number of experimental measurement β values included in the calculation, to evaluate the differences observed for each measurement category (i.e. the β values for gene expression, morphology, electrical activity, contractility used to calculate category-specific MSE values), as well as define a single MSE value calculated from all of the experimental measurements from all categories combined, that represents the total difference between the stem cell-derived and neonate cardiac myocytes based on

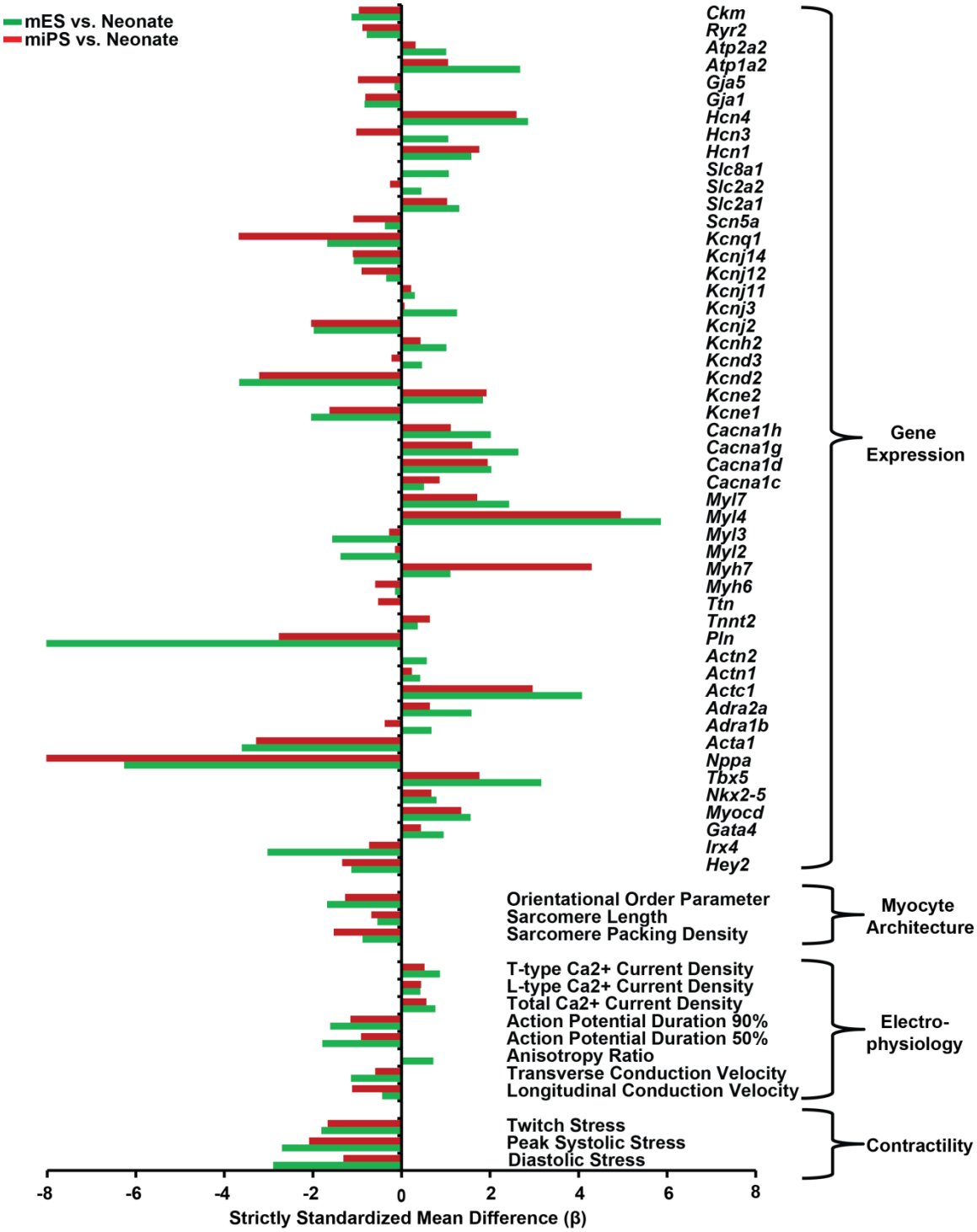

Figure 3-7: Integrated visual comparison of mES, miPS, and neonate experimental measurements.

(Continued) Strictly Standardized Mean Difference (β) values were computed for mES- and miPS-derived myocytes relative to the neonate cardiac myocytes from the mean and sample standard deviations collected for each experimental measurement. These β values were organized by measurement type (i.e. gene expression, myocyte architecture, electrophysiology, contractility) and plotted to allow comparison. Negative β values indicate measurements with higher relative magnitude in the neonate cardiac myocytes, whereas positive β values indicate measurements that were higher in the mES/miPS myocytes relative to the neonate cardiac myocytes based on the measurements performed (Table 3-1). A lower MSE values indicates a better match to the neonate target phenotype, with an MSE value of zero indicating a perfect match.

Table 3-1: Mean squared error values calculated for each group of measurements in the comparison of the mES- and miPS-derived myocytes to the neonate ventricular myocytes. The strictly standardized mean difference (β) values computed for each experimental measurement were used to calculate mean squared error (MSE) values for each of the major measurement categories, as well as all of the measurements combined, in the comparisons of the mES (MSE_{mES}), and miPS (MSE_{miPS}) engineered tissues to the neonate engineered tissues.

Measurement Category	MSE_{mES}	MSE_{miPS}
Gene Expression	5.69	4.25
Morphology	1.30	1.48
Electrophysiology	1.16	0.57
Contractility	6.32	2.95
All Measurements	4.95	3.60

We found that the miPS tissues exhibited lower MSE values than the mES tissues for every measurement category, except morphology. In addition, the overall MSE values calculated from all of the experimental measurements combined revealed a lower MSE for the miPS engineered tissues than those comprised of mES-derived myocytes. This suggests that the miPS-derived myocytes exhibited a global phenotype that was slightly closer to the neonate cardiac myocytes than the mES-derived myocytes, although both the mES- and miPS-derived myocytes demonstrated substantial differences from the neonate cardiac myocytes for a number of characteristics.

3.3 Discussion

The goal of this study was to define a quality control standard rubric for assessing stem cell-derived cardiac myocytes. We chose a set of experimental measurements that provide insight, not only into the expression profile of the cells, but also into morphological and functional characteristics that are intimately tied to the contractile function of cardiac tissues [100, 160, 185]. We utilized ventricular myocytes isolated from post-natal mouse hearts to serve as our reference standard for defining the target phenotype, although an inherent limitation to using these cells is the presence of non-cardiomyocytes, such as fibroblasts, endothelial cells, and smooth muscle cells that may confound the interpretation of some experimental measurements, such as gene expression profiling. It should also be noted that the mES- and miPS-derived cardiac myocytes used in this study were produced using a differentiation protocol that gives rise to a heterogeneous population of atrial, ventricular, and pacemaker-like cells that may also make interpretation of certain measurements challenging. However, the quality

assessment strategy proposed is not dependent on any particular set of measurements, and allows researchers the flexibility to choose the set of experimental measurements that best suits their needs.

Using the experimental measurements described above and isolated neonatal ventricular myocytes as our reference phenotype, we developed a "quality index" that utilizes the magnitude and variance of these measurements to provide a numeric score of how closely the stem cell-derived myocytes match the characteristics of the neonatal cardiac myocytes. The combination of gene expression, morphological evaluation, electrophysiological, and contractility measurements employed allowed us to pin-point specific differences in the structural and functional properties of the mES and miPS engineered tissues versus the neonate tissues that have important implications for their utility in *in vitro* assays. Additional studies of the relationships between these measurements and the response of engineered cardiac tissues to compounds that have known effects on heart function may provide valuable insight into the combination of measurements that offer the most reliable insight into the ability of stem cell-derived cardiac myocytes to adopt the desired phenotype. With a carefully chosen set of experimental parameters, this quality assessment rubric may provide a reliable means to evaluate strategies employed to improve the differentiation of cardiac myocytes from stem cells and drive them towards a more mature phenotype [199]. Further, this "quality index" would not only allow researchers to identify the commercial stem cell-derived myocyte product lines that are most suitable for their needs, it may also serve the stem cell industry as a quality assurance system for ensuring that batches released to customers faithfully recapitulate the desired phenotype.

3.4 Materials and Methods

3.4.1 Cardiac Myocyte Cell Culture

3.4.1.1 Murine Stem Cell-Derived Cardiac Myocyte Culture

Cor.At murine ES- (Lot# CS25CL_V_SN_1M, production date: 2010-02-16) and iPS-derived (Lot# CS02CL-i, production date: 2010-11-15; CS07CL-i, production date: 2011-05-09) myocytes were cultured according to instructions, and with culture reagents supplied by the manufacturer (Axiogenesis, Cologne, Germany). Briefly, cells were cultured in T25 flasks pre-coated with 0.01 µg/mL fibronectin (FN) (BD Biosciences, Bedford, MA) in puromycin-containing culture media at 37ºC and 5% CO_2 for 72 hours to eliminate un-differentiated stem cells from the culture. After 72 hours, cells were dissociated with 0.25% trypsin and seeded onto micro-contact printed substrates at densities of 100,000/cm^2. Cells were cultured for 2 days on micro-contact printed substrates to allow formation of a functional syncytium, while preserving the proportion of myocytes exhibiting ventricular characteristics prior to experimentation.

3.4.1.2 Neonatal Mouse Ventricular Myocyte Isolation and Culture

Neonatal mouse ventricular myocytes were isolated from 2-day old neonatal Balb/c mice using procedures approved by the Harvard University Animal Care and Use Committee. Briefly, excised ventricular tissue was incubated in a 0.1% (w/v) trypsin (USB Corp., Cleveland, OH) solution cooled to 4°C for approximately 12 hours with agitation. Trypsinized ventricular tissue was dissociated into cellular constituents via serial exposure to a 0.1% (w/v) solution of collagenase type II (Worthington Biochemical,

Lakewood, NJ) at 37º C for 2 minutes. Isolated myocytes were maintained in a culture medium consisting of Medium 199 (Invitrogen, Carlsbad, CA) supplemented with 10% (v/v) heat-inactivated fetal bovine serum (FBS), 10 mM HEPES, 20 mM glucose, 2 mM L-glutamine, 1.5 µM vitamin B-12, and 50 U/ml penicillin and seeded at a density of 200,000 cells/cm^2. From the second day of culture onward, the FBS concentration was reduced to 2% (v/v), and medium was exchanged every 48 hours. Myocytes were cultured for 4 days on micro-contact printed substrates prior to experimentation.

3.4.2 Fabrication of "Heart-on-a-Chip" Micro-Patterned ECM Substrates

3.4.2.1 Design and Fabrication of Micro-contact Printed ECM Substrates

Silicone stamps designed for micro-contact printing were prepared as previously described. Photolithographic masks were designed in AutoCAD (Autodesk Inc., San Rafael, CA), and consisted of 20 µm wide lines separated by 4 µm gaps to impose a laminar organization on the myocytes. Polydimethylsiloxane (PDMS, Sylgard 184, Dow Corning, Midland, MI) was used to fabricate stamps with the specified pattern. Stamps were incubated with 50 µg/mL FN (BD Biosciences, Bedford, MA) for one hour. Glass coverslips were spin-coated with PDMS and treated in a UV-ozone cleaner (Jelight Company, Inc., Irvine, CA) immediately prior to stamping with FN. After transfer of the FN pattern to the surface of the PDMS-coated coverslips, they were incubated in 1% (w/v) Pluronic F-127 (BASF, Ludwigshafen, Germany) to block cell adhesion to un-stamped regions.

3.4.2.2 Muscular Thin Film Fabrication

Engineered cardiac tissue contractile performance was measured using a custom muscular thin film based platform [149, 161, 170]. Briefly, the "heart-on-a-chip" substrates consisted of glass coverslips selectively coated with a thermo-sensitive sacrificial polymer, Poly (N-isopropylacrylamide) (PiPAAm, Polysciences, Inc., Warrington, PA), and with a second layer of PDMS. The thickness of the PDMS layer was found to be in the range of 10-18 μm for all "heart chips" used in this study (Dektak 6M, Veeco Instruments Inc., Plainview, NY).

3.4.3 Muscular Thin Film Contractility Measurements

During contractility experiments, samples were submerged in Tyrode's solution (mM, 5.0 HEPES, 5.0 glucose, 1.8 $CaCl_2$, 1.0 $MgCl_2$, 5.4 KCl, 135.0 NaCl, and 0.33 NaH_2PO_4, pH 7.4). All reagents were purchased from Sigma Aldrich (St. Louis, MO). Rectangular films were cut with a razor blade, and the bath temperature was decreased below the PiPAAm transition temperature, making possible for the MTF to bend away from the glass. Video recording of the deformation of each film were processed to obtain the time-course [161] of the tissue-generated stresses. The peak systolic and diastolic stresses were calculated as the average of the maxima and minima of the stress profile during 10 cycles at a pacing of 3 Hz, and twitch stress was defined as the difference between peak systolic and diastolic stresses.

3.4.4 Immunohistochemical Labeling

Samples were fixed in 4% (v/v) paraformaldehyde with 0.05% (v/v) Triton X-100 in PBS at room temperature for 10 minutes. Cells were incubated in a solution containing 1:200 dilutions of monoclonal anti-sarcomeric α-actinin antibody (A7811, clone EA-53, Sigma Aldrich, St. Louis, MO), polyclonal anti-fibronectin antibody (F3648, Sigma-Aldrich, St. Louis, MO), 4',6'-diamidino-2-phenylindole hydrochloride (DAPI, Invitrogen, Carlsbad, CA), and Alexa Fluor 633-conjugated phalloidin (Invitrogen, Carlsbad, CA) for one hour at room temperature. Samples were then incubated in 1:200 dilutions of Alexa Fluor 488-conjugated goat anti-mouse IgG and Alexa Fluor 546-conjugated goat anti-rabbit IgG secondary antibodies (Invitrogen, Carlsbad, CA) for 1 hour at room temperature. Labeled samples were imaged with a Zeiss LSM confocal microscope (Carl Zeiss Microscopy, Jena, Germany).

3.4.5 Quantitative Evaluation of Sarcomere Organization

Confocal Z-stacks of sarcomeric α-actinin fluorescence micrographs were de-convolved with Mediacy Autoquant (MediaCybernetics, Rockville, MD). Analysis of sarcomeric structural characteristics was conducted using custom-designed ImageJ [200] and MATLAB (Mathworks, Natick, MA) software (Figure 3-3A). The orientations of sarcomeric α-actinin positive pixels were determined using an adapted structure-tensor method [169] and the orientational order parameter (OOP), a measure of the global alignment of the sarcomeres, was calculated from the observed orientation values. The orientations observed in the micrographs were color-coded using the HSV digital image representation (Figure 3-3Bi) where the Hue channel was used for orientation, the

Saturation channel for pixel coherency (*i.e*. a measure of local contrast), and the Value channel for the pre-processed image. The normalized occurrence of orientations that demonstrated a coherency higher than a given threshold could then be displayed in a histogram (Figure 3-3Bii). The sarcomere length and the overall regularity of the z-lines were determined by processing the images with a 2D Fast Fourier Transform algorithm. The power spectrum (Figure 3-3Ci) was then radially integrated and normalized by the total area under the 1D curve. The sarcomere packing density was defined as the area under the periodic component (shaded red in Figure 3-3Cii).

3.4.6 Planar Patch Clamp Electrophysiological Recordings

Planar patch clamp experiments were conducted as previously described [192]. Briefly, cells were cultured on fibronectin (BD Biosciences, Bedford, MA) coated T25 flasks for 5 days, then isolated using .25% trypsin (Invitrogen, Carlsbad, CA), re-suspended in Extracellular Buffer Solution (EBS: mM, 140 NaCl, 4 KCl, 1 $MgCl_2$, 2 $CaCl_2$, 5 D-Glucose monohydrate, 10 HEPES, pH 7.4) to a final concentration of 1,000 cells/µL, and allowed to equilibrate for 5 minutes in EBS. The electronics were calibrated in the presence of EBS and Intracellular Buffer Solution (IBS: mM, 50 KCl, 10 NaCl, 60 KF, 20 EGTA, 10 HEPES, pH 7.2) prior to flowing cells into the chamber. 5 µL of cell suspension was then introduced into the chip and the negative pressure automatically adjusted to produce a final seal resistance greater than 1 GOhm. During current clamp experiments, cells were subjected to 10 trains of 10 current pulses at 3 Hz; the current amplitude was set to 1.5 times the threshold for AP generation. When the signal reached steady state, 10 APs were averaged yielding a representative trace for the calculation of

action potential duration indicators. During voltage clamp experiments cells were kept in buffers containing TTX (10 µM), Nifedipine (10 µM), 4-AP (1 mM) and TEA (20 mM) purchased from Sigma Aldrich (St. Louis, MO). The membrane potential subjected to 2 voltage clamp protocols, first the membrane potential was held to a value of -90 V for 250 ms and then stepped from -70 to +40 mV in 10 mV steps for 250 ms, thus eliciting the total Ca^{2+} current (TOT). Second, from the same holding potential, cells were stepped from -40 to +40 mV, a range in which mostly the L-type Ca^{2+} current (LCC) is active. The T-type component (TCC) was then calculated as the difference between TOT and LCC.

3.4.7 Optical Mapping of Tissue-Scale Electrophysiology

Samples were incubated in 4 µM RH237 (Invitrogen, Carlsbad, CA) for 5 minutes and washed 3 times with Tyrode's solution, prior to recording. Temperature of the bath solution was maintained at approximately 35º C using a digital temperature controller (TC-344B, Warner Instruments, Hamden, CT) for the duration of the experiment. 10 µM Blebbistatin (EMD Millipore, Billerica, MA) was added to minimize motion artifacts during recording of electrical activity [201, 202]. Samples were paced at 3 Hz with a 10 ms biphasic pulse at 10-15 V delivered using an SD-9 stimulator (Grass Technologies, Warwick, RI) and a bi-polar, platinum point electrode placed approximately 300 – 500 µm above the sample and 1 – 2 mm from the top right corner of the field of view (FOV). Imaging was performed using a Zeiss Axiovert 200 epifluorescence microscope (Carl Zeiss Microscopy, Jena, Germany) equipped with an X-cite Exacte mercury arc lamp (Lumen Dynamics, Mississauga, Ontario). Illumination light was passed through a

40X/1.3 NA objective (EC Plan-NEOFLUAR, Zeiss, Jena, Germany) and a band-pass excitation filter (530-585 nm). Emission light was filtered at 615 nm with a long-pass filter, and focused onto the 100 x 100 pixel chip of a high speed MiCAM Ultima CMOS camera (Scimedia, Costa Mesa, CA). Images were acquired at 1000 fps from 250 x 250 μm FOV. Post-processing of the raw data included reduction of drift induced by photobleaching by subtracting a linear fit of the baseline, applying a 3 x 3 pixel spatial filter to improve signal to noise ratio, and exclusion of saturated pixels. Activation time was calculated as the average maximum upstroke slope of multiple pulses over a 2 – 4 second recording window. Longitudinal and transverse conduction velocities (LCV and TCV) were calculated through a linear fit of the activation times along the horizontal and vertical axes of each FOV respectively. Optical action potential traces were calculated as the average of multiple pulses, while adjusting the offset of each pixel caused by different activation times.

3.4.8 Ratiometric Measurement of Ca^{2+} Transients in Engineered Tissues

Cardiac tissues were incubated in a 5 μM solution of acetoxymethyl (AM) Fura Red (Invitrogen, F-3021) reconstituted in Pluronic F-127 (Invitrogen, P-3000MP) for 20 minutes. After dye loading, cells were incubated in Tyrode's solution for 5 minutes, rinsed 3 times, and imaged on a Zeiss LSM LIVE (Carl Zeiss Microscopy, Jena, Germany) confocal microscope at 40x magnification with an environmental chamber to ensure a constant physiological temperature of 37° C. Tissues were field stimulated at 3 Hz during recordings. Dual excitation ratiometric recordings were performed by rapidly switching (through an acousto-optical tunable filter) excitation laser lights at 405 nm and

488 nm and collecting the corresponding emissions through a high-pass filter with cutoff at 546 nm. Recordings were constrained to 20 lines, oriented perpendicular to the main axis of the cells and ensuring minimal intersection with nuclei to maintain an acquisition speed of 250 fps. After background subtraction, two signals were obtained: one (blue line) that increases with the Ca^{2+} elevation corresponding to excitation at 405 nm, and one (green line) that shows an opposite trend and corresponded to the 488 nm excitation wavelength. The ratiometric representation of the Ca^{2+} transient was taken as the ratio of the 405 nm and 488 nm signals. Four consecutive transients at steady state were further averaged to create a representative single transient.

3.4.9 Real-Time PCR Gene Expression Measurement

Total RNA was collected in triplicate from both isotropic and micropatterned anisotropic samples using a Strategene Absolutely RNA Miniprep kit (Agilent Technologies, Santa Clara, CA) according to the manufacturer's instructions. Genomic DNA contamination was eliminated by incubating the RNA lysates in DNase I digestion buffer at 37ºC for 15 minutes during the RNA purification procedure. The quantity and purity of RNA lysates was assessed using a Nanodrop spectrophotometer (Thermo Scientific, Wilmington, DE). Purified total RNA lysates with OD 260/280 ratios greater than 1.7 were used for RT-qPCR measurements. Complementary DNA strands were synthesized for genes of interest using an RT2 first strand synthesis kit (Qiagen Inc, Valencia, CA) and custom pre-amplification primer sets (Qiagen Inc, Valencia, CA). 500 ng of total RNA were used from each lysate for each first strand synthesis reaction. Expression levels for specific genes of interest (Table S1) were measured using custom

RT2 Profiler RT-PCR arrays (Qiagen Inc, Valencia, CA) and a Bio-Rad CFX96 RT-PCR detection system (Hercules, CA). Statistical analysis of RT-qPCR threshold cycle data was carried out with the web-based RT2 Profiler PCR Array Data Analysis Suite version 3.5 (Qiagen Inc, Valencia, CA) according to published guidelines [167].

4 Conclusion

The vision of using human stem cells as a limitless source of cells for regenerative clinical applications, *in vitro* disease modeling, and pre-clinical drug screening is rapidly coming to pass. Ever improving differentiation protocols and advances in biomanufacturing science now make it possible to produce a number of differentiated cell types, such as neurons and heart muscle cells, from human stem cells at vast quantities far beyond what could originally be accomplished in the laboratory. With this forward progress in basic stem cell science, funding agencies and the public at large are eager to see stem cell therapies trickle into the clinic. In reality, translation from the academic laboratory has dripped into the clinic at best, due to unresolved issues with safety and efficacy. One of the most highly publicized attempts to translate stem cell therapies to the clinic was initiated by Geron Corporation in January of 2009, when they received FDA approval to begin phase I clinical trials of an embryonic stem cell based treatment for spinal cord injuries, known as GRNOPC1[181]. This approval was quickly rescinded when rodent studies raised concerns that GRNOPC1 was tumorigenic. Concerns over the safety of stem cell based therapeutics prompted the NIH and FDA to lay the groundwork for establishing regulations and guidelines to companies seeking to develop products using stem cells [176]. In addition to safety concerns, one of the main challenges in scaling up procedures for commercial scale production of stem cell products is quality control. Inherent biological variability and a lack of relevant, quantitative standards make it challenging to perform reliable batch validation, especially when quality control engineers don't have a reliable definition of what they should be shooting for.

No standardized, quantitative metrics currently exist for judging the quality of commercial stem cell-derived cardiac myocytes, so we considered more than 1,000 experimental parameters and chose 64 that we felt most rigorously define cardiac myocyte identity. These experimental measurements not only include the expression of genes important to cardiac myocyte development, they also include tissue-scale measures of sarcomere organization, electrical activity, and contractility that provide insight into how well the stem cell-derived cardiac myocytes self-organize into a useful mimetic of the myocardium. We then developed a tissue engineering test bed for assessing these parameters in stem cell-derived cardiac myocytes and comparing them against a "gold standard" established using post-natal ventricular myocytes possessing the desired phenotypic characteristics and level of maturity. This target phenotype is important for establishing the benchmark that defines whether or not batches of differentiated stem cells are suitable for research and therapeutic applications. Through quantitative integration of the magnitude and variance measured for these 64 parameters, we developed a "quality index" that scores how closely the stem cell-derived cardiac myocytes match the characteristics of the target phenotype. To validate the utility of our quality assessment rubric, we tested commercially-distributed mouse ES- and iPS-derived cardiac myocytes against neonatal mouse ventricular myocytes as our target phenotype. The combination of gene expression, morphological evaluation, electrophysiological, and contractility measurements employed allowed us to pin-point specific differences in the structural and functional properties of the ES- and iPS-derived cardiac engineered tissues versus the neonate ventricular tissues that have important implications for their utility in *in vitro* assays. Further, this "quality index" would not only allow researchers to identify

the commercial stem cell-derived myocyte product lines that are most suitable for their needs, it serves the stem cell industry as a quality assurance system for validating and improving manufacturing procedures to ensure that batches released to customers faithfully recapitulate the desired phenotype.

4.1 Design Considerations for Fabricating Engineered Myocardium from Stem Cell-Derived Cardiac Myocytes

Advances in stem cell bioprocessing methods and technologies have made commercialization of stem cell-derived myocytes for *in vitro* muscle physiology research practical.[203, 204] While quality assurance metrics exist for safety issues in the manufacture of stem cell-based products[205], no standardized guidelines currently exist for the evaluation of stem cell-derived myocyte functionality. Traditionally, myocardial differentiation is evaluated using methodologies that provide poor predictions of tissue-level cooperative function and little indication as to how closely stem cell-derived myocytes mimic native cardiac myocytes [182]. We hypothesized that the phenotypic state of stem cell-derived myocytes could be more accurately assessed by comparing and contrasting a combination of quantitative measurements taken on engineered tissues fabricated from these cells with the results obtained from tissues comprised of myocytes with a confirmed cardiac identity. To test this hypothesis, we fabricated anisotropic engineered cardiac tissues from neonatal mouse ventricular myocytes (neonate) to serve as our target phenotype, and compared them to engineered tissues comprised of either murine ES-derived myocytes (mES), or murine iPS-derived myocytes (miPS). These engineered tissues where subjected to a panel of 64 experimental measurements from 4

major categories (gene expression, myofibril structure, electrical activity, contractility) to assess their myocardial structural and functional characteristics. We also developed a quality control assessment strategy that utilizes the magnitude and variance of these measurements to provide a numeric score of how closely the stem cell-derived myocytes match the excitation-contraction coupling characteristics of a target phenotype, represented here by the neonate cardiac myocytes. This was achieved using a measure of effect size, known as Strictly Standardized Mean Difference (SSMD) that allows quantification of biological population differences. We then used the SSMD values from each experimental measurement for the mES and miPS tissues and calculated the mean squared error (*MSE*) versus the neonate tissues to evaluate the differences observed for each measurement category, as well as an overall score for all categories combined. We found that the miPS cardiac tissues exhibited lower *MSE* values than the mES cardiac tissues for every measurement category, except myofibril structure. In addition, the overall *MSE* values calculated from all of the experimental measurements combined revealed a lower *MSE* for the miPS engineered tissues than those comprised of mES-derived myocytes, suggesting that the miPS-derived cardiac myocytes more closely matched the phenotype of the neonate ventricular myocytes than the mES-derived cardiac myocytes. Taken together, the results presented in chapter 3 show that while the mES- and miPS-derived myocytes demonstrated characteristics of the cardiac myocyte lineage, they both exhibited substantially different structural and contractile properties from neonatal ventricular myocytes.

4.2 Opportunities and Challenges for Utilizing Mechanical Cues to Guide Engineered Myocardium Fabrication

The intercellular and cell-ECM interactions within a tissue govern the shape and organization that the cells comprising that tissue will ultimately adopt, and these interactions clearly play an important role in regulating the survival and functionality of those cells [25]. Microcontact printing is a well-established technique for fabricating planar cell growth substrates with precisely-defined ECM geometry. An elastomeric stamp with micrometer-scale features can be "inked" with an extracellular matrix protein of choice, such as fibronectin, laminin, or collagen, and transferred to a flat substrate that promotes protein adsorption. Cells seeded onto these substrates preferentially bind to the portions of the substrate coated with the patterned ECM protein, giving rise to a large population of cells with shapes defined by the ECM pattern [24]. This technique has been used extensively to study the relationship between shape and behavior and a number of cell types, including differentiating stem cells. The results of these studies indicate that cell geometry, is indeed and important factor in directing the lineage commitment of stem cells and continues to influence their behavior throughout their lifetime. A critical limitation of this technique is the fact that it can only be used with rigid planar substrates that do not mimic the mechanical properties of natural tissues and give rise to monolayers of cells. Three-dimensional scaffolds with natural tissue-like mechanical properties need to be developed that incorporate precise ECM cues for controlling cell shape in a non-planar substrate.

Biomaterials made today are routinely information rich and incorporate biologically active components inspired by natural analogs [206]. Researchers have

begun to design materials that combine synthetic polymer compounds with peptide motifs that can be proteolytically-cleaved by matrix metalloproteinases secreted by cells to create scaffolds that can be sculpted by cells during tissue formation [207]. Advances in the construction of three-dimensional polymeric scaffolds are also starting to make the fabrication of therapeutically-relevant artificial tissue constructs a reality [208-210]. A recently developed method derived from the micro-contact printing approach to fabricating two-dimensional tissues *in vitro* allows the fabrication of free-standing protein nanofabrics. These protein nanofabrics are constructed by micro-contact printing successive layers of ECM protein onto a rigid substrate coated with a thermosensitive polymer. These nanofabrics can be comprised of a heterogeneous composition of ECM proteins and the micro-contact printing technique provides control over the shape, size, and orientation of the protein "threads" with respect to one another. Further, cells will readily adhere to these ECM fabrics and stacking of these nanofabrics may allow the construction of ECM scaffolds with precise organizational cues throughout the volume of the scaffold [211]. Another promising approach for fabricating three-dimensional ECM tissue scaffolds with precise geometry is the recently developed rotary jet spinning technique for generating fibrous tissue scaffolds [212]. This technique overcomes the limitations of the traditional electrospinning technique to produce highly aligned nanoscale fibers using a nozzle rotating at high speed to produce a jet of polymer solution that undergoes extensive stretching before polymerization. The primary advantage of this technique over other methods of three-dimensional scaffold production is its ability to quickly produce large quantities of tissue scaffolds of arbitrary size composed of precisely aligned protein nanofibers. The focus of future biomaterials design will likely

be focused on the development of "smart" materials that integrate multiple inputs from both chemical and mechanical stimuli to direct their behavior [209]. Such materials could simplify and optimize engineered tissue fabrication by more closely reproducing the dynamic microenviroment presented to differentiating cells during development, allowing researchers to take advantage of the natural interactions between cells and their environment during tissue morphogenesis to reproducibly drive the fate commitment of cells without the need for complex experimental manipulations.

4.3 Opportunities and Challenges for Assessing the Quality of Mass Produced Stem Cell-Derived Cardiac Myocytes

An important final consideration in the fabrication of engineered tissues from uncommitted stem cells is the evaluation of functional performance characteristics of the artificial tissue. Traditionally, differentiation has been assessed by measuring the expression of specific marker genes. However, this metric requires destruction of the tissue to isolate mRNA for measurement and is not informative for cells and tissues that require the precise assembly and organization of macromolecular structures, such as the sarcomeres of striated muscle for their functionality. Biomimetic microfluidic devices are emerging as a promising platform for measuring the performance characteristics of engineered tissues *in vitro*. A recent study provided the first proof of principle demonstration of this approach to model the structural, functional, and mechanical properties of the alveolar-capillary interface of the human lung. This microfluidic device was not only able to reproduce the functionality of an alveoli, it also allowed the identification of novel mechanosensitive responses of the lungs to nanoparticulates [213].

Application of these organ-on-chip devices to the fabrication of tissues using stem cells could provide a powerful tool for the quantitative analysis of stem cell derived artificial tissues. Evaluation of the functional characteristics of muscle tissue is especially challenging, as traditional assays are not able to provide direct measurements of their contractile performance. A novel muscular thin film assay was recently developed that allows direct measurement of the contractile force of engineered muscle tissues [149]. This assay has been successfully used to demonstrate the myogenic potential of mouse cardiac progenitor cells isolated from the primary and secondary heart fields during various stages of cardiogenesis [214]. Subsequent modifications to the muscular thin film assay have made it amenable to the evaluation of smooth muscle cell contractility, in addition to striated muscle contractility, and allow the simultaneous measurement of multiple engineered muscle constructs in the same dish [161]. As the field of regenerative medicine advances, and the complexity of engineered tissues increase, new approaches will be needed to evaluate the utility of these tissues for therapeutic applications. Cell-based biochips represent an attractive test system that negate the need for costly animal models and allow quantitative analyses of tissue function that are not possible in traditional cell culture systems.

4.4 Dissertation Summary

In this body of work, we determined that two-dimensional engineered tissues comprised of isolated neonatal ventricular myocytes could recapitulate the structural and functional aspects of the adult ventricular myocardium. Furthermore, we showed that engineered tissues comprised of neonatal mouse ventricular myocytes could serve as a

suitable target phenotype for assessing the ability of murine stem cell-derived cardiac myocytes to form functional ventricular tissue analogs using a quantitative rubric of 64 essential parameters of cardiac myocyte phenotype.

4.5 Funding Sources

The research described in chapters 1 and 2 were funded by the Nanoscale Science and Engineering Center of the National Science Foundation under NSF award number PHY-0117795, the Harvard Materials Research Science and Engineering Center under NSF award number DMR-0213805, the Harvard Stem Cell Institute and GlaxoSmithKline, NIH/NINDS grant 1 U01 NS073474-01, and NIH grant 1 R01 HL079126. The work described in chapter 3 was supported by the the NIH/NHLBI for Human Pluripotent Stem Cells and Progenitor Models of Cardiac and Blood Diseases (U01 HL100408-02), and the NIH for a Human Cardio-Pulmonary System on a Chip research grant (UH2 TR000522-01). The author would also like to gratefully acknowledge the Harvard Center for Nanoscale Systems (CNS) for use of their microfabrication facilities, and Axiogenesis for providing Cor.At murine ES- and iPS-derived myocytes and Cor.At culture media for the studies described in chapter 3.

5 Bibliography

[1] Ingber DE. The riddle of morphogenesis: a question of solution chemistry or molecular cell engineering? Cell. 1993;75:1249-52.

[2] Parker KK, Ingber DE. Extracellular matrix, mechanotransduction and structural hierarchies in heart tissue engineering. Philos Trans R Soc Lond B Biol Sci. 2007;362:1267-79.

[3] Ingber DE. Cellular mechanotransduction: putting all the pieces together again. Faseb J. 2006;20:811-27.

[4] Ingber DE. Mechanical control of tissue morphogenesis during embryological development. Int J Dev Biol. 2006;50:255-66.

[5] Wozniak MA, Chen CS. Mechanotransduction in development: a growing role for contractility. Nat Rev Mol Cell Biol. 2009;10:34-43.

[6] Chen CS, Tan J, Tien J. Mechanotransduction at cell-matrix and cell-cell contacts. Annu Rev Biomed Eng. 2004;6:275-302.

[7] Jamora C, DasGupta R, Kocieniewski P, Fuchs E. Links between signal transduction, transcription and adhesion in epithelial bud development. Nature. 2003;422:317-22.

[8] Moore KA, Polte T, Huang S, Shi B, Alsberg E, Sunday ME, et al. Control of basement membrane remodeling and epithelial branching morphogenesis in embryonic lung by Rho and cytoskeletal tension. Dev Dyn. 2005;232:268-81.

[9] Ingber DE. Mechanical signaling and the cellular response to extracellular matrix in angiogenesis and cardiovascular physiology. Circ Res. 2002;91:877-87.

[10] Latacha KS, Remond MC, Ramasubramanian A, Chen AY, Elson EL, Taber LA. Role of actin polymerization in bending of the early heart tube. Dev Dyn. 2005;233:1272-86.

[11] Taber LA. Biomechanics of cardiovascular development. Annu Rev Biomed Eng. 2001;3:1-25.

[12] Itasaki N, Nakamura H, Sumida H, Yasuda M. Actin bundles on the right side in the caudal part of the heart tube play a role in dextro-looping in the embryonic chick heart. Anat Embryol (Berl). 1991;183:29-39.

[13] Jacot JG, Martin JC, Hunt DL. Mechanobiology of cardiomyocyte development. Journal of biomechanics. 2010;43:93-8.

[14] McCain ML, Parker KK. Mechanotransduction: the role of mechanical stress, myocyte shape, and cytoskeletal architecture on cardiac function. Pflugers Arch. 2011;462:89-104.

[15] Evans SM, Yelon D, Conlon FL, Kirby ML. Myocardial lineage development. Circ Res. 2010;107:1428-44.

[16] Taber LA, Lin IE, Clark EB. Mechanics of cardiac looping. Dev Dyn. 1995;203:42-50.

[17] Damon BJ, Remond MC, Bigelow MR, Trusk TC, Xie W, Perucchio R, et al. Patterns of muscular strain in the embryonic heart wall. Dev Dyn. 2009;238:1535-46.

[18] Srivastava D, Olson EN. A genetic blueprint for cardiac development. Nature. 2000;407:221-6.

[19] Price RL, Chintanowonges C, Shiraishi I, Borg TK, Terracio L. Local and regional variations in myofibrillar patterns in looping rat hearts. Anat Rec. 1996;245:83-93.

[20] Heineke J, Molkentin JD. Regulation of cardiac hypertrophy by intracellular signalling pathways. Nat Rev Mol Cell Biol. 2006;7:589-600.

[21] Frey N, Olson EN. Cardiac hypertrophy: the good, the bad, and the ugly. Annu Rev Physiol. 2003;65:45-79.

[22] Sheehy SP, Huang S, Parker KK. Time-warped comparison of gene expression in adaptive and maladaptive cardiac hypertrophy. Circ Cardiovasc Genet. 2009;2:116-24.

[23] Alenghat FJ, Ingber DE, Ingber DE. Mechanotransduction: all signals point to cytoskeleton, matrix, and integrins. Sci STKE. 2002;2002:pe6.

[24] Singhvi R, Kumar A, Lopez GP, Stephanopoulos GN, Wang DI, Whitesides GM, et al. Engineering cell shape and function. Science. 1994;264:696-8.

[25] Chen CS, Mrksich M, Huang S, Whitesides GM, Ingber DE. Geometric control of cell life and death. Science. 1997;276:1425-8.

[26] Bray M-A, Sheehy SP, Parker KK. Sarcomere alignment is regulated by myocyte shape. Cell Motil Cytoskeleton. 2008;65:641-51.

[27] Parker KK, Brock AL, Brangwynne C, Mannix RJ, Wang N, Ostuni E, et al. Directional control of lamellipodia extension by constraining cell shape and orienting cell tractional forces. Faseb J. 2002;16:1195-204.

[28] Schwartz MA, Schaller MD, Ginsberg MH. Integrins: emerging paradigms of signal transduction. Annu Rev Cell Dev Biol. 1995;11:549-99.

[29] Price RL, Nakagawa M, Terracio L, Borg TK. Ultrastructural localization of laminin on in vivo embryonic, neonatal, and adult rat cardiac myocytes and in early rat embryos raised in whole-embryo culture. J Histochem Cytochem. 1992;40:1373-81.

[30] Ross RS, Borg TK. Integrins and the myocardium. Circ Res. 2001;88:1112-9.

[31] Terracio L, Rubin K, Gullberg D, Balog E, Carver W, Jyring R, et al. Expression of collagen binding integrins during cardiac development and hypertrophy. Circ Res. 1991;68:734-44.

[32] Farhadian F, Contard F, Corbier A, Barrieux A, Rappaport L, Samuel JL. Fibronectin expression during physiological and pathological cardiac growth. J Mol Cell Cardiol. 1995;27:981-90.

[33] Samuel JL, Farhadian F, Sabri A, Marotte F, Robert V, Rappaport L. Expression of fibronectin during rat fetal and postnatal development: an in situ hybridisation and immunohistochemical study. Cardiovasc Res. 1994;28:1653-61.

[34] Carver W, Price RL, Raso DS, Terracio L, Borg TK. Distribution of beta-1 integrin in the developing rat heart. J Histochem Cytochem. 1994;42:167-75.

[35] Hilenski LL, Ma XH, Vinson N, Terracio L, Borg TK. The role of beta 1 integrin in spreading and myofibrillogenesis in neonatal rat cardiomyocytes in vitro. Cell Motil Cytoskeleton. 1992;21:87-100.

[36] Hornberger LK, Singhroy S, Cavalle-Garrido T, Tsang W, Keeley F, Rabinovitch M. Synthesis of extracellular matrix and adhesion through beta(1) integrins are critical for fetal ventricular myocyte proliferation. Circ Res. 2000;87:508-15.

[37] Belkin AM, Zhidkova NI, Balzac F, Altruda F, Tomatis D, Maier A, et al. Beta 1D integrin displaces the beta 1A isoform in striated muscles: localization at junctional structures and signaling potential in nonmuscle cells. J Cell Biol. 1996;132:211-26.

[38] van der Flier A, Gaspar AC, Thorsteinsdottir S, Baudoin C, Groeneveld E, Mummery CL, et al. Spatial and temporal expression of the beta1D integrin during mouse development. Dev Dyn. 1997;210:472-86.

[39] de Melker AA, Sonnenberg A. Integrins: alternative splicing as a mechanism to regulate ligand binding and integrin signaling events. Bioessays. 1999;21:499-509.

[40] Keller RS, Shai SY, Babbitt CJ, Pham CG, Solaro RJ, Valencik ML, et al. Disruption of integrin function in the murine myocardium leads to perinatal lethality, fibrosis, and abnormal cardiac performance. Am J Pathol. 2001;158:1079-90.

[41] Shai S-Y, Harpf AE, Babbitt CJ, Jordan MC, Fishbein MC, Chen J, et al. Cardiac myocyte-specific excision of the beta1 integrin gene results in myocardial fibrosis and cardiac failure. Circ Res. 2002;90:458-64.

[42] Wang N, Butler JP, Ingber DE. Mechanotransduction across the cell surface and through the cytoskeleton. Science. 1993;260:1124-7.

[43] Matthews BD, Overby DR, Mannix R, Ingber DE. Cellular adaptation to mechanical stress: role of integrins, Rho, cytoskeletal tension and mechanosensitive ion channels. J Cell Sci. 2006;119:508-18.

[44] Meyer CJ, Alenghat FJ, Rim P, Fong JH, Fabry B, Ingber DE. Mechanical control of cyclic AMP signalling and gene transcription through integrins. Nat Cell Biol. 2000;2:666-8.

[45] Burridge K, Chrzanowska-Wodnicka M. Focal adhesions, contractility, and signaling. Annu Rev Cell Dev Biol. 1996;12:463-518.

[46] Schwartz MA, Ginsberg MH. Networks and crosstalk: integrin signalling spreads. Nat Cell Biol. 2002;4:E65-8.

[47] Samarel AM. Costameres, focal adhesions, and cardiomyocyte mechanotransduction. Am J Physiol Heart Circ Physiol. 2005;289:H2291-301.

[48] Discher DE, Mooney DJ, Zandstra PW. Growth Factors, Matrices, and Forces Combine and Control Stem Cells. Science. 2009;324:1673-7.

[49] Fletcher DA, Mullins D. Cell mechanics and the cytoskeleton. Nature. 2010;463:485-92.

[50] Wang N, Tytell JD, Ingber DE. Mechanotransduction at a distance: mechanically coupling the extracellular matrix with the nucleus. Nat Rev Mol Cell Biol. 2009;10:75-82.

[51] Gjorevski N, Nelson CM. Bidirectional extracellular matrix signaling during tissue morphogenesis. Cytokine Growth Factor Rev. 2009;20:459-65.

[52] Dahl KN, Ribeiro AJS, Lammerding J. Nuclear shape, mechanics, and mechanotransduction. Circ Res. 2008;102:1307-18.

[53] Brancaccio M, Guazzone S, Menini N, Sibona E, Hirsch E, De Andrea M, et al. Melusin is a new muscle-specific interactor for beta(1) integrin cytoplasmic domain. J Biol Chem. 1999;274:29282-8.

[54] Brancaccio M, Fratta L, Notte A, Hirsch E, Poulet R, Guazzone S, et al. Melusin, a muscle-specific integrin beta1-interacting protein, is required to prevent cardiac failure in response to chronic pressure overload. Nat Med. 2003;9:68-75.

[55] Knoll R, Hoshijima M, Hoffman HM, Person V, Lorenzen-Schmidt I, Bang M-L, et al. The cardiac mechanical stretch sensor machinery involves a Z disc complex that is defective in a subset of human dilated cardiomyopathy. Cell. 2002;111:943-55.

[56] Heineke J, Ruetten H, Willenbockel C, Gross SC, Naguib M, Schaefer A, et al. Attenuation of cardiac remodeling after myocardial infarction by muscle LIM protein-calcineurin signaling at the sarcomeric Z-disc. Proc Natl Acad Sci U S A. 2005;102:1655-60.

[57] Puchner EM, Alexandrovich A, Kho AL, Hensen U, Schafer LV, Brandmeier B, et al. Mechanoenzymatics of titin kinase. Proc Natl Acad Sci U S A. 2008;105:13385-90.

[58] Sheikh F, Raskin A, Chu P-H, Lange S, Domenighetti AA, Zheng M, et al. An FHL1-containing complex within the cardiomyocyte sarcomere mediates hypertrophic biomechanical stress responses in mice. J Clin Invest. 2008;118:3870-80.

[59] Lange S, Xiang F, Yakovenko A, Vihola A, Hackman P, Rostkova E, et al. The kinase domain of titin controls muscle gene expression and protein turnover. Science. 2005;308:1599-603.

[60] Lange S, Auerbach D, McLoughlin P, Perriard E, Schafer BW, Perriard J-C, et al. Subcellular targeting of metabolic enzymes to titin in heart muscle may be mediated by DRAL/FHL-2. J Cell Sci. 2002;115:4925-36.

[61] Kruger M, Linke WA. Titin-based mechanical signalling in normal and failing myocardium. J Mol Cell Cardiol. 2009;46:490-8.

[62] Boateng SY, Belin RJ, Geenen DL, Margulies KB, Martin JL, Hoshijima M, et al. Cardiac dysfunction and heart failure are associated with abnormalities in the subcellular distribution and amounts of oligomeric muscle LIM protein. Am J Physiol Heart Circ Physiol. 2007;292:H259-69.

[63] Linke WA. Sense and stretchability: the role of titin and titin-associated proteins in myocardial stress-sensing and mechanical dysfunction. Cardiovasc Res. 2008;77:637-48.

[64] Maniotis AJ, Bojanowski K, Ingber DE. Mechanical continuity and reversible chromosome disassembly within intact genomes removed from living cells. J Cell Biochem. 1997;65:114-30.

[65] Maniotis AJ, Chen CS, Ingber DE. Demonstration of mechanical connections between integrins, cytoskeletal filaments, and nucleoplasm that stabilize nuclear structure. Proc Natl Acad Sci U S A. 1997;94:849-54.

[66] Thomas CH, Collier JH, Sfeir CS, Healy KE. Engineering gene expression and protein synthesis by modulation of nuclear shape. Proc Natl Acad Sci U S A. 2002;99:1972-7.

[67] Bray M-AP, Adams WJ, Geisse NA, Feinberg AW, Sheehy SP, Parker KK. Nuclear morphology and deformation in engineered cardiac myocytes and tissues. Biomaterials. 2009;31:5143-50.

[68] Brangwynne CP, Koenderink GH, Mackintosh FC, Weitz DA. Nonequilibrium microtubule fluctuations in a model cytoskeleton. Phys Rev Lett. 2008;100:118104.

[69] Ingber DE. Tensegrity: the architectural basis of cellular mechanotransduction. Annu Rev Physiol. 1997;59:575-99.

[70] Samarakoon R, Higgins PJ. MEK/ERK pathway mediates cell-shape-dependent plasminogen activator inhibitor type 1 gene expression upon drug-induced disruption of the microfilament and microtubule networks. J Cell Sci. 2002;115:3093-103.

[71] Olson EN, Nordheim A. Linking actin dynamics and gene transcription to drive cellular motile functions. Nat Rev Mol Cell Biol. 2010;11:353-65.

[72] Kuwahara K, Barrientos T, Pipes GCT, Li S, Olson EN. Muscle-specific signaling mechanism that links actin dynamics to serum response factor. Mol Cell Biol. 2005;25:3173-81.

[73] Kuwahara K, Teg Pipes GC, McAnally J, Richardson JA, Hill JA, Bassel-Duby R, et al. Modulation of adverse cardiac remodeling by STARS, a mediator of MEF2 signaling and SRF activity. J Clin Invest. 2007;117:1324-34.

[74] Mack CP, Somlyo AV, Hautmann M, Somlyo AP, Owens GK. Smooth muscle differentiation marker gene expression is regulated by RhoA-mediated actin polymerization. J Biol Chem. 2001;276:341-7.

[75] Mammoto A, Connor KM, Mammoto T, Yung CW, Huh D, Aderman CM, et al. A mechanosensitive transcriptional mechanism that controls angiogenesis. Nature. 2009;457:1103-8.

[76] Simpson DG, Decker ML, Clark WA, Decker RS. Contractile activity and cell-cell contact regulate myofibrillar organization in cultured cardiac myocytes. J Cell Biol. 1993;123:323-36.

[77] Kresh JY, Chopra A. Intercellular and extracellular mechanotransduction in cardiac myocytes. Pflugers Arch. 2011;462:75-87.

[78] Peters NS, Severs NJ, Rothery SM, Lincoln C, Yacoub MH, Green CR. Spatiotemporal relation between gap junctions and fascia adherens junctions during postnatal development of human ventricular myocardium. Circulation. 1994;90:713-25.

[79] Niessen CM, Leckband D, Yap AS. Tissue organization by cadherin adhesion molecules: dynamic molecular and cellular mechanisms of morphogenetic regulation. Physiol Rev. 2011;91:691-731.

[80] Miyake Y, Inoue N, Nishimura K, Kinoshita N, Hosoya H, Yonemura S. Actomyosin tension is required for correct recruitment of adherens junction components and zonula occludens formation. Exp Cell Res. 2006;312:1637-50.

[81] Liu Z, Tan JL, Cohen DM, Yang MT, Sniadecki NJ, Ruiz SA, et al. Mechanical tugging force regulates the size of cell-cell junctions. Proc Natl Acad Sci U S A. 2010;107:9944-9.

[82] Nelson WJ, Nusse R. Convergence of Wnt, beta-catenin, and cadherin pathways. Science. 2004;303:1483-7.

[83] Gessert S, Kuhl M. The multiple phases and faces of wnt signaling during cardiac differentiation and development. Circ Res. 2010;107:186-99.

[84] Androutsellis-Theotokis A, Leker RR, Soldner F, Hoeppner DJ, Ravin R, Poser SW, et al. Notch signalling regulates stem cell numbers in vitro and in vivo. Nature. 2006;442:823-6.

[85] Boni A, Urbanek K, Nascimbene A, Hosoda T, Zheng H, Delucchi F, et al. Notch1 regulates the fate of cardiac progenitor cells. Proc Natl Acad Sci U S A. 2008;105:15529-34.

[86] Ueno S, Weidinger G, Osugi T, Kohn AD, Golob JL, Pabon L, et al. Biphasic role for Wnt/beta-catenin signaling in cardiac specification in zebrafish and embryonic stem cells. Proc Natl Acad Sci U S A. 2007;104:9685-90.

[87] Rao TP, Kuhl M. An updated overview on Wnt signaling pathways: a prelude for more. Circ Res. 2010;106:1798-806.

[88] Kwon C, Qian L, Cheng P, Nigam V, Arnold J, Srivastava D. A regulatory pathway involving Notch1/beta-catenin/Isl1 determines cardiac progenitor cell fate. Nat Cell Biol. 2009;11:951-7.

[89] Combs MD, Yutzey KE. Heart valve development: regulatory networks in development and disease. Circ Res. 2009;105:408-21.

[90] Yang J-H, Wylie-Sears J, Bischoff J. Opposing actions of Notch1 and VEGF in post-natal cardiac valve endothelial cells. Biochem Biophys Res Commun. 2008;374:512-6.

[91] Hove JR, Koster RW, Forouhar AS, Acevedo-Bolton G, Fraser SE, Gharib M. Intracardiac fluid forces are an essential epigenetic factor for embryonic cardiogenesis. Nature. 2003;421:172-7.

[92] Miller LA. Fluid dynamics of ventricular filling in the embryonic heart. Cell Biochem Biophys. 2011;61:33-45.

[93] Santhanakrishnan A, Miller LA. Fluid dynamics of heart development. Cell Biochem Biophys. 2011;61:1-22.

[94] Balachandran K, Alford PW, Wylie-Sears J, Goss JA, Grosberg A, Bischoff J, et al. Cyclic strain induces dual-mode endothelial-mesenchymal transformation of the cardiac valve. Proc Natl Acad Sci U S A. 2011;108:19943-8.

[95] Arciniegas E, Frid MG, Douglas IS, Stenmark KR. Perspectives on endothelial-to-mesenchymal transition: potential contribution to vascular remodeling in chronic pulmonary hypertension. Am J Physiol Lung Cell Mol Physiol. 2007;293:L1-8.

[96] Saffitz JE, Kleber AG. Effects of mechanical forces and mediators of hypertrophy on remodeling of gap junctions in the heart. Circ Res. 2004;94:585-91.

[97] Saffitz JE. Dependence of electrical coupling on mechanical coupling in cardiac myocytes: insights gained from cardiomyopathies caused by defects in cell-cell connections. Ann N Y Acad Sci. 2005;1047:336-44.

[98] Gourdie RG, Green CR, Severs NJ, Thompson RP. Immunolabelling patterns of gap junction connexins in the developing and mature rat heart. Anat Embryol (Berl). 1992;185:363-78.

[99] McCain ML, Desplantez T, Geisse NA, Rothen-Rutishauser B, Oberer H, Parker KK, et al. Cell-to-cell coupling in engineered pairs of rat ventricular cardiomyocytes: relation between Cx43 immunofluorescence and intercellular electrical conductance. Am J Physiol Heart Circ Physiol. 2012;302:H443-50.

[100] Bursac N, Parker KK, Iravanian S, Tung L. Cardiomyocyte cultures with controlled macroscopic anisotropy: a model for functional electrophysiological studies of cardiac muscle. Circ Res. 2002;91:e45-54.

[101] Chung C-Y, Bien H, Entcheva E. The role of cardiac tissue alignment in modulating electrical function. J Cardiovasc Electrophysiol. 2007;18:1323-9.

[102] Manasek FJ, Burnside MB, Waterman RE. Myocardial cell shape change as a mechanism of embryonic heart looping. Dev Biol. 1972;29:349-71.

[103] Pijnappels DA, Schalij MJ, Ramkisoensing AA, van Tuyn J, de Vries AAF, van der Laarse A, et al. Forced alignment of mesenchymal stem cells undergoing cardiomyogenic differentiation affects functional integration with cardiomyocyte cultures. Circ Res. 2008;103:167-76.

[104] Geisse NA, Sheehy SP, Parker KK. Control of myocyte remodeling in vitro with engineered substrates. In Vitro Cell Dev Biol Anim. 2009;45:343-50.

[105] Fu J, Wang Y-K, Yang MT, Desai RA, Yu X, Liu Z, et al. Mechanical regulation of cell function with geometrically modulated elastomeric substrates. Nat Methods. 2010;7:733-6.

[106] Walsh KB, Parks GE. Changes in cardiac myocyte morphology alter the properties of voltage-gated ion channels. Cardiovasc Res. 2002;55:64-75.

[107] Pong T, Adams WJ, Bray M-A, Feinberg AW, Sheehy SP, Werdich AA, et al. Hierarchical architecture influences calcium dynamics in engineered cardiac muscle. Exp Biol Med (Maywood). 2011;236:366-73.

[108] Yin L, Bien H, Entcheva E. Scaffold topography alters intracellular calcium dynamics in cultured cardiomyocyte networks. Am J Physiol Heart Circ Physiol. 2004;287:H1276-85.

[109] Alford PW, Nesmith AP, Seywerd JN, Grosberg A, Parker KK. Vascular smooth muscle contractility depends on cell shape. Integr Biol (Camb). 2011;3:1063-70.

[110] Georges PC, Janmey PA. Cell type-specific response to growth on soft materials. J Appl Physiol. 2005;98:1547-53.

[111] Pelham RJ, Jr., Wang Yl. Cell locomotion and focal adhesions are regulated by substrate flexibility. Proc Natl Acad Sci U S A. 1997;94:13661-5.

[112] Huebsch N, Arany PR, Mao AS, Shvartsman D, Ali OA, Bencherif SA, et al. Harnessing traction-mediated manipulation of the cell/matrix interface to control stem-cell fate. Nature Materials. 2010;9:518-26.

[113] Guilak F, Cohen DM, Estes BT, Gimble JM, Liedtke W, Chen CS. Control of stem cell fate by physical interactions with the extracellular matrix. Cell Stem Cell. 2009;5:17-26.

[114] Engler AJ, Carag-Krieger C, Johnson CP, Raab M, Tang HY, Speicher DW, et al. Embryonic cardiomyocytes beat best on a matrix with heart-like elasticity: scar-like rigidity inhibits beating. J Cell Sci. 2008;121:3794-802.

[115] Tobita K, Schroder EA, Tinney JP, Garrison JB, Keller BB. Regional passive ventricular stress-strain relations during development of altered loads in chick embryo. Am J Physiol Heart Circ Physiol. 2002;282:H2386-96.

[116] Bajaj P, Tang X, Saif TA, Bashir R. Stiffness of the substrate influences the phenotype of embryonic chicken cardiac myocytes. J Biomed Mater Res A. 2010;95:1261-9.

[117] Bhana B, Iyer RK, Chen WLK, Zhao R, Sider KL, Likhitpanichkul M, et al. Influence of substrate stiffness on the phenotype of heart cells. Biotechnol Bioeng. 2010;105:1148-60.

[118] Jacot JG, McCulloch AD, Omens JH. Substrate stiffness affects the functional maturation of neonatal rat ventricular myocytes. Biophys J. 2008;95:3479-87.

[119] Engler AJ, Sen S, Sweeney HL, Discher DE. Matrix elasticity directs stem cell lineage specification. Cell. 2006;126:677-89.

[120] Zajac AL, Discher DE. Cell differentiation through tissue elasticity-coupled, myosin-driven remodeling. Curr Opin Cell Biol. 2008;20:609-15.

[121] Balaban NQ, Schwarz US, Riveline D, Goichberg P, Tzur G, Sabanay I, et al. Force and focal adhesion assembly: a close relationship studied using elastic micropatterned substrates. Nat Cell Biol. 2001;3:466-72.

[122] Manasek FJ, Monroe RG. Early cardiac morphogenesis is independent of function. Dev Biol. 1972;27:584-8.

[123] Auman HJ, Coleman H, Riley HE, Olale F, Tsai H-J, Yelon D. Functional modulation of cardiac form through regionally confined cell shape changes. PLoS Biol. 2007;5:e53.

[124] Trepat X, Deng L, An SS, Navajas D, Tschumperlin DJ, Gerthoffer WT, et al. Universal physical responses to stretch in the living cell. Nature. 2007;447:592-5.

[125] Shanker AJ, Yamada K, Green KG, Yamada KA, Saffitz JE. Matrix-protein-specific regulation of Cx43 expression in cardiac myocytes subjected to mechanical load. Circ Res. 2005;96:558-66.

[126] Salameh A, Wustmann A, Karl S, Blanke K, Apel D, Rojas-Gomez D, et al. Cyclic mechanical stretch induces cardiomyocyte orientation and polarization of the gap junction protein connexin43. Circ Res. 2010;106:1592-602.

[127] Yamada K, Green KG, Samarel AM, Saffitz JE. Distinct pathways regulate expression of cardiac electrical and mechanical junction proteins in response to stretch. Circ Res. 2005;97:346-53.

[128] Zhuang J, Yamada KA, Saffitz JE, Kleber AG. Pulsatile stretch remodels cell-to-cell communication in cultured myocytes. Circ Res. 2000;87:316-22.

[129] Frank D, Kuhn C, Brors B, Hanselmann C, Ludde M, Katus HA, et al. Gene expression pattern in biomechanically stretched cardiomyocytes: evidence for a stretch-specific gene program. Hypertension. 2008;51:309-18.

[130] Gopalan SM, Flaim C, Bhatia SN, Hoshijima M, Knoell R, Chien KR, et al. Anisotropic stretch-induced hypertrophy in neonatal ventricular myocytes micropatterned on deformable elastomers. Biotechnol Bioeng. 2003;81:578-87.

[131] Cadre BM, Qi M, Eble DM, Shannon TR, Bers DM, Samarel AM. Cyclic stretch down-regulates calcium transporter gene expression in neonatal rat ventricular myocytes. J Mol Cell Cardiol. 1998;30:2247-59.

[132] Mrksich M, Dike LE, Tien J, Ingber DE, Whitesides GM. Using microcontact printing to pattern the attachment of mammalian cells to self-assembled monolayers of alkanethiolates on transparent films of gold and silver. Exp Cell Res. 1997;235:305-13.

[133] Mrksich M, Chen CS, Xia Y, Dike LE, Ingber DE, Whitesides GM. Controlling cell attachment on contoured surfaces with self-assembled monolayers of alkanethiolates on gold. Proc Natl Acad Sci U S A. 1996;93:10775-8.

[134] Novak IL, Slepchenko BM, Mogilner A, Loew LM. Cooperativity between cell contractility and adhesion. Phys Rev Lett. 2004;93:268109.

[135] Deshpande VS, McMeeking RM, Evans AG. A bio-chemo-mechanical model for cell contractility. Proc Natl Acad Sci U S A. 2006;103:14015-20.

[136] Deshpande VS, Mrksich M, McMeeking RM, Evans AG. A bio-mechanical model for coupling cell contractility with focal adhesion formation. Journal of the Mechanics and Physics of Solids. 2008;56:1484-510.

[137] Paszek MJ, Boettiger D, Weaver VM, Hammer DA. Integrin clustering is driven by mechanical resistance from the glycocalyx and the substrate. PLoS Computational Biology. 2009;5.

[138] Grosberg A, Kuo P-L, Guo C-L, Geisse NA, Bray M-A, Adams WJ, et al. Self-organization of muscle cell structure and function. PLoS Comput Biol. 2011;7:e1001088.

[139] Parker KK, Tan J, Chen CS, Tung L. Myofibrillar architecture in engineered cardiac myocytes. Circ Res. 2008;103:340-2.

[140] Goktepe S, Abilez OJ, Parker KK, Kuhl E. A multiscale model for eccentric and concentric cardiac growth through sarcomerogenesis. J Theor Biol. 2010;265:433-42.

[141] Latimer DC, Roth BJ, Parker KK. Analytical model for predicting mechanotransduction effects in engineered cardiac tissue. Tissue Eng. 2003;9:283-9.

[142] Discher D, Dong C, Fredberg JJ, Guilak F, Ingber D, Janmey P, et al. Biomechanics: cell research and applications for the next decade. Ann Biomed Eng. 2009;37:847-59.

[143] Sheehy SP, Grosberg A, Parker KK. The contribution of cellular mechanotransduction to cardiomyocyte form and function. Biomechanics and Modeling in Mechanobiology. 2012;11:1227-39.

[144] Manner J. On rotation, torsion, lateralization, and handedness of the embryonic heart loop: New insights from a simulation model for the heart loop of chick embryos. The Anatomical Record Part A: Discoveries in Molecular, Cellular, and Evolutionary Biology. 2004;278A:481-92.

[145] Carreras F, Ballester M, Pujadas S, Leta R, Pons-Llado G. Morphological and functional evidences of the helical heart from non-invasive cardiac imaging. European Journal of Cardio-Thoracic Surgery. 2006;29:S50-5.

[146] Torrent-Guasp F, Kocica MJ, Corno AF, Komeda M, Carreras-Costa F, Flotats A, et al. Towards new understanding of the heart structure and function. European Journal of Cardio-Thoracic Surgery. 2005;27:191-201.

[147] Streeter Jr. DD, Spotnitz HM, Patel DP, Ross J, Sonnenblick EH. Fiber Orientation in the Canine Left Ventricle during Diastole and Systole. Circ Res. 1969;24:339-47.

[148] Hudlicka O, Brown MD. Postnatal growth of the heart and its blood vessels. J Vasc Res. 1996;33:266-87.

[149] Feinberg AW, Feigel A, Shevkoplyas SS, Sheehy S, Whitesides GM, Parker KK. Muscular thin films for building actuators and powering devices. Science. 2007;317:1366-70.

[150] Navé BT, Becker M, Roenicke V, Henkel T. Validation of targets and drug candidates in an engineered three-dimensional cardiac tissue model. Drug Discovery Today. 2002;7:419-25.

[151] Rothen-Rutishauser BM, Ehler E, Perriard E, Messerli JM, Perriard JC. Different Behaviour of the Non-sarcomeric Cytoskeleton in Neonatal and Adult Rat Cardiomyocytes. J Mol Cell Cardiol. 1998;30:19-31.

[152] Leuranguer V, Monteil A, Bourinet E, Dayanithi G, Nargeot J. T-type calcium currents in rat cardiomyocytes during postnatal development: contribution to hormone secretion. Am J Physiol-Heart Circul Physiol. 2000;279:H2540-H8.

[153] Ferron L, Capuano V, Deroubaix E, Coulombe A, Renaud JF. Functional and molecular characterization of a T-type Ca2+ channel during fetal and postnatal rat heart development. J Mol Cell Cardiol. 2002;34:533-46.

[154] Schroder EA, Wei YD, Satin J. The developing cardiac myocyte - Maturation of excitability and excitation-contraction coupling. In: Sideman S, Beyar R, Landesberg A, editors. Interactive and Integrative Cardiology. Oxford: Blackwell Publishing; 2006. p. 63-75.

[155] Kilborn MJ, Fedida D. A study of the developmental changes in outward currents of rat ventricular myocytes. J Physiol-London. 1990;430:37-60.

[156] Du AP, Sanger JM, Sanger JW. Cardiac myofibrillogenesis inside intact embryonic hearts. Dev Biol. 2008;318:236-46.

[157] Jacot JG, Kita-Matsuo H, Wei KA, Vincent Chen HS, Omens JH, Mercola M, et al. Cardiac myocyte force development during differentiation and maturation. Ann N Y Acad Sci. 2010;1188:121-7.

[158] Grosberg A, Kuo PL, Guo CL, Geisse NA, Bray MA, Adams WJ, et al. Self-Organization of Muscle Cell Structure and Function. PLoS Computational Biology. 2011;7.

[159] Pong T, Adams WJ, Bray MA, Feinberg AW, Sheehy SP, Werdich AA, et al. Hierarchical architecture influences calcium dynamics in engineered cardiac muscle. Exp Biol Med (Maywood). 2011;236:366-73.

[160] Feinberg AW, Alford PW, Jin H, Ripplinger CM, Werdich AA, Sheehy SP, et al. Controlling the contractile strength of engineered cardiac muscle by hierarchal tissue architecture. Biomaterials. 2012;33:5732-41.

[161] Alford PW, Feinberg AW, Sheehy SP, Parker KK. Biohybrid thin films for measuring contractility in engineered cardiovascular muscle. Biomaterials. 2010;31:3613-21.

[162] Effron MB, Bhatnagar GM, Spurgeon HA, Ruano-Arroyo G, Lakatta EG. Changes in myosin isoenzymes, ATPase activity, and contraction duration in rat cardiac muscle with aging can be modulated by thyroxine. Circ Res. 1987;60:238-45.

[163] Uehata M, Ishizaki T, Satoh H, Ono T, Kawahara T, Morishita T, et al. Calcium sensitization of smooth muscle mediated by a Rho-associated protein kinase in hypertension. Nature. 1997;389:990-4.

[164] Lakatta EG, Gerstenblith G, Angell CS, Shock NW, Weisfeldt ML. Prolonged contraction duration in aged myocardium. J Clin Invest. 1975;55:61-8.

[165] van RJ, van den BF. Cumulative dose-response curves. I. Introduction to the technique. Archives internationales de pharmacodynamie et de therapie. 1963;143:240-6.

[166] Chung C-y, Bien H, Sobie EA, Dasari V, McKinnon D, Rosati B, et al. Hypertrophic phenotype in cardiac cell assemblies solely by structural cues and ensuing self-organization. The FASEB Journal. 2011;25:851-62.

[167] Schmittgen TD, Livak KJ. Analyzing real-time PCR data by the comparative C(T) method. Nat Protoc. 2008;3:1101-8.

[168] Sato Y, Nakajima S, Shiraga N, Atsumi H, Yoshida S, Koller T, et al. Three-dimensional multi-scale line filter for segmentation and visualization of curvilinear structures in medical images. Medical image analysis. 1998;2:143-68.

[169] Rezakhaniha R, Agianniotis A, Schrauwen JTC, Griffa A, Sage D, Bouten CVC, et al. Experimental investigation of collagen waviness and orientation in the arterial adventitia using confocal laser scanning microscopy. Biomechanics and Modeling in Mechanobiology. 2012;11:461-73.

[170] Grosberg A, Alford PW, McCain ML, Parker KK. Ensembles of engineered cardiac tissues for physiological and pharmacological study: heart on a chip. Lab Chip. 2011;11:4165-73.

[171] Rodriguez EK, Hoger A, McCulloch AD. Stress-Dependent Finite Growth in Soft Elastic Tissues. J Biomech. 1994;27:455-67.

[172] Ramasubramanian A, Taber LA. Computational modeling of morphogenesis regulated by mechanical feedback. Biomechanics and Modeling in Mechanobiology. 2008;7:77-91.

[173] Brower V. Human ES cells: can you build a business around them? Nat Biotechnol. 1999;17:139-42.

[174] FDA. Current Good Tissue Practice (CGTP) and Additional Requirements for Manufacturers of Human Cells, Tissues, and Cellular and Tissue-Based Products (HCT/Ps). Food and Drug Administration Center for Biologics Evaluation and Research. 2011.

[175] Fink DW, Jr. FDA regulation of stem cell-based products. Science. 2009;324:1662-3.

[176] Fox JL. Human iPSC and ESC translation potential debated. Nat Biotechnol. 2011;29:375-6.

[177] Rubin LL. Stem cells and drug discovery: the beginning of a new era? Cell. 2008;132:549-52.

[178] Wobus AM, Loser P. Present state and future perspectives of using pluripotent stem cells in toxicology research. Arch Toxicol. 2011;85:79-117.

[179] Placzek MR, Chung IM, Macedo HM, Ismail S, Mortera Blanco T, Lim M, et al. Stem cell bioprocessing: fundamentals and principles. J R Soc Interface. 2009;6:209-32.

[180] Thomson H. Bioprocessing of embryonic stem cells for drug discovery. Trends Biotechnol. 2007;25:224-30.

[181] Webb S. The gold rush for induced pluripotent stem cells. Nat Biotechnol. 2009;27:977-9.

[182] Mummery CL, Zhang J, Ng ES, Elliott DA, Elefanty AG, Kamp TJ. Differentiation of human embryonic stem cells and induced pluripotent stem cells to cardiomyocytes: a methods overview. Circ Res. 2012;111:344-58.

[183] Ng SY, Wong CK, Tsang SY. Differential gene expressions in atrial and ventricular myocytes: insights into the road of applying embryonic stem cell-derived cardiomyocytes for future therapies. Am J Physiol Cell Physiol. 2010;299:C1234-49.

[184] Bruneau BG. Transcriptional regulation of vertebrate cardiac morphogenesis. Circ Res. 2002;90:509-19.

[185] Kleber AG, Rudy Y. Basic mechanisms of cardiac impulse propagation and associated arrhythmias. Physiol Rev. 2004;84:431-88.

[186] Sartiani L, Bettiol E, Stillitano F, Mugelli A, Cerbai E, Jaconi ME. Developmental changes in cardiomyocytes differentiated from human embryonic stem cells: a molecular and electrophysiological approach. Stem Cells. 2007;25:1136-44.

[187] Maltsev VA, Wobus AM, Rohwedel J, Bader M, Hescheler J. Cardiomyocytes differentiated in vitro from embryonic stem cells developmentally express cardiac-specific genes and ionic currents. Circ Res. 1994;75:233-44.

[188] McCain ML, Sheehy SP, Grosberg A, Goss JA, Parker KK. Recapitulating maladaptive, multiscale remodeling of failing myocardium on a chip. Proc Natl Acad Sci U S A. 2013;110:9770-5.

[189] Kuczynski W, Zywucki B, Malecki J. Determination of orientational order parameter in various liquid-cryst alline phases. Mol Cryst Liq Cryst. 2002;381:1-19.

[190] Dabiri GA, Turnacioglu KK, Sanger JM, Sanger JW. Myofibrillogenesis visualized in living embryonic cardiomyocytes. Proc Natl Acad Sci U S A. 1997;94:9493-8.

[191] LoRusso SM, Rhee D, Sanger JM, Sanger JW. Premyofibrils in spreading adult cardiomyocytes in tissue culture: evidence for reexpression of the embryonic program for myofibrillogenesis in adult cells. Cell Motil Cytoskeleton. 1997;37:183-98.

[192] Weinberg S, Lipke EA, Tung L. In vitro electrophysiological mapping of stem cells. Methods in molecular biology (Clifton, NJ). 2010;660:215-37.

[193] Thomas SP, Bircher-Lehmann L, Thomas SA, Zhuang J, Saffitz JE, Kleber AG. Synthetic Strands of Neonatal Mouse Cardiac Myocytes : Structural and Electrophysiological Properties. Circ Res. 2000;87:467-73.

[194] Bers DM. Cardiac excitation-contraction coupling. Nature. 2002;415:198-205.

[195] Stuyvers BD, McCulloch AD, Guo J, Duff HJ, ter Keurs HEDJ. Effect of stimulation rate, sarcomere length and Ca(2+) on force generation by mouse cardiac muscle. J Physiol. 2002;544:817-30.

[196] Gao WD, Perez NG, Marban E. Calcium cycling and contractile activation in intact mouse cardiac muscle. J Physiol. 1998;507 (Pt 1):175-84.

[197] Birmingham A, Selfors LM, Forster T, Wrobel D, Kennedy CJ, Shanks E, et al. Statistical methods for analysis of high-throughput RNA interference screens. Nat Methods. 2009;6:569-75.

[198] Zhang XD. A pair of new statistical parameters for quality control in RNA interference high-throughput screening assays. Genomics. 2007;89:552-61.

[199] Cassino TR, Drowley L, Okada M, Beckman SA, Keller B, Tobita K, et al. Mechanical loading of stem cells for improvement of transplantation outcome in a model

of acute myocardial infarction: the role of loading history. Tissue engineering Part A. 2012;18:1101-8.

[200] Abramoff MD, Magalhaes, P.J., Ram, S.J. . Image Processing with ImageJ. Biophotonics International. 2004;11:36-42.

[201] Herron TJ, Lee P, Jalife J. Optical imaging of voltage and calcium in cardiac cells & tissues. Circ Res. 2012;110:609-23.

[202] Fedorov VV, Lozinsky IT, Sosunov EA, Anyukhovsky EP, Rosen MR, Balke CW, et al. Application of blebbistatin as an excitation-contraction uncoupler for electrophysiologic study of rat and rabbit hearts. Heart rhythm : the official journal of the Heart Rhythm Society. 2007;4:619-26.

[203] Thomson H. Bioprocessing of embryonic stem cells for drug discovery. Trends in biotechnology. 2007;25:224-30.

[204] Placzek MR, Chung IM, Macedo HM, Ismail S, Mortera Blanco T, Lim M, et al. Stem cell bioprocessing: fundamentals and principles. J R Soc Interface. 2009;6:209-32.

[205] Fink DW, Jr. FDA regulation of stem cell-based products. Science. 2009;324:1662-3.

[206] Lutolf MP, Hubbell JA. Synthetic biomaterials as instructive extracellular microenvironments for morphogenesis in tissue engineering. Nat Biotechnol. 2005;23:47-55.

[207] Chau Y, Luo Y, Cheung ACY, Nagai Y, Zhang SG, Kobler JB, et al. Incorporation of a matrix metalloproteinase-sensitive substrate into self-assembling peptides - A model for biofunctional scaffolds. Biomaterials. 2008;29:1713-9.

[208] Kraehenbuehl TP, Zammaretti P, Van der Vlies AJ, Schoenmakers RG, Lutolf MP, Jaconi ME, et al. Three-dimensional extracellular matrix-directed cardioprogenitor differentiation: systematic modulation of a synthetic cell-responsive PEG-hydrogel. Biomaterials. 2008;29:2757-66.

[209] Huebsch N, Mooney DJ. Inspiration and application in the evolution of biomaterials. Nature. 2009;462:426-32.

[210] Eschenhagen T, Zimmermann WH. Engineering myocardial tissue. Circ Res. 2005;97:1220-31.

[211] Feinberg AW, Parker KK. Surface-initiated assembly of protein nanofabrics. Nano Lett. 2010;10:2184-91.

[212] Badrossamay MR, McIlwee HA, Goss JA, Parker KK. Nanofiber assembly by rotary jet-spinning. Nano Lett. 2010;10:2257-61.

[213] Huh D, Matthews BD, Mammoto A, Montoya-Zavala M, Hsin HY, Ingber DE. Reconstituting organ-level lung functions on a chip. Science. 2010;328:1662-8.

[214] Domian IJ, Chiravuri M, van der Meer P, Feinberg AW, Shi X, Shao Y, et al. Generation of functional ventricular heart muscle from mouse ventricular progenitor cells. Science. 2009;326:426-9.

6 Appendices

6.1 Appendix A: List of Publications

1. **Sheehy SP**, Pasqualini F, Grosberg A, Park SJ, Yvonne Aratyn-Schaus Y, Parker KK. Quality Metrics for Stem Cell-Derived Cardiac Myocytes. *Stem Cell Reports*. 2014 Mar;2(3):282-294.
2. Deravi LF, Magyar AP, **Sheehy SP**, Bell GRR, Mäthger LM, Senfta SL, Wardill TJ, Lane WS, Kuzirian AM, Hanlon RT, Hu EL, and Parker KK. The structure–function relationships of a natural nanoscale photonic device in cuttlefish chromatophores. *J. R. Soc. Interface* 11: 20130942.
3. Feinberg AW, Ripplinger CM, van der Meer P, **Sheehy SP**, Domian I, Chien KR, Parker KK. Functional differences in engineered myocardium from embryonic stem cell-derived versus neonatal cardiomyocytes. *Stem Cell Reports*. 2013;1:387-96.
4. McCain ML, **Sheehy SP**, Grosberg A, Goss JA, and Parker KK. Recapitulating maladaptive, multiscale remodeling of failing myocardium on a chip. *PNAS*. 2013; 110: 9770-9775.
5. Kuo P, Lee H, Bray MA, Geisse NA, Huang YT, Adams WJ, **Sheehy SP**, Parker KK. Myocyte shape regulates lateral registry of sarcomeres and contractility. *Am. J. Pathol*. 2012; 181(6):2030-7.
6. **Sheehy SP**, Grosberg A, Parker KK. The contribution of cellular mechanotransduction to cardiomyocyte form and function. *Biomech Model Mechanobiol*. 2012; 11: 1227-1239.

7. Feinberg AW, Alford PW, Jin H, Ripplinger CM, Werdich AA, **Sheehy SP**, Grosberg A, Parker KK. Controlling the contractile strength of engineered cardiac muscle by hierarchal tissue architecture. *Biomaterials*. 2012;33:5732-5741.
8. **Sheehy SP**, Parker KK. The Role of Mechanical Forces in Guiding Tissue Differentiation. In: Bernstein H, editor. Tissue Engineering in Regenerative Medicine. Springer; 2011:77-97.

6.2 Appendix B: Table of Genes Measured in Custom Rat qPCR Array

Gene Symbol	Refseq #	Gene Description
Hey2	NM_130417	Hairy/enhancer-of-split related with YRPW motif 2
Irx4	NM_001107330	Iroquois homeobox 4
Mef2c	XM_574821	Myocyte enhancer factor 2C
Gata4	NM_144730	GATA binding protein 4
Myocd	NM_182667	Myocardin
Nkx2-5	NM_053651	NK2 transcription factor related, locus 5 (Drosophila)
Tbx5	NM_001009964	T-box 5
Nppa	NM_012612	Natriuretic peptide precursor A
Nppb	NM_031545	Natriuretic peptide precursor B
Acta1	NM_019212	Actin, alpha 1, skeletal muscle
Adra1b	NM_016991	Adrenergic, alpha-1B-, receptor
Adra1d	NM_024483	Adrenergic, alpha-1D-, receptor
Adra2a	NM_012739	Adrenergic, alpha-2A-, receptor
Actc1	NM_019183	Actin, alpha, cardiac muscle 1
Actn1	NM_031005	Actinin, alpha 1
Actn2	NM_001170325	Actinin alpha 2
Pln	NM_022707	Phospholamban
Tnni3	NM_017144	Troponin I type 3 (cardiac)
Tnnt2	NM_012676	Troponin T type 2 (cardiac)
Ttn	XM_001065955	Titin
Myh3	NM_012604	Myosin, heavy chain 3, skeletal muscle, embryonic
Myh6	NM_017239	Myosin, heavy chain 6, cardiac muscle, alpha
Myh7	NM_017240	Myosin, heavy chain 7, cardiac muscle, beta
Myl2	NM_001035252	Myosin, light polypeptide 2, regulatory, cardiac, slow
Myl3	NM_012606	Myosin, light chain 3, alkali; ventricular, skeletal, slow
Myl4	NM_001109495	Myosin, light chain 4
Myl7	NM_001106017	Myosin, light chain 7, regulatory
Cacna1c	NM_012517	Calcium channel, voltage-dependent, L type, alpha 1C subunit
Cacna1d	NM_017298	Calcium channel, voltage-dependent, L type, alpha 1D subunit
Cacna1g	NM_031601	Calcium channel, voltage-dependent, T type, alpha 1G subunit
Cacna1h	NM_153814	Calcium channel, voltage-dependent, T type, alpha 1H subunit
Cacna1s	NM_053873	Calcium channel, voltage-dependent, L type, alpha 1S subunit
Kcna5	NM_012972	Potassium voltage-gated channel, shaker-related subfamily, member 5
Kcne1	NM_012973	Potassium voltage-gated channel, Isk-related family, member 1
Kcne2	NM_133603	Potassium voltage-gated channel, Isk-related family, member 2
Kcnd2	NM_031730	Potassium voltage-gated channel, Shal-related subfamily, member 2
Kcnd3	NM_031739	Potassium voltage-gated channel, Shal-related subfamily, member 3
Kcnh2	NM_053949	Potassium voltage-gated channel, subfamily H (eag-related), member 2
Kcnj2	NM_017296	Potassium inwardly-rectifying channel, subfamily J, member 2
Kcnj3	NM_031610	Potassium inwardly-rectifying channel, subfamily J, member 3
Kcnj11	NM_031358	Potassium inwardly rectifying channel, subfamily J, member 11
Kcnj12	NM_053981	Potassium inwardly-rectifying channel, subfamily J, member 12
Kcnj14	NM_170718	Potassium inwardly-rectifying channel, subfamily J, member 14
Kcnq1	NM_032073	Potassium voltage-gated channel, KQT-like subfamily, member 1
Scn5a	NM_013125	Sodium channel, voltage-gated, type V, alpha subunit
Slc2a1	NM_138827	Solute carrier family 2 (facilitated glucose transporter), member 1
Slc2a2	NM_012879	Solute carrier family 2 (facilitated glucose transporter), member 2

Slc8a1	NM_019268	Solute carrier family 8 (sodium/calcium exchanger), member 1
Hcn1	NM_053375	Hyperpolarization-activated cyclic nucleotide-gated potassium channel 1
Hcn3	NM_053685	Hyperpolarization-activated cyclic nucleotide-gated potassium channel 3
Hcn4	NM_021658	Hyperpolarization activated cyclic nucleotide-gated potassium channel 4
Gja1	NM_012567	Gap junction protein, alpha 1
Gja5	NM_019280	Gap junction protein, alpha 5
Atp1a2	NM_012505	ATPase, Na+/K+ transporting, alpha 2 polypeptide
Atp1a3	NM_012506	ATPase, Na+/K+ transporting, alpha 3 polypeptide
Atp2a1	NM_058213	ATPase, Ca++ transporting, cardiac muscle, fast twitch 1
Atp2a2	NM_001110139	ATPase, Ca++ transporting, cardiac muscle, slow twitch 2
Ryr2	NM_001191043	Ryanodine receptor 2, cardiac
Ckm	NM_012530	Creatine kinase, muscle
Acsl5	NM_053607	Acyl-CoA synthetase long-chain family member 5
Ptk2	NM_013081	PTK2 protein tyrosine kinase 2
Ilk	NM_133409	Integrin-linked kinase
Ctgf	NM_022266	Connective tissue growth factor
Itga1	NM_030994	Integrin, alpha 1
Itga2	XM_345156	Integrin, alpha 2
Itga4	NM_001107737	Integrin, alpha 4
Itga5	NM_001108118	Integrin, alpha 5 (fibronectin receptor, alpha polypeptide)
Itga6	XM_215984	Integrin, alpha 6
Itgav	NM_001106549	Integrin, alpha V
Itgb1	NM_017022	Integrin, beta 1
Itgb3	NM_153720	Integrin, beta 3
Abra	NM_175844	Actin-binding Rho activating protein
Rhoa	NM_057132	Ras homolog gene family, member A
Cdc42	NM_171994	Cell division cycle 42 (GTP binding protein)
Rac1	NM_134366	Ras-related C3 botulinum toxin substrate 1
Rock1	NM_031098	Rho-associated coiled-coil containing protein kinase 1
Rock2	NM_013022	Rho-associated coiled-coil containing protein kinase 2
Rnd1	NM_001013222	Rho family GTPase 1
Vcl	NM_001107248	Vinculin
Ctnnb1	NM_053357	Catenin (cadherin associated protein), beta 1
Vegfa	NM_031836	Vascular endothelial growth factor A
Ctf1	NM_017129	Cardiotrophin 1
Itpr2	NM_031046	Inositol 1,4,5-triphosphate receptor, type 2
Tgfb2	NM_031131	Transforming growth factor, beta 2
Mylk3	NM_001110810	Myosin light chain kinase 3
Camk2d	NM_012519	Calcium/calmodulin-dependent protein kinase II delta
Gapdh	NM_017008	Glyceraldehyde-3-phosphate dehydrogenase
Rplp1	NM_001007604	Ribosomal protein, large, P1
Actb	NM_031144	Actin, beta

6.3 Appendix C: Table of Genes Measured in Custom Mouse qPCR Array

Gene Symbol	Refseq #	Gene Description
Hey2	NM_013904	Hairy/enhancer-of-split related with YRPW motif 2
Irx4	NM_018885	Iroquois related homeobox 4 (Drosophila)
Bmp10	NM_009756	Bone morphogenetic protein 10
Gata4	NM_008092	GATA binding protein 4
Myocd	NM_145136	Myocardin
Nkx2-5	NM_008700	NK2 transcription factor related, locus 5 (Drosophila)
Tbx5	NM_011537	T-box 5
Nppa	NM_008725	Natriuretic peptide type A
Acta1	NM_009606	Actin, alpha 1, skeletal muscle
Adra1b	NM_007416	Adrenergic receptor, alpha 1b
Adra2a	NM_007417	Adrenergic receptor, alpha 2a
Actc1	NM_009608	Actin, alpha, cardiac muscle 1
Actn1	NM_134156	Actinin, alpha 1
Actn2	NM_033268	Actinin alpha 2
Pln	NM_023129	Phospholamban
Tnnt2	NM_011619	Troponin T2, cardiac
Ttn	NM_011652	Titin
Myh6	NM_010856	Myosin, heavy polypeptide 6, cardiac muscle, alpha
Myh7	NM_080728	Myosin, heavy polypeptide 7, cardiac muscle, beta
Myl2	NM_010861	Myosin, light polypeptide 2, regulatory, cardiac, slow
Myl3	NM_010859	Myosin, light polypeptide 3
Myl4	NM_010858	Myosin, light polypeptide 4
Myl7	NM_022879	Myosin, light polypeptide 7, regulatory
Cacna1c	NM_009781	Calcium channel, voltage-dependent, L type, alpha 1C subunit
Cacna1d	NM_028981	Calcium channel, voltage-dependent, L type, alpha 1D subunit
Cacna1g	NM_009783	Calcium channel, voltage-dependent, T type, alpha 1G subunit
Cacna1h	NM_021415	Calcium channel, voltage-dependent, T type, alpha 1H subunit
Kcna5	NM_145983	Potassium voltage-gated channel, shaker-related subfamily, member 5
Kcne1	NM_008424	Potassium voltage-gated channel, Isk-related subfamily, member 1
Kcne2	NM_134110	Potassium voltage-gated channel, Isk-related subfamily, gene 2
Kcnd2	NM_019697	Potassium voltage-gated channel, Shal-related family, member 2
Kcnd3	NM_019931	Potassium voltage-gated channel, Shal-related family, member 3
Kcnh2	NM_013569	Potassium voltage-gated channel, subfamily H (eag-related), member 2
Kcnj2	NM_008425	Potassium inwardly-rectifying channel, subfamily J, member 2
Kcnj3	NM_008426	Potassium inwardly-rectifying channel, subfamily J, member 3
Kcnj11	NM_010602	Potassium inwardly rectifying channel, subfamily J, member 11
Kcnj12	NM_010603	Potassium inwardly-rectifying channel, subfamily J, member 12
Kcnj14	NM_145963	Potassium inwardly-rectifying channel, subfamily J, member 14
Kcnq1	NM_008434	Potassium voltage-gated channel, subfamily Q, member 1
Scn5a	NM_021544	Sodium channel, voltage-gated, type V, alpha
Slc2a1	NM_011400	Solute carrier family 2 (facilitated glucose transporter), member 1
Slc2a2	NM_031197	Solute carrier family 2 (facilitated glucose transporter), member 2
Slc8a1	NM_011406	Solute carrier family 8 (sodium/calcium exchanger), member 1
Hcn1	NM_010408	Hyperpolarization-activated, cyclic nucleotide-gated K+ 1
Hcn3	NM_008227	Hyperpolarization-activated, cyclic nucleotide-gated K+ 3
Hcn4	NM_001081192	Hyperpolarization-activated, cyclic nucleotide-gated K+ 4
Gja1	NM_010288	Gap junction protein, alpha 1

Gja5	NM_008121	Gap junction protein, alpha 5
Atp1a2	NM_178405	ATPase, Na+/K+ transporting, alpha 2 polypeptide
Atp1a3	NM_144921	ATPase, Na+/K+ transporting, alpha 3 polypeptide
Atp2a1	NM_007504	ATPase, Ca++ transporting, cardiac muscle, fast twitch 1
Atp2a2	NM_009722	ATPase, Ca++ transporting, cardiac muscle, slow twitch 2
Ryr2	NM_023868	Ryanodine receptor 2, cardiac
Ckm	NM_007710	Creatine kinase, muscle
Acsl5	NM_027976	Acyl-CoA synthetase long-chain family member 5
Ptk2	NM_007982	PTK2 protein tyrosine kinase 2
Ilk	NM_010562	Integrin linked kinase
Ctgf	NM_010217	Connective tissue growth factor
Itga1	NM_001033228	Integrin alpha 1
Itga2	NM_008396	Integrin alpha 2
Itga4	NM_010576	Integrin alpha 4
Itga5	NM_010577	Integrin alpha 5 (fibronectin receptor alpha)
Itgav	NM_008402	Integrin alpha V
Itgb1	NM_010578	Integrin beta 1 (fibronectin receptor beta)
Itgb3	NM_016780	Integrin beta 3
Abra	NM_175456	Actin-binding Rho activating protein
Rhoa	NM_016802	Ras homolog gene family, member A
Cdc42	NM_009861	Cell division cycle 42 homolog (S. cerevisiae)
Rac1	NM_009007	RAS-related C3 botulinum substrate 1
Rock1	NM_009071	Rho-associated coiled-coil containing protein kinase 1
Rock2	NM_009072	Rho-associated coiled-coil containing protein kinase 2
Rnd1	NM_172612	Rho family GTPase 1
Vcl	NM_009502	Vinculin
Ctnnb1	NM_007614	Catenin (cadherin associated protein), beta 1
Aifm1	NM_012019	Apoptosis-inducing factor, mitochondrion-associated 1
Atp5j	NM_016755	ATP synthase, H+ transporting, mitochondrial F0 complex, subunit F
Hsp90ab1	NM_008302	Heat shock protein 90 alpha (cytosolic), class B member 1
Hspa2	NM_008301	Heat shock protein 2
Hsph1	NM_013559	Heat shock 105kDa/110kDa protein 1
Bcat1	NM_007532	Branched chain aminotransferase 1, cytosolic
Ch25h	NM_009890	Cholesterol 25-hydroxylase
Itpr2	NM_019923	Inositol 1,4,5-triphosphate receptor 2
Tgfb2	NM_009367	Transforming growth factor, beta 2
Notch1	NM_008714	Notch gene homolog 1 (Drosophila)
Pou5f1	NM_013633	POU domain, class 5, transcription factor 1
Nanog	NM_028016	Nanog homeobox
Sox2	NM_011443	SRY-box containing gene 2
Gapdh	NM_008084	Glyceraldehyde-3-phosphate dehydrogenase
Actb	NM_007393	Actin, beta

6.4 Appendix D: Table of Experimental Parameters Used for Quality Index

Measurement Class	Measurement	Measurement Description
Contractility	Diastolic	Diastolic stress
Contractility	Systolic	Systolic stress
Contractility	Twitch	Twitch Stress (Systolic - Diastolic)
Electrophysiology	LCV	Longitudinal conduction velocity
Electrophysiology	TCV	Transverse conduction velocity
Electrophysiology	AR	Anisotropy ratio
Electrophysiology	APD50	Action potential duration at 50% repolarization
Electrophysiology	APD90	Action potential duration at 90% repolarization
Electrophysiology	TOT	Total calcium current density
Electrophysiology	LCC	L-type calcium current density
Electrophysiology	TCC	T-type calcium current density
Morphology	SPD	Sarcomere packing density
Morphology	SL	Sarcomere length
Morphology	OOP	Orientational order parameter
Gene expression	*Hey2*	Hairy/enhancer-of-split related with YRPW motif 2
Gene expression	*Irx4*	Iroquois related homeobox 4 (Drosophila)
Gene expression	*Gata4*	GATA binding protein 4
Gene expression	*Myocd*	Myocardin
Gene expression	*Nkx2-5*	NK2 transcription factor related, locus 5 (Drosophila)
Gene expression	*Tbx5*	T-box 5
Gene expression	*Nppa*	Natriuretic peptide type A
Gene expression	*Acta1*	Actin, alpha 1, skeletal muscle
Gene expression	*Adra1b*	Adrenergic receptor, alpha 1b
Gene expression	*Adra2a*	Adrenergic receptor, alpha 2a
Gene expression	*Actc1*	Actin, alpha, cardiac muscle 1
Gene expression	*Actn1*	Actinin, alpha 1
Gene expression	*Actn2*	Actinin alpha 2
Gene expression	*Pln*	Phospholamban
Gene expression	*Tnnt2*	Troponin T2, cardiac
Gene expression	*Ttn*	Titin
Gene expression	*Myh6*	Myosin, heavy polypeptide 6, cardiac muscle, alpha
Gene expression	*Myh7*	Myosin, heavy polypeptide 7, cardiac muscle, beta
Gene expression	*Myl2*	Myosin, light polypeptide 2, regulatory, cardiac, slow
Gene expression	*Myl3*	Myosin, light polypeptide 3
Gene expression	*Myl4*	Myosin, light polypeptide 4
Gene expression	*Myl7*	Myosin, light polypeptide 7, regulatory
Gene expression	*Cacna1c*	Calcium channel, voltage-dependent, L type, alpha 1C subunit
Gene expression	*Cacna1d*	Calcium channel, voltage-dependent, L type, alpha 1D subunit
Gene expression	*Cacna1g*	Calcium channel, voltage-dependent, T type, alpha 1G subunit
Gene expression	*Cacna1h*	Calcium channel, voltage-dependent, T type, alpha 1H subunit

Gene expression	*Kcne1*	Potassium voltage-gated channel, Isk-related subfamily, member 1
Gene expression	*Kcne2*	Potassium voltage-gated channel, Isk-related subfamily, gene 2
Gene expression	*Kcnd2*	Potassium voltage-gated channel, Shal-related family, member 2
Gene expression	*Kcnd3*	Potassium voltage-gated channel, Shal-related family, member 3
Gene expression	*Kcnh2*	Potassium voltage-gated channel, subfamily H (eag-related), member 2
Gene expression	*Kcnj2*	Potassium inwardly-rectifying channel, subfamily J, member 2
Gene expression	*Kcnj3*	Potassium inwardly-rectifying channel, subfamily J, member 3
Gene expression	*Kcnj11*	Potassium inwardly rectifying channel, subfamily J, member 11
Gene expression	*Kcnj12*	Potassium inwardly-rectifying channel, subfamily J, member 12
Gene expression	*Kcnj14*	Potassium inwardly-rectifying channel, subfamily J, member 14
Gene expression	*Kcnq1*	Potassium voltage-gated channel, subfamily Q, member 1
Gene expression	*Scn5a*	Sodium channel, voltage-gated, type V, alpha
Gene expression	*Slc2a1*	Solute carrier family 2 (facilitated glucose transporter), member 1
Gene expression	*Slc2a2*	Solute carrier family 2 (facilitated glucose transporter), member 2
Gene expression	*Slc8a1*	Solute carrier family 8 (sodium/calcium exchanger), member 1
Gene expression	*Hcn1*	Hyperpolarization-activated, cyclic nucleotide-gated K+ 1
Gene expression	*Hcn3*	Hyperpolarization-activated, cyclic nucleotide-gated K+ 3
Gene expression	*Hcn4*	Hyperpolarization-activated, cyclic nucleotide-gated K+ 4
Gene expression	*Gja1*	Gap junction protein, alpha 1
Gene expression	*Gja5*	Gap junction protein, alpha 5
Gene expression	*Atp1a2*	ATPase, Ca++ transporting, cardiac muscle, fast twitch 1
Gene expression	*Atp2a2*	ATPase, Ca++ transporting, cardiac muscle, slow twitch 2
Gene expression	*Ryr2*	Ryanodine receptor 2, cardiac
Gene expression	*Ckm*	Creatine kinase, muscle